Algorithms for Indoor Localization Based on IEEE 802.15.4-2011 UWB and Inertial Sensors

Tingcong Ye
108115427

NATIONAL UNIVERSITY OF IRELAND, CORK

SCHOOL OF ENGINEERING

DEPARTMENT OF ELECTRICAL AND ELECTRONIC ENGINEERING

Thesis submitted for the degree of Doctor of Philosophy

January 2015

Head of Department: Prof Nabeel A. Riza

Supervisors: Dr Michael Walsh
Mr Brendan O'Flynn

Research supported by NEMBES, eGo, WSN Group, Tyndall National Institute

Contents

List of Figures

List of Tables

Glossary of Acronyms

Acronym	Meaning
UWB	Ultra Wideband
TOA	Time of Arrival
MEMS	Micro Electro Mechanical Sensors
IMU	Inertial Measurement Unit
SNR	Signal to Noise Ratio
SDS-TW-TOA	Symmetric Double Sided Two Way Time of Arrival
INS	Internal Navigation System
IPS	Indoor Positioning System
GPS	Global Positioning System
TOF	Time of Flight
LOS	Line of Sight
NLOS	Non Line of Sight
AWGN	Additive White Gaussian Noise
ADC	Analog to Digital Converter
AGC	Automatic Gain Control
AOA	Angle of Arrival
RSS	Received Signal Strength
CRLB	Cramer-Rao Lower Bound
SFD	Start of Frame Delimiter
PHR	Physical Header
CIR	Channel Impulse Response
SB	Search Back
EKF	Extended Kalman Filter
PRF	Pulse Repetition Frequency
SPI	Serial Peripheral Interface
MAE	Mean Absolute Error
CDF	Cumulative Probability Functions
MMF	Maximum and Minimum Filter
DAC	Digital Analogue Converter
VGA	Variable Gain Amplifier
LNA	Low Noise Amplifier
BER	Bit Error Rate
QPC	Quick Power Control
SPC	Slow Power Control
FPC	Fixed Step Size Power Control
NPC	Non Power Control

I, Tingcong Ye, certify that this thesis is my own work and I have not obtained a degree in this university or elsewhere on the basis of the work submitted in this thesis.

Tingcong Ye

To my family.

Acknowledgements

This dissertation would not have been possible without the help and contributions of many individuals, to whom I am greatly in debt.

First and foremost, I must thank my supervisors, Dr. Michael Walsh, and Mr. Brendan O'Flynn, for giving me an opportunity to work in this fascinating field of indoor positioning. I have greatly benefited from their rigorous approach to applied research. Besides engineering, they always encourage me to broaden my knowledge and improve my presentation and language skills. I sincerely appreciate the patience they had in me over the past four years. I am grateful to them for funding my stay at the wonderful Tyndall National Institute and beautiful Cork city. Michael, Brendan, without your support, my thesis would not have reached this stage.

I thank my advisors, Dr. Alan Mathewson and Dr. Bob Manning, who always give precious advice and suggestion about my project, and warm encouragement and support. I thank Networked Embedded Systems (NEMBES) and eGo for the financial support.

I enjoyed my time as a PhD student in Tyndall National Institute and would like to thank the head of Microsystems Center, Prof. Cian O'Mathuna, former CEO, Prof. Roger Whatmore, CEO, Dr. Kieran Drain, as well as all the staff and students in Tyndall.

I would like to thank all of the members of the Room 3.1.51, Block A, Dr. Sean Harte, Padraig Curran, Brian McCarthy, Liqiang Zheng, Mark Gaffney, Wassim Magnin, Donal Kennedy, for your brotherly affection, support and selfless help. I enjoyed your skinny jokes about me. I would like to thank all of the members of the Wireless Sensor Network Group. I thank Salvatore Tedesco, who has been really helpful for setting up and implementing our experiments. John Buckley and Peter Haigh taught me how to use the Vector Networked Analyzer and Frequency Analyzer, and have been very

helpful for my experiments. Philip Angove and Steven Aherne supplied me electronic components. And thanks for other guys in WSN group for your help during the past four years.

I thank Mr. Pet Mehigan and Mr. Bill Cashman, for helping to move the partitions for our experiments.

Special thanks to my parents and brother, I owe you so much gratitude. I would also like to thank my wife, Xiaofang, for her unconditional support and love.

Abstract

In this thesis, extensive experiments are firstly conducted to characterise the performance of using the emerging IEEE 802.15.4-2011 ultra wideband (UWB) for indoor localization, and the results demonstrate the accuracy and precision of using time of arrival measurements for ranging applications.

A multipath propagation controlling technique is synthesized which considers the relationship between transmit power, transmission range and signal-to-noise ratio. The methodology includes a novel bilateral transmitter output power control algorithm which is demonstrated to be able to stabilize the multipath channel, and enable sub 5cm instant ranging accuracy in line of sight conditions.

A fully-coupled architecture is proposed for the localization system using a combination of IEEE 802.15.4-2011 UWB and inertial sensors. This architecture not only implements the position estimation of the object by fusing the UWB and inertial measurements, but enables the nodes in the localization network to mutually share positional and other useful information via the UWB channel. The hybrid system has been demonstrated to be capable of simultaneous local-positioning and remote-tracking of the mobile object.

Three fusion algorithms for relative position estimation are proposed, including internal navigation system (INS), INS with UWB ranging correction, and orientation plus ranging. Experimental results show that the INS with UWB correction algorithm achieves an average position accuracy of 0.1883m, and gets 83% and 62% improvements on the accuracy of the INS (1.0994m) and the existing extended Kalman filter tracking algorithm (0.5m), respectively.

Chapter 1

Introduction

High precision location information is of great importance in many commercial, public safety, and military applications. Global positioning system (GPS) is an excellent technology for many localization scenarios and typically has fine precision outdoors [35]. However, GPS can not be deployed for indoor use, because line of sight (LOS) transmission between receivers and satellites is not possible in an indoor environment [33]. Reliable indoor localization technology is a key enabler for a diverse set of applications including robotics, logistics, security tracking (the localization of authorized persons in high security areas), medical services (the monitoring of patients), search and rescue operations (communications with fire fighters or natural disaster victims), control of home appliances, automotive safety and a large set of wireless sensor network (WSN) applications [62]. Such applications require localization systems with submeter, and even centimeter level accuracy [63].

The purpose of localization algorithms is to accurately determine the location of an object given a set of measurements. Wireless localization techniques can be classified based on measurements between an object and each reference point (or anchor), such as range-based, angle-based, and proximity-based localization [34]. Among them, the range-based systems are more suitable for high precision localization. Employing ranging measurements between the object and anchors, a trilateration algorithm can

compute the object's location in a 2D plane.

The precision of the location information depends on whether the ranging measurements contain errors or not. Alternative wireless technologies have been used for the design of an indoor localization system, such as infrared, ultrasound, optical signal, RFID, WIFI, Bluetooth, Zigbee and ultra wideband (UWB). Among them, UWB system offers the potential of achieving high precision localization through time of arrival (TOA) ranging techniques, even in harsh environments, due to its ability to resolve multipath and penetrate obstacles [22]. The potential of UWB technology for future wireless communication networks was recognized by the IEEE, which adopted UWB in the IEEE 802.15.4-2011 wireless personal area network (WPAN) standard for the creation of a physical layer for short-range and low data rate communications and for precise localization [3]. The IEEE 802.15.4-2011 was previously called IEEE 802.15.4a WPAN standard [2].

In TOA ranging, the distance between wireless devices can be calculated using measurements of the signal propagation delay, or time of flight (TOF), $TOF = d/c$, where d is the actual distance and c is the speed of electromagnetic waves. The signal propagation delay equals the receive timestamp minus the transmit timestamp. The transmit timestamp can be accurately measured by the timer circuitry when the signal is sent. The receive timestamp equals the arrival time of the first signal path with the largest power.

An inertial system based on micro electro mechanical sensors (MEMS) is another promising technology for indoor localization. An inertial measurement unit (IMU) consisting of a gyroscope, an accelerometer and a magnetometer, is inexpensive, small and highly portable [32]. When the IMU is attached to an object, its measurements can be used to compute the location of the object relative to a known starting point [68]. Orientation of the IMU is calculated by integrating the angular velocity, which is measured by the gyroscope. The location of the IMU is computed by double integra-

tion of the acceleration, which in turn is found by rotating external specific force using the known orientation and subtracting the acceleration due to gravity. The advantage of inertial system for indoor localization is that the system determines the location of an object using onboard measurements, capable of rejecting multipath effects and non line of sight (NLOS) conditions.

Currently, a combination of UWB and inertial sensors is an attractive solution for indoor localization [74]. This is because such a hybrid system can improve the performance of UWB-only or IMU-only localization. The IMU can provide location information of an object when UWB measurements are absent due to range limitations or adverse NLOS conditions. In addition, a stable UWB ranging can help to eliminate the inherent integration drift of inertial navigation.

1.1 Contributions

This work focuses on the development of algorithms to improve the performance of indoor localization system using the emerging IEEE 802.15.4-2011 UWB technology and inertial sensors. The main contributions to the state of the art are summarized as follows.

• The first reported performance characterization of the IEEE 802.15.4-2011 UWB for indoor localization, and the results demonstrate the accuracy and precision of using TOA measurements for ranging applications.

• The first reported observation of the features of IEEE 802.15.4-2011 UWB propagation in indoor environments, and relationship between transmit power, transmission range and signal to noise ratio (SNR).

• A bilateral transmitter output power control algorithm is developed, which can:

(1) stabilize the IEEE 802.15.4-2011 UWB multipath channels;

(2) cooperate seamlessly with a symmetric double sided two way ranging protocol;

(3) achieve 80% within 5cm instant ranging precision, and get 68% improvement on the precision of the existing non-power control methodology in LOS conditions.

• A fully-coupled architecture is developed for hybrid IEEE 802.15.4-2011 UWB and IMU localization system , which can:

(1) perform data exchange with other network nodes using the UWB channel;

(2) realize simultaneous local-positioning and remote-tracking of an object.

• A fusion algorithm, called internal navigation system (INS) with UWB ranging correction, is developed, which obtains a total average position error of 0.1883m of three practical cases, and gets 83% and 62% improvements on the accuracy of the pure INS (1.0994m) and the existing extended Kalman filter tracking algorithm fusing UWB and IMU data (0.5m), respectively.

• The results of this work were published and the peer reviewed. Papers are listed as follows.

(1) Ye T., Walsh M., Haigh P., Barton J., Mathewson A., O'Flynn B., "Experimental Impulse Radio IEEE 802.15.4a UWB Based Wireless Sensor Localization Technology: Characterization, Reliability and Ranging," 22nd IET Irish Signals and Systems Conference (ISSC), June, 2011.

(2) Ye T., Walsh M., O'Flynn B., "Experimental Analysis of Transmit-power for IEEE 802.15.4a UWB Ranging under Multipath Environment," 23th IET Irish Signals and Systems Conference (ISSC), June, 2012.

(3) Ye T., Walsh M., Haigh P., Barton J., Mathewson A., O'Flynn B., "An experimental evaluation of IEEE 802.15.4a ultra wideband technology for precision indoor ranging," International Journal of Ambient Computing and Intelligence (IJACI) 4(2), p.48-63, April-June 2012.

(4) Ye T., Walsh M., O'Flynn B., O'Mathuna, C., "Adaptive Up/Down Transmit-power Control in IEEE 802.15.4a UWB Ranging under Multi-path Environment," IEEE 27th Convention of Electrical and Electronics Engineers in Israel, p.1-5, Nov. 2012.

(5) Ye T., Walsh M., O'Flynn B., "Multipath Effects Mitigation for UWB-IR Ranging Using Bilateral Power Control Methodology," 24th IET Irish Signals and Systems Conference (ISSC), June, 2013.

(6) Ye T., Walsh M., O'Flynn B., O'Mathuna, C., "Transceiver-power Control for 802.15.4a UWB-IR Ranging in the Presence of Multipath Propagation," The Seventh International Conference on Sensor Technologies and Applications, August, 2013.

(7) Ye T., Tedesco S., Walsh M., O'Flynn B., "Fully-Coupled Hybrid IEEE 802.15.4a UWB/IMU Position Estimation in Indoor Environments," 25th IET Irish Signals and Systems Conference (ISSC) and China-Ireland International Conference on Information and Communications Technologies, June, 2014.

1.2 Problem Statement

The accuracy and precision are two main performance parameters of the indoor localization system. Extensive experiments are firstly conducted in this work to characterise the performance of using the emerging IEEE 802.15.4-2011 UWB for indoor localization, and the results demonstrate the accuracy and precision of TOA ranging. The ranging accuracies in different propagation conditions lie in the order of decimeters. Although the obtained performance is sufficient for some aforementioned applications, many potential application areas have higher performance requirements. For example, in-building robot navigation requires eight-centimeter accuracy [37].

An important problem of IEEE 802.15.4-2011 UWB TOA ranging in indoor environments is that, if the multipath channel is not stable, the signal communication quality may decrease, resulting in the degradation of instant ranging accuracy and stability.

In multipath channel, each received UWB pulse may have a different shape than the transmitted pulse due to varying antenna characteristics and materials for different propagation paths [17]. Reflections from scatterers in an indoor environment arrive at a receiver as replicas of the transmitted signal with various attenuation levels and delays [52]. A large number of multipath components are uniformly spread over the input range of the analog to digital converter (ADC) [26]. Since the uncertain multipath components do not overlap in time and therefore do not cancel out, the crest factor (crest factor is a measure of a waveform, showing the ratio of peak values to the average value), decreases, resulting in the saturation noise increasing [61]. As a result, the SNR decreases, and adjacent peaks with comparable amplitudes to the correct peak in the channel impulse response may exist, making the TOA detection nontrivial. Moreover, the received signal strength at the antenna is usually not regular in multipath propagation, especially in mobile cases. If the received signal is strong, the ADC goes into saturation and noise increases quickly; on the other hand, if the received signal is too weak, the SNR decreases due to the thermal and quantisation noise [61]. These noise sources affect the received signal quality and hence the performance of IEEE 802.15.4-2011 UWB ranging. In addition, there is no exact model on the signal communication quality of IEEE 802.15.4-2011 UWB signal propagation in multipath environments.

The problem of inertial navigation is that the inertial measurements, such as the angular velocity and the external specific force, include bias and noise terms which cause errors in the calculated location [59]. This integration drift is inherent to all inertial navigation. Using MEMS inertial sensors, the integration drift is relatively large. The error of each calculated location will be accumulated for a new position estimation. As a result, the orientation and the location are only accurate and reliable for a short period of time. This is the reason why some MEMS IMU based systems are typically used in combination with a stabilizing sensor such as UWB for localization purposes [49].

A limitation of existing hybrid UWB and IMU systems is that their data fusion architectures consider inertial sensors and UWB as ad-hoc components working in isolation, incapable of exchanging inertial or positional data with other network nodes given that the UWB channel is dedicated to ranging alone. As a result issues surrounding extensive infrastructure requirements, synchronization, and limitations associated with the mutual sharing of inertial data have arisen.

The architectures of the proposed hybrid UWB and IMU systems can be classified as loosely coupled data fusion and tightly coupled data fusion [74]. In the former case, two different location estimations are performed simultaneously and independently by UWB and IMU, and the final position of an object is obtained by fusing both outputs with a simple integration method [69]. This approach limits the achievable synchronization between the inertial sensor data and UWB ranging measurements, reducing the achievable accuracy of the system. In the latter case, instead, inertial and UWB measurements are considered as inputs of a particle or Kalman filter, which directly provide the requested position of an object [36].

However, these architectures do not share data with other network nodes. As a consequence, they are limited in simultaneous local-positioning and remote-tracking of the object. In several scenarios, simultaneous local-positioning and remote-tracking of the object might be required. 'Local-positioning' implies that the object is able to self-locate, while 'remote-tracking' indicates that the object is tracked by another node, such as an anchor, to which the object is transmitting the positional data. The importance of simultaneous local-positioning and remote-tracking can be further illustrated by a typical scenario called mobile robot localization [64]. Robots, equipped with sensors for data collection, require their accurate location information to establish a feedback loop for motion control. On the other hand, robots are required to be synchronously and remotely tracked by the user for safety management.

1.3 Hypothesis

The problems mentioned in this work include: 1) the uncertain multipath components from IEEE 802.15.4-2011 UWB multipath channels affect the instant TOA ranging performance; 2) the accuracy of inertial navigation are affected by the bias and noise terms of inertial measurements; and 3) the existing architectures of hybrid UWB and IMU systems are limited in mutual sharing data.

Precise ranging means accurate localization. In order to obtain better precision for applications such as in-building robot navigation which requires eight-centimeter accuracy, the IEEE 802.15.4-2011 UWB based TOA ranging system should be able to address the problem of the uncertain multipath components. Due to the unstable multipath channel, the irregular magnitude of multipath components may generate noise and hence decrease the SNR. According to the path loss model, the channel parameters are varying in different propagation environments [46]. Dynamically controlling the transmitter output power might stabilize the IEEE 802.15.4-2011 multipath channel and hence improve the instant ranging accuracy.

The pure inertial navigation system suffers from the error sources from the MEMS sensors. Due to physical limitations inherent in MEMS inertial sensors, the raw inertial measurements contain more or less bias and noise. In the hybrid UWB and IMU system, fusing the accurate UWB ranging and the erroneous inertial measurements might improve the accuracy of the pure inertial navigation system.

For mutual sharing data between network nodes, a wireless technology is required for the hybrid UWB and IMU systems. Based on the existing architectures, directly using the UWB communication channel for both ranging and transmitting required data such as inertial and UWB measurements, might realize simultaneous local-positioning and remote-tracking of the object.

1.4 Outline

The remainder of this thesis is organized as follows.

Chapter 2 reviews the state of the art wireless positioning technologies for indoor use, approaches for improving UWB TOA ranging performance in multipath environments, the pure inertial navigation system, and the architectures of proposed hybrid UWB and IMU systems.

Chapter 3 provides an examination of the ranging capabilities of the world's first IEEE 802.15.4-2011 UWB transceiver prototype in multipath environments. It analyzes the effects of different propagation conditions on the accuracy and precision of range estimates.

In chapter 4, the features of IEEE 802.15.4-2011 UWB multipath propagation in indoor environments are reported. The bilateral transmitter output power control algorithm is then presented, based on the relationship between transmit power, transmission range and SNR. Experimental results to evaluate this new approach are given in final.

In chapter 5, a novel hybrid fully-coupled hybrid IEEE 802.15.4-2011 UWB and IMU system is described. Three fusion algorithms for position estimation of an object are introduced. Experimental results to show the benefits of such a fully-coupled hybrid positioning system are finally reported.

Chapter 6 provides conclusions and recommendations for future work.

Chapter 2

State of the Art

2.1 Wireless Indoor Localization Technologies

According to recent statistics, most people spend about 80%∼90% of their time in indoor environments, such as office blocks, shopping malls, hospitals, factories and private houses, while 70% of calls and 80% of data connections originate from indoors [5]. Reliable indoor localization can enable a lot of location-based services and location-awareness applications. Opus Research[1] predicts the market for indoor location and place-based marketing and advertising to surpass $10 billion by 2018.

Based on the geometric properties of triangles, triangulation is the conventional localization algorithm to determine the unknown location of an object [34]. Triangulation can be divided into trilateration and angulation. The trilateration is the range based localization. The angulation is the angle based localization. In [63], Vossiek et al introduced that the received signal parameters can be used to measure the distance and angle. The angle can be measured through an angle of arrival (AOA) technique; and the distance can be estimated using two ranging techniques, namely received signal

[1] Source: http://opusresearch.net/wordpress/2014/02/01/opus-research-report-mapping-the-indoor-marketing-opportunity/.

strength (RSS) and time of arrival (TOA).

To date, a number of wireless technologies have been employed for indoor localization, including infrared, ultrasound, optical signal and radio frequency (RF) technology [43]. However, the indoor environment is usually cluttered, rather than resembling the ideal of "free space". This clutter generally comprises not only of the walls, but the furniture, doors, equipment and of course people. These stationary and mobile obstacles have impact on the received signals, such as reflection interference and occlusion.

Infrared systems use incident angles of the light diffused by each infrared transmitter to measure the position of the receiver in a very accurate way (several millimeters resolution) and they are low power and inexpensive [42]. However, infrared signals can not penetrate through obstructions, and therefore require line of sight (LOS) communication between transmitters and receivers. Localization based on infrared technology usually has to install infrared sensors all over the indoor environment to pick up the signals from a transmitter. Moreover, infrared signals are susceptible to sunlight [20].

Ultrasonic localization system using TOA ranging techniques can obtain several centimeters accuracy of the tag's position using hundreds of receivers which were placed on the ceiling [65]. The ultrasonic tag is usually small and inexpensive. However, systems based on ultrasound signals only give a workable and cost effective solution for small volumes due to their limited range. Moreover, ultrasound signals suffer from reflected signals [23].

Optical signal based localization system can provide millimeter level accuracy and are typically more appropriate for short ranges of few meters [45]. However, like infrared, optical signals for localization require LOS conditions, and are affected by sunlight.

The RF technologies are able to penetrate obstacles. Hence, RF radios have a larger coverage area and need less infrastructure compared to infrared, ultrasonic and optical signals. The RF technologies can be divided into narrow bandwidth signal, such as RFID, WIFI, Bluetooth, Zigbee, and large bandwidth signal such as ultra wideband

(UWB). Compared to other RF technologies, the UWB signal has the unique characteristic of large bandwidth.

The Federal Communication Commission (FCC) has defined UWB systems as those which have an absolute bandwidth larger than 500MHz and central frequency larger than 2.5 GHz, or have a fractional bandwidth larger than 0.2 for systems with central frequency lower than 2.5GHz [1]. In order to make UWB coexist with other wireless technologies, the power spectral density of UWB signal is limited and must not exceed -41.3 dBm/MHz for frequency ranges from 3.1 GHz to 10.6 GHz. Due to its large bandwidth property, UWB radio offers various advantages for the design of indoor localization system.

• Multipath immunity. UWB signals use short pulses. As a result, pulses belonging to different multipath reflections tend not to overlap in time. Therefore, the pulses do not interfere with each other and individual paths tend not to fade, unlike narrow bandwidth signals whose multipath components always overlap and incur fading, e.g., WIFi, Bluetooth and Zigbee.

• High ranging, and hence localization accuracy. Large signal bandwidth, and consequently, the fine time resolution of UWB signals has the potential of achieving centimeter level ranging accuracy through signal TOA measurements [52].

• Low cost and low power transceiver circuitry. UWB operates in baseband modulation [41]. A baseband signal can be transmitted without a sine wave carrier (almost "carrier-free"), which facilitates low cost and low power implementation.

• No LOS requirement, less interference, higher penetration ability compared to infrared, ultrasound and optical signals.

The RF technologies have been used for indoor localization [25]. The accuracies of the RFID, WIFI, Bluetooth, Zigbee based localization systems are several meters, which are poor for indoor use. UWB localization system can provide higher accuracy then

other RF technologies.

2.2 UWB Ranging and Localization

To date, many used UWB technology for localization through TOA ranging techniques. In [55], Sharma et al used UWB signals for range estimation through the TOA technique. The TOA measurements provided very accurate range estimates in LOS conditions. In free-space, the average error in estimating the range values was 0.39cm over a range of 40cm. Even though with both the antennas on-body, the average error was 0.89cm over a range of 40cm.

In [56], Silva et al employed the IEEE 802.15.4a compliant UWB signals for industrial localization applications. Experimental results show that the TOA ranging based localization system can obtain 11cm accuracy in LOS conditions over a range of 9m.

In [13], Dalce et al used the IEEE 802.15.4a UWB transceivers and a parallel symmetric double sided two way ranging protocol to measure the distance between the mobile object and anchors. The experimental results show that ranging error is about 1m. A calibration-based correction method was used to improve the distance estimates, and finally obtained approximate 70cm position error over a range of 1.4m.

In [7], Bharadwaj et al from the research group *Queen Mary* in the University of London, used UWB signal for indoor positioning via TOA ranging techniques in the presence of different objects. Maximum error of 5 to 6cm in localisation is achieved in the presence of a wooden block which is due to the fact that it has a height more than the base stations and mobile station making it into a non line of sight situation. Minimum error obtained is 1 to 3cm when no object is present in the area where localisation is taking place.

Some companies also consider UWB radios for indoor localization, such as *Ubisense*[2],

[2]http://www.ubisense.net.

Zebra[3], *Time Domain*[4] and *Decawave*[5]. The available capabilities of these commercial localization systems are summarized in Table 2.1.

The maximum transmission ranges of *Ubisense*, *Zebra*, *Time Domain* and *Decawave* UWB systems are 160m, 200m, 354m and 290m in LOS condition, respectively. The *Time Domain* uses a UWB signal with larger bandwidth of 2GHz than others, and obtains an accuracy of 2cm in LOS conditions using TOA ranging technique. The use of larger signal bandwidth can more easily (at least theoretically) obtain more accurate ranging measurements [16]. However, as described in [58], to exploit the accuracy of large signal bandwidth of 2GHz, a very high frequency clock able to sample inside a sub-nanosecond time window is needed. Using such a high frequency clock, in the order of gigahertz, is not appropriate for implementing a low power UWB transceiver. Compared to the *Time Domain*, other companies use UWB signals with a smaller bandwidth of 0.5GHz. The *Ubisense*, *Zebra* and *Decawave* localization systems can obtain accuracies of 15cm, 30cm and 10cm in LOS conditions, respectively.

Table 2.1: Existing UWB TOA Positioning Technologies

Company	Bandwidth	Precision	LOS Accuracy	LOS Range	NLOS Results
Ubisense	0.5GHz	None	15cm	160m	None
Zebra	0.5GHz	None	30cm	200m	None
Time Domain	2GHz	None	2cm	354m	None
Decawave	0.5GHz	None	10cm	290m	None

These UWB ranging or localization systems do not provide precision results. The precision, which considers how consistently the system works, specifies the probability that the error is smaller than a certain error. Compared to the precision, the accuracy considers the value of mean distance errors. The precision results may give more sufficient information about the performance of the localization system than the accuracy results [43]. For example, the ranging error can be very small for most measurements, but a few measurements with very large errors may dominate the mean absolute error.

[3]http://www.zebra.com.
[4]http://www.timedomain.com.
[5]http://www.decawave.com.

Although the accuracy results in these experiments show the reliability of UWB for indoor localization, the uncertain and varying multipath propagation may result in TOA ranging instability and inaccuracy, especially in mobile cases. Some provided NLOS ranging or localization results, however, most of them did not. The performance of UWB TOA ranging in different NLOS conditions may be different. Sometimes, the UWB localization system may lack TOA measurements due to adverse NLOS conditions.

Among these researching groups and companies, Silva's team [56], Dalce's team [13] and *Decawave* consider the emerging IEEE 802.15.4-2011 UWB for localization purposes. The IEEE 802.15.4-2011 standard has become a recognized industry standard and provides a specification for both the physical layer and medium access control layer [10]. Employing a prototype fully IEEE 802.15.4a compliant transceiver technology, the world's first IEEE 802.15.4a UWB wireless packet was transmitted and successfully coherently received in real time in March 2009 [12]. This hardware boasts improved throughput, far superior energy efficient, better resistance to interference and multipath effects and a more secure channel when compared with existing WSN technologies such as IEEE 802.15.4 [47].

Although the reported performance of IEEE 802.15.4-2011 UWB based localization (11cm (Silva's team), 70cm (Dalce's team) and 10cm (*Decawave*) in LOS conditions) is sufficient for some aforementioned applications, it is not enough accurate for many potential application areas such as in-building robot navigation which requires 8cm accuracy. Localization based on UWB TOA ranging techniques in indoor environments is mainly affected by noise, multipath components and NLOS propagation [52].

2.3 Error sources of Time-based Ranging

This section reviews the error sources of TOA ranging in practical implementations, such as noise, multipath and NLOS propagation.

2.3.1 The Effect of Noise

The performance limits of TOA ranging have been analyzed by [71]. High signal bandwidth and SNR are beneficial for TOA ranging system. In UWB systems, the signal bandwidth is confirmed. The high SNR condition is a requirement for TOA ranging. However, in practice, the SNR is always affected by different noise sources, resulting in ranging inaccuracy and instability.

2.3.1.1 Analog to Digital Converter Noise

One noise source in the UWB systems might be the ADC noise. In [24], Gray et al analyzed the noise power generated by a saturating ADC. Due to its nonlinear nature, the ADC may contribute two noise powers to the device output, one due to quantisation effects and the other due to saturation effects.

Figure 2.1 (1) shows the transfer function of the ADC, where the saturation level V_{sat} has been set at k times the input root mean square (rms) voltage V_{rms}. Figure 2.1 (2) shows the resulting error signal $e(x)$, which is the difference between input and output of the ADC. Assuming $P(x)$ is the input signal, the total ADC noise power due to $e(x)$ can be computed from:

$$P_{ADCnoise} = 2\int_0^{\infty} e^2(x)P(x)dx \tag{2.1}$$

If the $P_{ADCnoise}$ have both quantization and saturation noise, the quantization noise

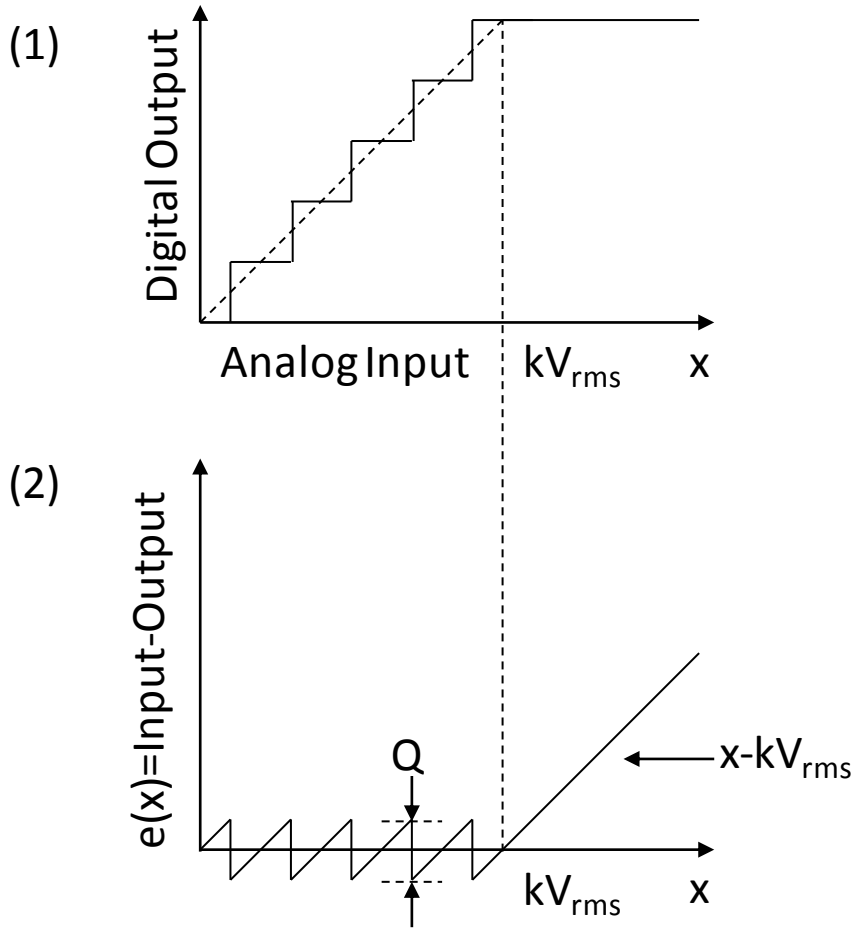

Figure 2.1: Analog to digital converter: (1) characteristic; (2) error signal.

power can be expressed as:

$$P_{qn} = 2\int_0^{kV_{rms}} e^2(x)P(x)dx \tag{2.2}$$

and, the saturation noise power is given by:

$$P_{sn} = 2\int_{kV_{rms}}^{\infty} e^2(x)P(x)dx = 2\int_{kV_{rms}}^{\infty} (x-kV_{rms})^2P(x)dx \tag{2.3}$$

The system generates saturation noise typically when the received signal strength exceeds the saturation level of the ADC.

Consider the quantization noise computation. If x_n represents the value of x at each

zero crossing of $e(x)$, then assuming that over any one interval $-Q/2 < x < Q/2$, $P(x) \cong P(x_n) = constant$, the P_{qn} can be rewritten as:

$$P_{qn} = 2\sum_n P(x_n) \int_{-Q/2}^{Q/2} x^2 dx = 2\sum_n P(x_n) \frac{Q^3}{12} = 2\frac{Q^2}{12} \sum_n P(x_n) Q \tag{2.4}$$

Then,

$$P_{qn} \cong 2\frac{Q^2}{12} \int_0^{kV_{rms}} P(x) dx \tag{2.5}$$

Where,

$$Q = \frac{kV_{rms}}{2^{M-1} - 1} \tag{2.6}$$

Where, Q is the quantization step size [24] (see Figure 2.1 (2)) and M is the number of ADC bits.

In practice, from equation (2.3), if the input is very strong, the probability of ADC saturation is high and the saturation noise power quickly increases. If the ADC has a large saturation level V_{sat}, from equation (2.2), the quantization noise power increases. From equation (2.5) and equation (2.6), the quantization noise can be reducing by increasing the M, or in other words, using a high resolution ADC.

2.3.1.2 Thermal Noise and Interference

The thermal noise generally comes from antenna circuits. In UWB systems, the thermal noise can be modeled by [17] as:

$$N_0 = kTemp_s(f) = k(Temp_A + (F(f) - 1)Temp_0) \tag{2.7}$$

Where, $k = 1.38 * 10^{-23} J/K$ is the Maxwell constant, $Temp_s$ is the noise temperature, $Temp_A$ is the antenna temperature, $F(f)$ is the noise figure, $Temp_0$ is the standard

temperature, 290K. The thermal noise is often regarded as AWGN.

The interference from other narrowband radios should take into account, but it is not a critical problem with multi-bit ADCs in UWB systems [60]. The UWB receiver can remove the interference in the digital domain or avoid it by choosing a band free from sources of interference.

2.3.2 The Effect of Multipath

The multipath is another error source of the TOA ranging system. When UWB signal propagates in a reflective indoor environment, a large number of multipath components are observable and uniformly spread over the input range of the ADC [26]. The channel impulse response may exhibit adjacent peaks with comparable amplitude to the correct peak. The first signal path may not be the strongest, resulting in TOA estimation inaccuracy.

In addition, these adjacent peaks do not overlap in time and therefore do not cancel out. As a result, more received power will be measured during the width of the transmitted pulse, that may generate saturation noise and decrease the SNR [61].

2.3.3 The Effect of Non Line of Sight Propagation

Deployed in indoor environments, UWB ranging systems have to face the challenges of NLOS propagation. An error source is the direct path excess delay caused by the propagation of a partially obstructed direct path component that travels through different obstacles [52]. In this situation, the TOF of UWB signals depends not only upon the traveled distance but also on the encountered materials. Since the propagation of electromagnetic waves is slower in some materials compared to air the signal arrives with excess delay, thereby introducing a positive bias in the range estimate.

Another error source of NLOS propagation is that the direct path is completely obstructed, and the receiver can only observe the reflected multipath components. In such a situation, the estimated TOF is larger than the true TOF. In NLOS conditions, the TOA estimate at the receiver includes a positive bias, mainly due to extra propagation delay. When all the multipath components are completely obstructed, the TOA measurements are absent at the receiver.

2.4 Approaches for Time-based Ranging

This section reviews approaches to improve the performance of the UWB TOA ranging system.

2.4.1 Automatic Gain Control Algorithm

Jing et al presents a double closed-loop automatic gain control (AGC) algorithm to decrease the saturation effect of the ADC [38]. This algorithm includes two AGC loops. The first AGC loop before synchronization module is used for coarse tuning. The second AGC loop after the sychronization module calculates the symbol power in preamble to approximate the reference power and is used for fine tuning. Simulation results show that the AGC algorithm can effectively improve the adjustable range of voltage-controlled amplifier (VGA) gain and convergence speed of the conventional AGC.

In [48], Olonbayar et al developed an automatic gain setting algorithm which measures the signal power every three symbols and sets the gain by the difference between the measured and the target powers. The simulation results suggest that the sensitivity can be improved by using higher resolution ADCs.

The advantage of the AGC algorithms is that they regulate the received signal power

and decrease the ADC noise. However, these AGC modules with limited adjustable range suffer from a large number of multipath components. Moreover, the AGC increases the power consumption of the system and makes the physical layer more complex. In addition, as the AGC modules only work inside the receiver circuit, they can not control the whole channel environment.

2.4.2 Threshold-based Time of Arrival Estimator

Theoretically, the TOA is equal to the time delay that maximizes the correlator output. However, the first arriving path may not be the strongest due to multipath components and NLOS conditions. Therefore, intelligent TOA estimator is required to mitigate the effects of multipath and NLOS propagation. Numerous TOA estimators have been developed for practical implementation, such as maximum and threshold criterion [16]. Let a received UWB signal be represented by [52]:

$$r(t) = \alpha s(t-\tau) + n(t) \tag{2.8}$$

Where, α is the channel coefficient and $n(t)$ is white Gaussian noise. The channel impulse response, which describes the reaction of the output of the ADC as a function of time, exhibits multipath components and noise. The channel impulse response can be represented as:

$$z(n) = \int_{n}^{(n+1)T} |r(t)|^2 dt \tag{2.9}$$

Where, $n \in 1,2,...N$ is the sampling index and N is the total number of received samples, T is the sampling period and $r(t)$ is the received multipath signal. With these samples available, the TOA estimator is then used to determine the first arrival path and its corresponding TOA.

The max criterion is based on the selection of the largest sample, n_k, in the channel impulse response, see Figure 2.2 [57]. The threshold criterion is based on an estimate of TOA sample, n_{TOA}, by comparing each element within the observation interval of the channel impulse response to a predefined threshold, see Figure 2.2. In particular, the TOA estimate is taken as the first threshold crossing event. The threshold value is usually defined using noise variance [18], [29]. For certain SNR ranges, the threshold based TOA estimators can obtain better ranging performance, when compared to the max criterion based TOA estimators [14].

A TOA estimator uses a search back (SB) technique, which is based on the detection of the largest sample and a search back procedure [28]. The search begins from the largest sample, and the search proceeds element by element backward in a window of length until the sample under test goes below a predefined threshold, and finally find out the search back path, n_{SB}, see Figure 2.2.

Compared to the threshold-based TOA estimator, the SB TOA estimator needs suitable values of threshold and window length. In [31], experimental results show that the simple threshold technique outperforms the search back technique. Although the threshold-based TOA estimator can obtain better ranging accuracy than other TOA estimators, it suffers from low SNR conditions [15]. However, high SNR conditions often cannot be met in UWB systems since they are primarily intended to operate in harsh multipath conditions with low SNR values.

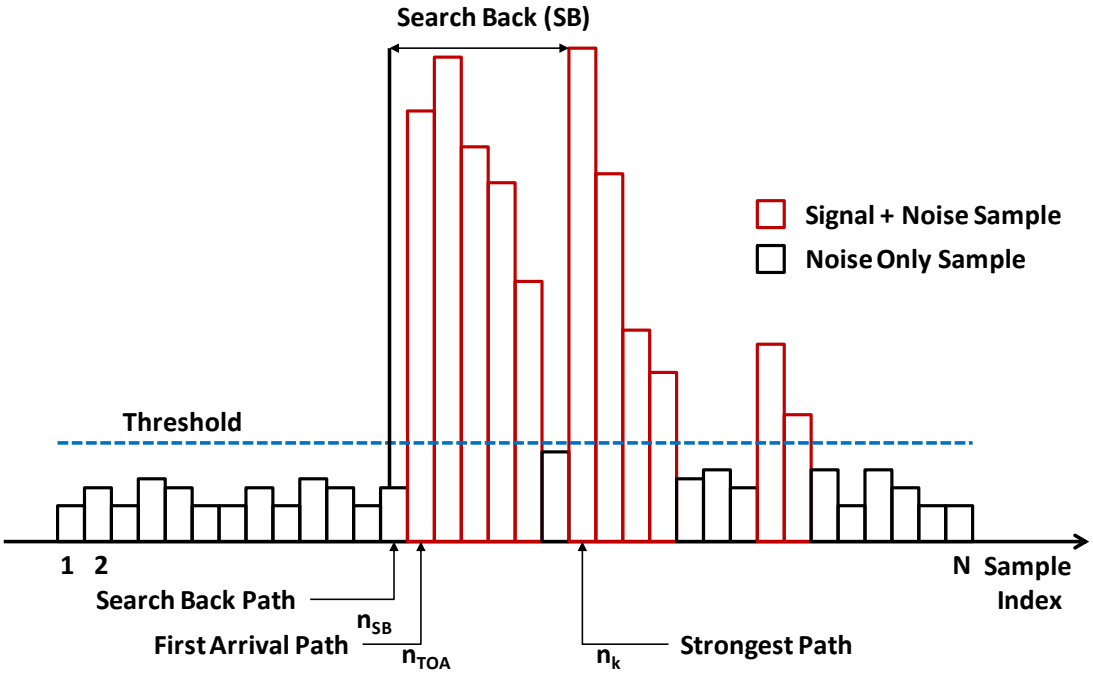

Figure 2.2: Time of arrival estimators.

2.5 Inertial Navigation

An inertial measurement unit (IMU) is a feasible option for indoor localization, because the system determines the location of an object using onboard measurements, capable of rejecting multipath effects and NLOS conditions [32]. The pure inertial navigation system (INS) uses an IMU consisting of gyroscopes, accelerometers and magnetometers to track orientation and position changes. The orientation of the IMU-frame of time step k is defined by three Euler angles: $\Psi_k = [\varphi, \theta, \psi]$ roll, pitch and yaw. The Euler angles can be derived by using angular velocity $\Omega_k = [\omega_x, \omega_y, \omega_z]^T$ and a set of known Euler angles at a given time as initial orientation. However, since $\tan\theta$ tends to infinity for pitch angles around $\pm 90^\circ$, the error becomes unbounded. To deal with this problem, quaternion algebra is generally used to present orientation with Euler parameters $q_k = [q_0, q_1, q_2, q_3]^T$ instead of Euler angles. The procedures of orientation and position are described as follows.

(1) Set the initial Euler parameters, e.g., $[1,0,0,0]^T$.

(2) Calculate the change of Euler parameter $\dot{q}_k$ using the angular rate data ω_k from gyroscopes.

$$\dot{q}_k = \frac{1}{2} q_k \otimes \omega_k \tag{2.10}$$

(3) Integrate to Euler parameters at current step with time duration dt.

$$q_{k+1} = q_k + \dot{q}_k dt \tag{2.11}$$

(4) Transform Euler parameters q_{k+1} back to Euler angles as follows.

$$\varphi = \arctan \frac{2(q_0 q_x + q_y q_z)}{1 - 2(q_x^2 + q_y^2)} \tag{2.12}$$

$$\theta = \arcsin(2(q_0 q_y - q_z q_x)) \tag{2.13}$$

$$\psi = \arctan \frac{2(q_0 q_z + q_x q_y)}{1 - 2(q_y^2 + q_z^2)} \tag{2.14}$$

(5) Calculate velocity by taking the first integral of acceleration in IMU-frame A_{k+1} with respect to dt. However, since acceleration sensor output $A_{k+1} = [a_x, a_y, a_z]^T$ contains the component of gravity, the acceleration due to the movement must be extracted. Here, the system assumes the IMU body frame is the same as earth-frame.

$$A_{k+1} = [a_x, a_y, a_z]^T - [0, 0, g]^T \tag{2.15}$$

Where, the gravity $g = 9.81 m^2/s$, and then the velocity is

$$V_{k+1} = V_k + A_{k+1} dt \tag{2.16}$$

(6) Calculate position of current IMU by taking the integral of velocity V_{k+1}.

$$P_{k+1} = P_k + V_{k+1} dt \tag{2.17}$$

(7) Repeat step (2) to (6) for all the time steps for position estimation of the object relative to a known starting point.

The bias and noise terms of inertial measurements cause errors in the calculated location [59]. As a result, the orientation and the location are only accurate and reliable for a short period of time. The integration drift is inherent to all the inertial navigation.

Many companies and groups have employed the inertial sensors for motion tracking applications. In [32], some work on inertial navigation were surveyed. The accuracy of these inertial navigation systems using MEMS sensors ranges from 0.62m to 1.321m.

In [49], Pittet et al used MEMS inertial sensors to track the human motion in indoor environments. The pure inertial navigation algorithm is used to compute the position. The error grows with time ranging from one meter to several meters.

In [51], Xsens MVN system uses biomechanical joint constraints based on human body models to eliminate the integration drift of each body segment in relation to the others. However, some inertial position drift is still present, typically between 1% and 2% of the traversed distance.

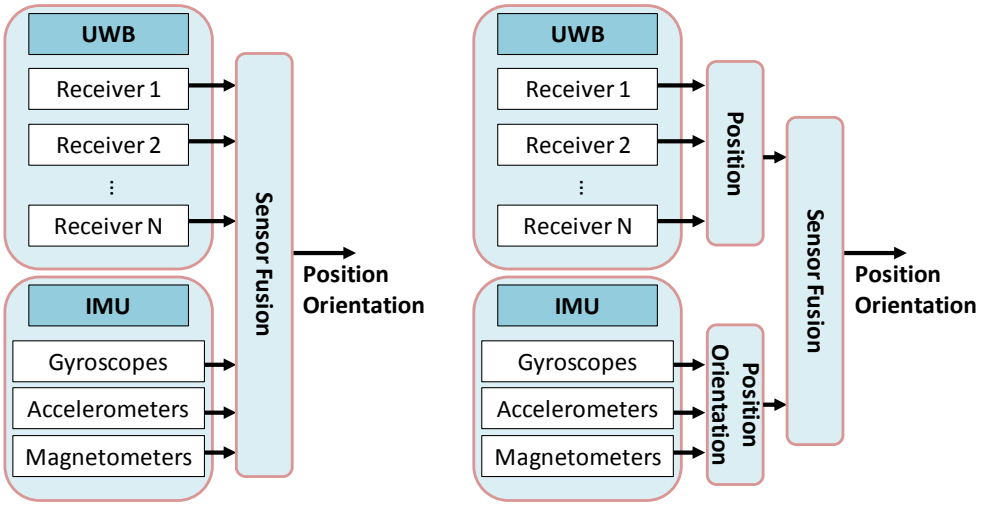

Figure 2.3: Sensor fusion architectures of hybrid UWB and IMU systems.

2.6 Hybrid UWB and IMU System

The advantages of hybrid UWB and IMU system are that the IMU can provide location information of an object when UWB measurements are absent due to range limitations or adverse NLOS conditions. In addition, a stable UWB ranging can help to eliminate the inherent integration drift of inertial navigation. The proposed hybrid UWB and IMU systems can be simply categorized into two cases according to the sensor fusion architecture: tightly-coupled and loosely-coupled, as shown in Figure 2.3.

In a tightly coupled architecture, the "raw" sensor measurements from the inertial sensors and the UWB receivers are directly used for sensor fusion, as illustrated in Figure 2.3 (a).

Bellusci et al proposed a tightly coupled hybrid UWB and IMU system for human motion tracking [6]. In this system, three tags (a tag is a UWB plus inertial sensors unit) are placed on the top of the head and on each of the feet of the actor for motion tracking. The readers, or UWB radio receivers, collect the "raw" sensor measurements of the tags with different sampling rates to estimate the position and orientation of the people using an extended Kalman filter (EKF). The EKF can handle the different sampling rates and a varying number of measurements straightforwardly [40]. The

EKF in this system was used to give an optimal estimate of the sensor kinematics using the inertial and UWB measurements. The localization error is only about 0.1m.

In [36], Hol et al presented a tracking system based on the combination of an UWB module and a MEMS IMU consisting of a 3D rate gyroscope and a 3D accelerometer. This system uses six synchronized UWB receivers at known locations that are attached to the ceiling to track a sensor unit which is mounted on a foot of the test subject. The tightly coupled architecture was considered in this system and an EKF was used to estimate position as well as orientation of the sensor unit while being reliable in case of multipath effects and NLOS conditions.

Another architecture for data fusion is a loosely coupled approach, as shown in Figure 2.3 (b). In a loosely coupled architecture, the position and orientation estimations are firstly performed independently by UWB and IMU, and then the already filtered quantities are fused to obtain final position and orientation measurements.

Youssef et al proposed a loosely coupled architecture for the hybrid UWB and IMU positioning system [69]. In this system, the pedestrian was holding a UWB transmitter in his right hand, and an IMU was attached to one of his ankles. The position estimates from two sub-systems were coupled to compute a final position using an EKF, which is employed to improve the tracking results. The accuracy can be improved to be 0.5m.

In [49], Pittet et al proposed an indoor navigation system based on UWB and MEMS inertial sensors to cope with multipath difficulties in indoor environments. In this system, the localization hardware uses only one IMU, attached to the UWB mobile, suspended together around the neck and carried on the thorax. A coupling filter based on an EKF was developed to compute pedestrian trajectories based on UWB location and MEMS inertial data. Therefore, this system can be regarded as a loosely coupled system. The localization accuracy ranges from 0.7m to 2.8m.

Sczyslo, et al proposed a hybrid tracking system combining a UWB system with inertial sensors [54]. A mixture of uncoupled and loose coupling architecture was taken

to integrate the IMU and UWB measurements. This system used a simple integration of position estimates from UWB trilateration and inertial navigation to find the final position of the IMU attached to a mobile unit.

These proposed hybrid UWB and IMU systems can improve the performance of UWB-only or IMU-only localization systems according to the experimental results, thanks to the tightly coupled and loosely coupled sensor fusion architectures. Compared to loosely coupled architecture, tightly coupled sensor fusion approach have two advantages. Firstly, preprocessing of measurements typically results in loss of information in loosely coupled approach, for example, when there are not enough TOA measurements for trilateration (at least three distance measurements). By directly using the sensor measurements through the tightly coupled approach, nothing has to be disregarded and maximal advantage is taken of the available information. Secondly, the available inertial measurements (such as orientation) gives accurate predictions of the UWB measurements, which allows for improved outlier detection without the need to rely on NLOS identification models for the mobile unit, as in the case of conventional UWB only positioning systems. In [74] and [73], Zwirello et al analyzed the performance of both tightly-coupled and loosely-couple integration schemes of a hybrid UWB and IMU system. Results showed that tightly-coupled data fusion is advisable for practical realization of the navigation system.

However, there are some limitations of these hybrid UWB and IMU systems. Firstly, these systems have implemented the two technologies in isolation where the IMU navigation and UWB ranging execute separately. This approach limits the achievable synchronization between the inertial sensor data and UWB ranging measurements, reducing the achievable accuracy of the system. Secondly, both loosely-coupled and tightly-coupled architectures are limited in that the nodes are incapable of exchanging inertial or positional data with other network nodes given the UWB channel is dedicated to ranging alone. As a consequence, they are limited in simultaneous local-

positioning and remote-tracking of the object. The solution in many cases is to supplement the system with an additional wireless technology for communications, which, in turn, increases the cost and size of the infrastructure and further complicates data synchronization.

2.7 Chapter Summary

In this chapter, the state of the art wireless localization technologies for indoor use were reviewed. Due to its large signal bandwidth property, UWB radio offers various advantages over other wireless technologies for localization purposes. The proposed ranging and localization systems using UWB or the emerging IEEE 802.15.4-2011 signals were summarized. Reported localization accuracies range from a centimeter to the order of decimeters. Although the obtained performance is sufficient for some aforementioned applications, many potential application areas have higher performance requirements. For example, in-building robot navigation requires eight-centimeter accuracy. However, these reports did not provide precision results, which are important information to evaluate the performance of the localization techniques, especially in mobile cases. Uncertain multipath propagation may cause instability and inaccuracy of instant ranging measurements.

Error sources in the time of arrival (TOA) based ranging system were reviewed. Noise, multipath components and NLOS situations introduce challenges for UWB TOA ranging. The noise sources come from both the hardware system and the channel environment. The automatic gain control modules can regulate the input of the ADC, but they suffer from a large number of multipath components. The threshold-based TOA estimator operates well in practical implementation, but it requires high signal to noise ratio (SNR) conditions. Nevertheless, high SNR conditions often cannot be met in UWB systems since they are primarily intended to operate in harsh multipath condi-

tions with low SNR values. Therefore, a robust algorithm is required that can stabilize the multipath channel to get an expected SNR.

Inertial sensors used for indoor localization were reviewed. Due to physical limitations inherent in MEMS inertial sensors, their measurements contain more or less bias and noise. The error of proposed inertial navigation system grows with time. Therefore an algorithm is required to improve the performance of inertial navigation in a long period of time.

In hybrid UWB and IMU systems, the IMU can provide location information of an object when UWB measurements are absent due to range limitations or adverse NLOS conditions; the stable UWB ranging can help to eliminate the inherent integration drift of inertial navigation. The tightly coupled sensor fusion can achieve a positioning accuracy of 0.1m. The best positioning accuracy of the loosely coupled sensor fusion is 0.5m. However, these proposed hybrid UWB and IMU systems are limited in mutual sharing data with other network nodes. As a consequence, they are limited in simultaneous local-positioning and remote-tracking of the object for some scenarios such as robot localization. Therefore a method is required for the hybrid UWB and IMU systems that can enable mutual sharing data with other network nodes.

Chapter 3

IEEE 802.15.4-2011 UWB Ranging Examination

This chapter provides an examination of the ranging capabilities of the IEEE 802.15.4-2011 UWB system in multipath environments. A ranging paradigm to measure the antenna to antenna distance is described using a symmetric double sided two way TOA protocol and a threshold-based TOA estimator. The world's first IEEE 802.15.4-2011 UWB transceiver prototype and ranging examination settings are introduced. The effects of different propagation conditions on the accuracy and precision of ranging measurements are analyzed.

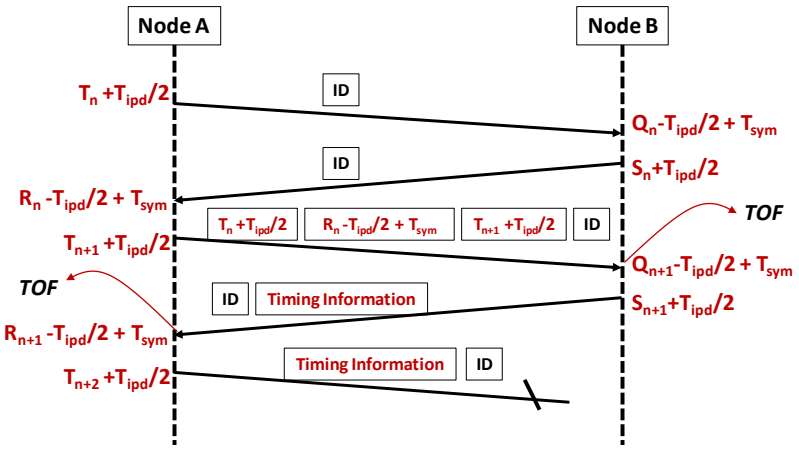

Figure 3.1: Ranging paradigm.

3.1 Ranging Paradigm

In practical implementation, successful TOA ranging relies on the system being able to accurately determine transmit and receive times for messages as they leave one antenna and arrive at the other antenna. This is needed for antenna-to-antenna TOF measurements and the resulting antenna-to-antenna distance estimation. An IEEE 802.15.4-2011 UWB signal is formed with a preamble, a start of frame delimiter (SFD), a physical header (PHR), and PHY service data unit (PSDU) [2]. A UWB frame having the ranging bit set in the PHR is defined as a ranging frame (RFRAME). The first UWB pulse of the first bit of the PHR is defined as the ranging marker (RMARKER) for TOA ranging implementation.

A ranging protocol called symmetric double sided two way TOA (SDS-TW-TOA) is utilized in this work to estimate the TOF [30]. Figure 3.1 depicts the TOF-based distance estimation which consists of following steps.

(1) Node A sends a ranging frame with ID, Node B in range can identify Node A. In this transmission, Node A notes the n^{th} transmit timestamp of the RMARKER, T_n. Half the internal propagation delay, $T_{ipd}/2$, is compensated to the T_n, in order to reflect the time instant at which the RMARKER leaves at the antenna.

(2) Node B receives the signal of Node A, and measures the n^{th} receive timestamp, Q_n. The SFD to PHR delay, T_{sym}, is added to Q_n, to compensate the receive-time of RMARKER. This is because of the Q_n measured in this work is the receive-time of the last symbol of the SFD. The half internal propagation delay, $T_{ipd}/2$, is then subtracted from the Q_n, in order to reflect the time instant at which the RMARKER arrives at the antenna.

(3) Node B responds after a specific turnaround time, and notes its transmit timestamp of the RMARKER, S_n, to which the $T_{ipd}/2$ is added.

(4) Node A senses the response of Node B, and measures its n^{th} receive timestamp, R_n.

Similar to the adjustment of receive-time of Node B, the T_{sym} is added to and $T_{ipd}/2$ is subtracted from the R_n.

(5) After a specific turnaround time, Node A sets the future transmit time of response, $T_{n+1}+T_{ipd}/2$, embeds timing values, $T_n+T_{ipd}/2$, $R_n-T_{ipd}/2+T_{sym}$, $T_{n+1}+T_{ipd}/2$ in message.

(6) Node B receives the signal from Node A on Q_{n+1}, and then has enough information to calculate the TOF according to the SDS-TW-TOA protocol as follows.

$$TOF_n = \frac{R_n - T_n - S_n + Q_n + Q_{n+1} - S_n - T_{n+1} + R_n + 4T_{sym} - 4T_{ipd}}{4} \tag{3.1}$$

Consequently, the antenna-to-antenna distance is calculated as

$$d_n = TOF_n \times c \tag{3.2}$$

(7) Node A calculates the TOF and distance on $n+1^{th}$ receive-time R_{n+1}, when it receives signal of Node B with timing information.

The SFD to PHR delay, T_{sym}, is a symbol duration which is a system parameter. The internal propagation delay, T_{ipd}, is a calibrated value. The T_{ipd} is characterized by tweaking the value of T_{ipd} until the average distance reported matches the real antenna-to-antenna distance measured with a tape measure. The value is then halved and compensated for transmit and receive timestamps. The transmit timestamps are made when the RMARKER is sent by the digital circuitry. The receive timestamps are estimated using a threshold-based leading path detection algorithm, which is described in next subsection.

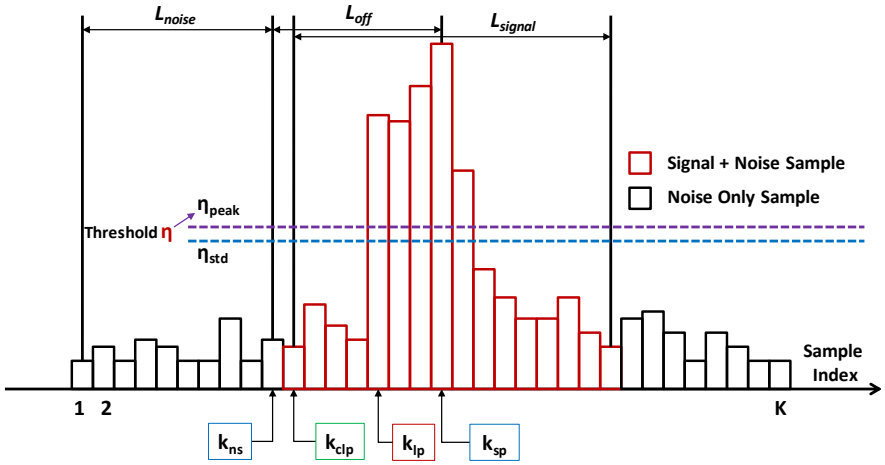

Figure 3.2: Threshold-based leading path detection algorithm.

3.1.1 Threshold-based Leading Path Detection

In this work, a threshold-based leading path detection technique is used to determine the TOA of the first arrival path from the channel impulse response (CIR) read, as shown in Figure 3.2.

The observation interval for the CIR is divided into $K = T_{ob}/T_{int}$ indices of the integration time T_{int}. In the CIR, note that the indices before the index k_{clp} contain only noise, whereas the remaining $K - k_{clp}$ indices may contain multipath, in addition to the noise. The index k_{clp} is the first byte of channel response read. The index of first arrival path is uniformly distributed in a length of L_{signal} from the index k_{clp}.

Firstly, we determine the threshold. Ideally, the strongest path, with index k_{sp}, is the first arrival path. The samples before index k_{ns} are noise only samples. $k_{ns} = k_{sp} - L_{off}$, L_{off} is denoted as noise start offset. The threshold value is calculated based on noise variance. The noise variance is measured from the noise only samples as

$$\sigma_n = \frac{\sum_{i=k_{ns}-L_{noise}}^{k_{ns}+L_{noise}} (P_i^{real} - P_a^{real})^2 + (P_i^{imag} - P_a^{imag})^2}{L_{noise}}; if(i<0), i = i+K; \qquad (3.3)$$

Where,

$$P_a^{real} = \frac{\sum_{i=k_{ns}-L_{noise}}^{k_{ns}+L_{noise}} P_i^{real}}{L_{noise}}; if(i<0), i = i+K; \tag{3.4}$$

$$P_a^{imag} = \frac{\sum_{i=k_{ns}-L_{noise}}^{k_{ns}+L_{noise}} P_i^{imag}}{L_{noise}}; if(i<0), i = i+K; \tag{3.5}$$

Where, L_{noise} is the length of noise samples, P_i^{real} and P_i^{imag} are the real value and imaginary value of the i^{th} noise sample, due to the complex-valued time-discrete input. P_a^{real} and P_a^{imag} are the average real and imaginary values of noise only samples, respectively. The standard deviation of the noise is calculated as

$$\sigma_{std} = \sqrt{\sigma_n} \tag{3.6}$$

And, the threshold based on σ_{std} is set as

$$\eta_{std} = (\alpha\sigma_{std})^2 = \alpha^2\sigma_n \tag{3.7}$$

In equation (3.7), α is a user specified parameter. The squared noise threshold η_{std} is used to compare with squared signal magnitude in the CIR. In order to avoid the selection of first arrival path from the noise only region, we use another threshold called peak threshold. The peak threshold η_{peak} is determined using the maximum value of the variance set as

$$\eta_{peak} = max\{(P_i^{real} - P_a^{real})^2 + (P_i^{imag} - P_a^{imag})^2, i = k_{ns} - L_{noise}, ..., k_{ns}\} \times \beta \quad if(i<0), i = i+K; \tag{3.8}$$

In the equation (3.8), β is a user specified parameter. As shown in Figure 3.2, the final threshold η for leading path detection is choosing the largest one between η_{std} and η_{peak} as follows.

$$\eta = max\{\eta_{std}, \eta_{peak}\} \tag{3.9}$$

Secondly, the leading path is detected by comparing each element of the CIR from the index $k_{ns}+1$ within the observation interval to the threshold. The leading path index, k_{lp}, is taken as the first threshold crossing event. If there is none above the η, the index k_{sp} with largest magnitude is then selected as the leading path index.

Finally, the receive-time is estimated as follows.

$$\hat{\tau} = \begin{cases} T_{clp} + T_{int} \times (k_{sp} - k_{clp}) + \dfrac{T_{int}}{2}, None > \eta \\ T_{clp} + T_{int} \times (k_{lp} - k_{clp}) + \dfrac{T_{int}}{2}, Others \end{cases} \tag{3.10}$$

Where, the T_{clp} is receive-time of the first byte of channel impulse response read, $\frac{T_{int}}{2}$ is compensated for TOA estimation of the leading path.

3.2 IEEE 802.15.4-2011 UWB Transceiver Prototype

In order to examine the ranging abilities of IEEE 802.15.4-2011 UWB in real-world indoor environments, this work employs the world's first IEEE 802.15.4-2011 compliant UWB transceiver prototypes, provided by *Decawave* Company, Dublin, Ireland [11].

The IEEE 802.15.4-2011 UWB transceiver prototype is realized using an Altera FPGA to capture the digital circuitry and discrete RF components to build the RF section. The PCB is 15cm wide and 25cm long, see Figure 3.3. The connector at the top of

the Figure 3.3 is a SMA connector, which is used to interface to the antenna. This UWB radio is equipped with a spline antenna. It has shown that using a spline shaped geometry for a printed monopole reduces pulse distortion and improves the fidelity factor [4], [39]. In practice the RF circuitry is covered in metal-can RF shields to improve performance. For physical robustness each prototype board is semi-enclosed in Perspex enabling it to be stood upright. The prototype is controlled via an SPI bus and is powered by connecting the power supply unit (PSU) to the 12VDC input port. As illustrated in Figure 3.4, at the transmitter part, the digital transceiver sends a signal which is then converted to be an analogue signal. Finally, at the analogue front end, the UWB pulse is shaped which is then radiated through an antenna. At the receiver part, the received analogue signal is converted to be a digital signal for signal synchronization and data detection.

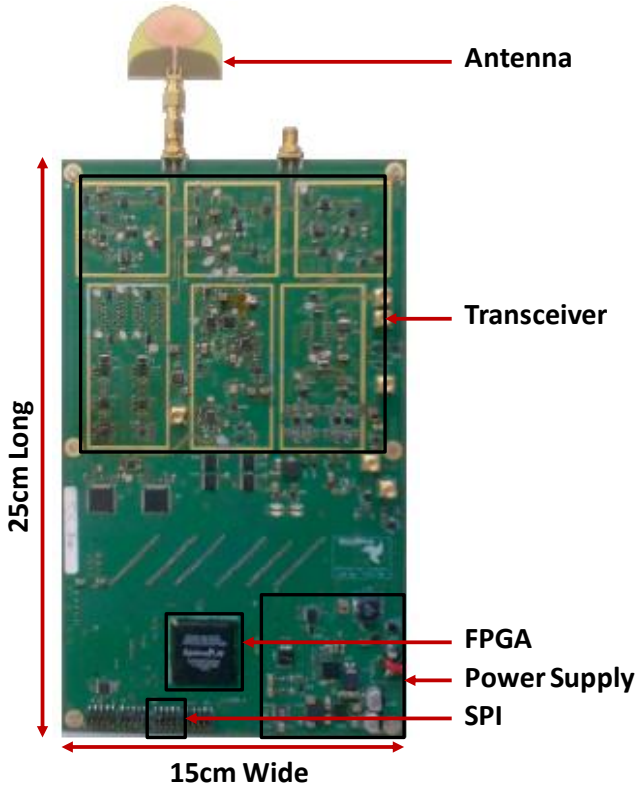

Figure 3.3: IEEE 802.15.4-2011 UWB prototype.

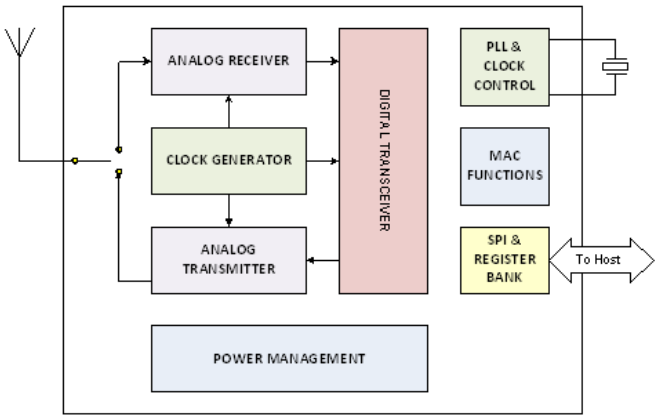

Figure 3.4: Functional block diagram.

3.2.1 Signal Settings

The IEEE 802.15.4-2011 UWB signal parameters are listed in Table 3.1. The channel band number is set to be 2, so radio works on a center frequency of 4GHz, according to the IEEE 802.15.4-2011 standard [3]. The signal bandwidth is 500MHz. The preamble code index is 4 with corresponding length-31 codes of $\{0000+1-100-100-1+1+1+1+10+1-1+1000+10-10+1+10\}$, and preamble length is 1024. The start of frame delimiter (SFD) uses length-8 codes of $\{0+10-11+100-1+1\}$. The pulse repetition frequency (PRF) is 16MHz, and the data rate is 850Kb/s. The

Table 3.1: IEEE 802.15.4-2011 UWB signal parameters

IEEE 802.15.4-2011 Channel Number	2
Preamble Code	0000+1-100-100-1+1+1 +1+10+1-1+1000+10-10+1+10
Start of Frame Delimiter (SFD) Code	0+10-11+100-1+1
Preamble Length	1024
Pulse Repetition Frequency (PRF)	16MHz
Data Rate	850Kbits/s
Center Frequency	4 GHz
Signal Bandwidth	500 MHz
Transmit-Power	-13.5dBm

transmit-power is set to be -13.5dBm. The signal spectrum was measured by an agilent spectrum analyzer, as shown in Figure 3.5. The effective bandwidth is about 500MHz, from a lower frequency of 3.75GHz to an upper frequency of 4.25GHz, is observed

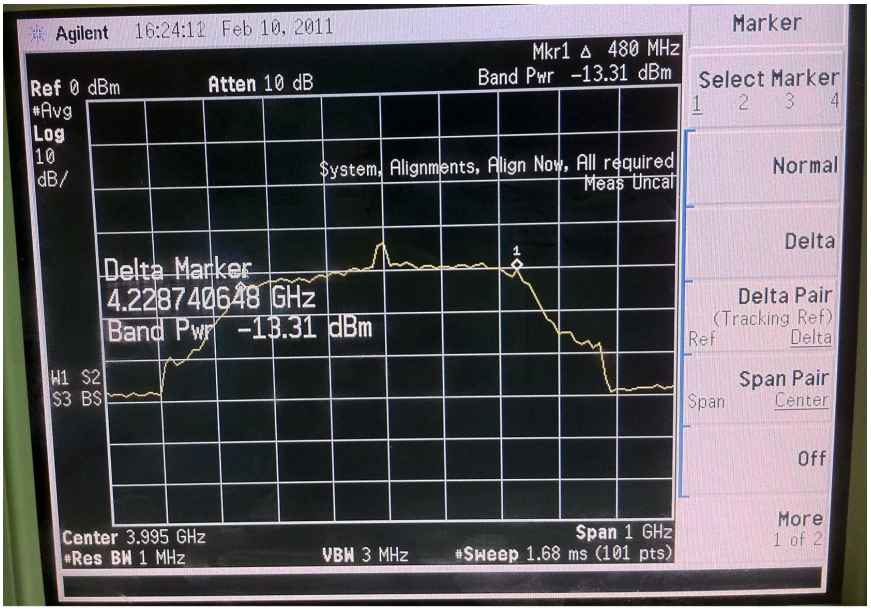

Figure 3.5: IEEE 802.15.4-2011 UWB signal spectrum.

with 1MHz resolution bandwidth. The band power is -13.31dBm at the 4.22GHz point, from which the transmitting power is about 0.047mW. Therefore, this radio complies with the emission limit set by the FCC [1].

3.2.2 Ranging Settings

The IEEE 802.15.4-2011 UWB transceivers perform the ranging paradigm using equation (3.1), equation (3.2) and equation (3.10); and are capable of capturing channel impulse response (CIR). Ranging parameters are listed in Table 3.2.

Table 3.2: IEEE 802.15.4-2011 UWB ranging parameters

Observation Interval, T_{ob}	992ns
Integration Time, T_{int}	1 ns
Signal Length, L_{signal}	128 ns
Noise Only Length, L_{noise}	256 ns
Noise Start Offset Length, L_{off}	128 ns
User Specified Parameter for η_{std}, α	5.5
User Specified Parameter for η_{peak}, β	1.5
Turnaround Time	300ms
SFD to PHR Delay, T_{sym}	992ns
Speed of Light, c	299702547m/s
Internal Propagation Delay, T_{ipd}	277.850ns

Each CIR captured at the receiving time is sampled at integration time T_{int} of 1ns over an observation interval T_{ob} of 992ns. The signal length L_{signal} is set to be 128ns from the measured index k_{clp}. The noise only length L_{noise} is 256ns and the noise start offset length L_{off} is 128ns. User specified parameters for threshold determination, α and β, are set to be 5.5 and 1.5, respectively in this ranging application. The user specified parameters are application dependent parameters. The turnaround time used for SDS-TW-TOA ranging protocol is 300ms. The SFD to PHR Delay T_{sym} is 992ns. We use the speed of light c of 299702547m/s to calculate the distance. The internal propagation delay T_{ipd} is using a calibrated value of 277.850ns.

3.3 Examination Settings

A block diagram of the ranging system is shown in Figure 3.6. The ranging software is built to run on laptop and use two cheetah SPI host adapters, one each to talk to the each UWB radio's SPI. To perform the ranging estimation between two UWB transceivers using symmetric double sided two way TOA (SDS-TW-TOA) protocol, one plays as leader, and the other plays as follower. The leader takes the lead. Both measure the antenna-to-antenna distance in between based on the SDS-TW-TOA ranging messages.

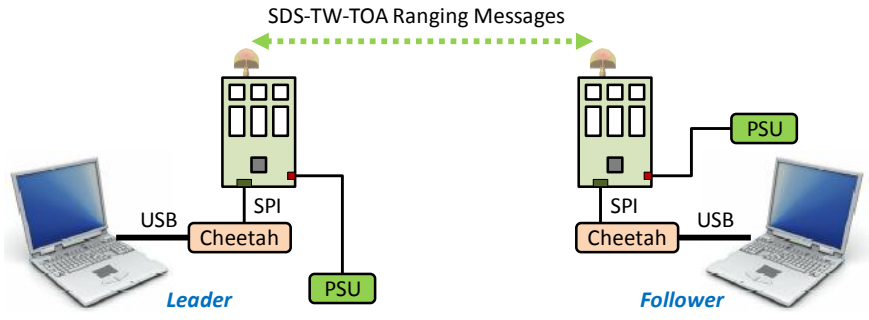

Figure 3.6: A block diagram of the measurement apparatus.

Ranging examination was made on one floor of an office building having the floor plan shown in Figure 3.7, and a typical measurement scenario is shown in Figure 3.8. Walls around offices are constructed of reinforced concrete. Some partition walls are used

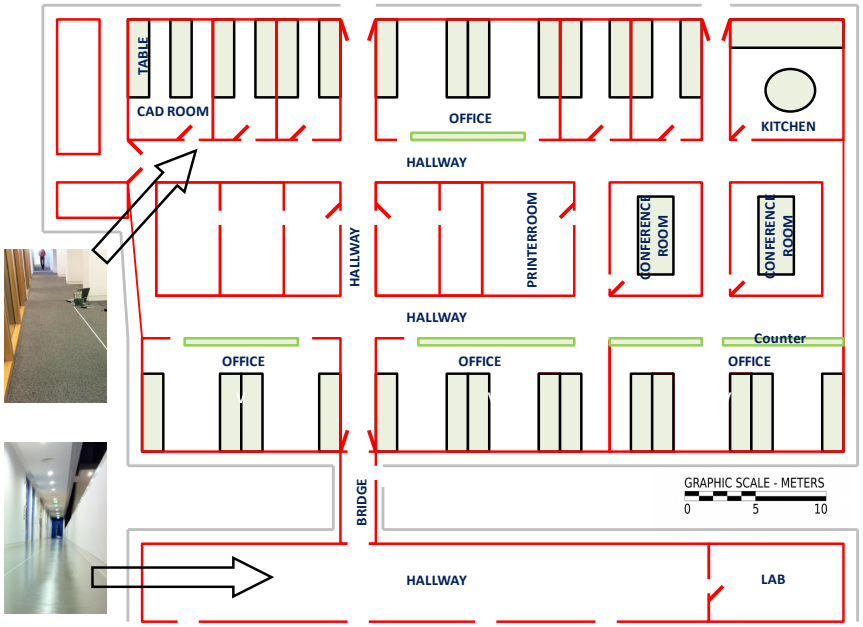

Figure 3.7: Measurements were taken in different rooms and hallways to capture different propagation conditions.

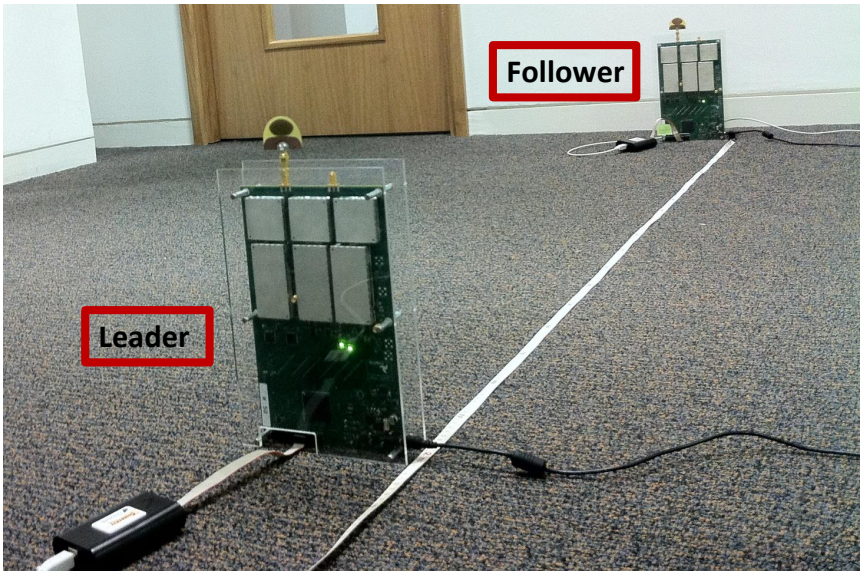

Figure 3.8: The measurement setup for ranging at the hallway of the second floor, block B, Tyndall National Institute.

to insulate the office from the hallways. Some offices use glass walls through which the people can see the hallways. The leader is kept stationary in specific locations of the building, while the follower moves to specific positions within transmission range. Different propagation conditions were considered during experiments. More than 200 ranging measurements were recorded from each testing point.

3.3.1 Propagation Condition Considerations

IEEE 802.15.4-2011 UWB channel models have been segregated into LOS and NLOS propagation conditions [46]. This is useful for simulating how a system will work in different environments. However, it cannot extrapolate how well a system will work in the real world where we get a mixture of LOS and NLOS channels. From a comprehensive review of the available channel measurements and reports, it is clear that two distinct NLOS cases exist [46], [66], [16]. A case where the signal is mainly obstructed by relatively low attenuation materials such as glass, lockers and doors, and a case where it is mainly obstructed by high attenuation materials such as multiple concrete walls. Therefore, the UWB channel is comprised of three different propagation scenarios as LOS, soft-NLOS, hard-NLOS conditions.

(1) LOS. LOS propagation only occurs when a direct line of sight between the transmitter and receiver exists, for example, in a hallway or an open field. The LOS path loss exponent was measured which ranges from 1.3 to 1.8 [46]. In the LOS channel, ideally, the line of sight component is the strongest path, other received multipath components have a lower power than the LOS path. Therefore, the strongest path ideally is the first arrival path. However, in practice, the first arrival path may not be the strongest due to the presence of the large number of multipath components.

(2) Soft-NLOS. This condition occurs when the line of sight path is obstructed by material with relatively low attenuation or by a combination of these materials. It represents the most common channel model over the distances of interest and takes into account most attenuation excluding that which is caused by multiple concrete walls. The soft-NLOS path loss exponent was found to be 2.2 in [19]. In this case, the propagation time of these signals depends not only upon the traveled distance but also on the encountered materials. Since the propagation of electromagnetic waves is slower in some materials compared to air the signal arrives with excess delay, thereby introducing a positive bias in the range estimate.

(3) Hard-NLOS. The hard-NLOS channel is attenuated severely due to a multiple concrete walls in the environment. One hard-NLOS model is the ULTRAWAVES (Wisair) model [67]. The path loss exponent was found to be 3.8. In this case, receiver can only observe NLOS components, resulting in estimated distances larger than the true distance.

3.3.2 Distance Types

Three distance types are considered in this work. The first one is variance ranging which is calculated as follows.

$$\bar{d} = \frac{\sum_n^N d_n}{N}, n = 1,2,...N \tag{3.11}$$

Where, N is the total number of the measured instant distances. d_n is the instantaneous distance.

The variance distance can be used for stationary ranging, but is not good for the mobile ranging scenario. Instant distance is the advisable for mobile cases. According to the ranging parameters as shown in Table 3.3, the turnaround time is set to be 300ms for the SDS-TW-TOA ranging protocol. The instant ranging duration is therefore about 0.6s. Hence, the instant distance d_n can be calculated using the equation (3.2). Due to the "raw" instant distance measurements may have large errors, a maximum and minimum filter (MMF) can be used as follows.

$$d_k = \frac{\sum_n^{n+10} d_n - max(\sum_n^{n+10} d_n) - min(\sum_n^{n+10} d_n)}{8}, n = 1,2,...N; k = n+10; \tag{3.12}$$

Where, the maximum and minimum values in a set of distance measurements are filtered. Integer 10 means the latest 10 instant ranging measurements. It is therefore the

first MMF distance measurement is calculated when 10 instant distance measurements are obtained.

3.3.3 Performance Evaluation Tools

The accuracy is defined as how far the estimated distance of the object is away from its actual distance (e.g. 1m accuracy). The precision specifies the probability that the ranging error is smaller than a certain error (e.g. 95% precision within 1m).

The ranging accuracy can be quantified by means of mean absolute error (MAE). In this work, the MAE is approximated by the sample mean of the absolute error as follows.

$$MAE = \frac{\sum_n^N d_n - d}{N}, n = 1, 2, ...N \tag{3.13}$$

Where, d is the true distance. The MAE which only considers the value of mean distance errors, may not give sufficient information about the performance of the ranging system. For example, the ranging error can be very small for most measurements, but a few measurements with very large errors may dominate the mean average error. Compared with accuracy the precision considers how consistently the system works, which is a measure of the robustness of the positioning technique as it reveals the variation in its performance over many trials [43]. Usually, the cumulative probability functions (CDF) of the distance error is used for measuring the precision of a system. The probability that the ranging error is smaller than a certain threshold x can be specified for all threshold values as follows.

$$CDF = P\{|d_n - d| \leq x\} \tag{3.14}$$

When two ranging techniques are compared, if their accuracies are the same, we prefer

the system with the CDF graph, which reaches high probability values faster, because its distance error is concentrated in small values. In practice, CDF is described by the percentile format. For example, one system has a ranging precision of 90% within 10cm (the CDF of distance error of 10 m is 0.9), and 95% within 20cm; another one has a precision of 50% within 10cm and 95% within 20cm. It could choose the former system because of its higher precision.

3.4 Experimental Results

The ranging experiments are implemented in different mulitpath environments such as library, indoor hallway, outdoor hallway and courtyard. In soft-NLOS conditions, the glass wall, plastic chair, counter, and wood door are selected as the obstacles. The concrete wall is used to give rise to the hard-NLOS propagation. Typical measurement scenarios are shown in Figure 3.9.

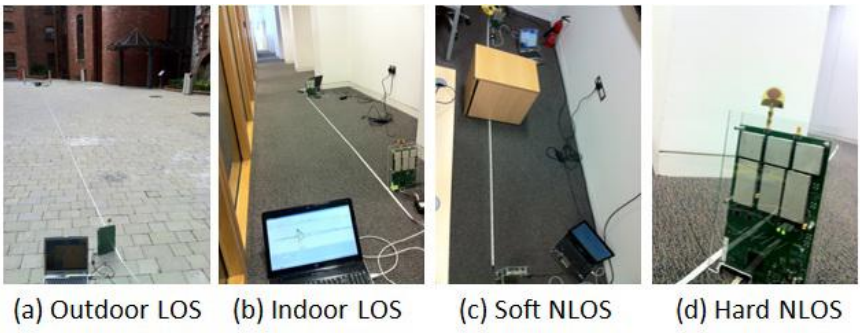

Figure 3.9: The setup of ranging experiments in different conditions.

3.4.1 Channel Impulse Responses

In order to accurately reflect reality in LOS, soft-NLOS and hard-NLOS propagation conditions, the leader and the follower are kept stationary with a direct line of sight distance of 10m. Then, a counter was placed between the two UWB transceivers to form a soft-NLOS propagation condition. The wood counter ($Length(L) \times Width(W) \times$

$Height(H) : 40cm \times 50cm \times 70cm$). In order to observe the hard-NLOS propagation, a concrete wall ($L \times W \times H : 5m \times 65cm \times 3cm$) is used as the obstacle. The system parameters used in these different conditions are all the same as listed in Table 3.1 and Table 3.3. The channel impulse responses (CIRs) captured from these propagation conditions are shown in Figure 3.10.

The magnitude of the visible largest path decreases from LOS to soft-NLOS, and then Hard-NLOS. This is because of the signal attenuation in the soft-NLOS condition is higher than the LOS propagation, but is lower than the hard-NLOS propagation. Some adjacent peaks exhibit in the LOS and the soft-NLOS CIRs.

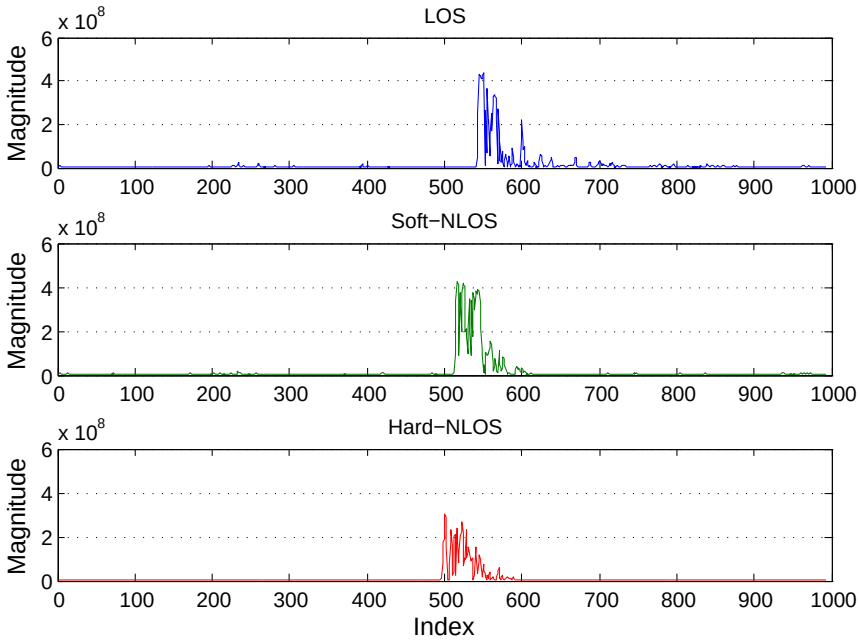

Figure 3.10: Channel impulse responses captured in LOS, Soft-NLOS and Hard-NLOS conditions after 10m transmission.

3.4.2 Accuracy

This subsection presents the accuracy results in LOS, soft-NLOS and hard-NLOS propagation conditions.

3.4.2.1 LOS

Figure 3.11 shows the ranging errors measured in LOS conditions in different places. The ranging error is less than 20cm.

In the library ($length(L) \times width(W) \times height(H) : 11m \times 7m \times 3.5m$), there are few chairs, tables around the UWB transceivers, and the maximum ranging error is 15cm at a distance 10m. The ranging error gradually increases from 1m (4cm error), 5m (13cm error), 7m (14cm error) to 10m (15cm error). In the outdoor hallway ($L \times W : 12m \times 2.5m$), there are only walls at both sides of the UWB transceivers, and the maximum ranging error of 18cm at a distance of 10m. The ranging error gradually decreases from 1m (11cm error), 2m (9cm error) to 5m (6cm error); and then increases from 6m (10cm error) to 10m (18cm error). In the indoor hallway ($L \times W \times H : 12m \times 1m \times 3.5m$), where there are some doors, WIFI sites and walls around the UWB transceivers, as shown in Figure 3.9 (b), the maximum ranging error is 11cm at a distance of 2m. The ranging error distribution at different distances is irregular. It looks like that gradually decreases from 1m (11cm error), 3m (10cm error), 5m (2cm error), and then increases from 6m (6cm error), 7m (10cm error), but finally decreases at 10m (2cm error). In outdoor courtyard where only sources of signal reflection are the operators, the equipment and the ground, as shown in Figure 3.9 (a), the maximum ranging error is 12cm at the distance of 8m. The same as the result of indoor hallway, its ranging error is irregular with distance increasing.

3.4.2.2 Soft-NLOS Test

In soft-NLOS ranging, experiments are implemented at three meters distance. Different obstacles, such as glass, chair, counter and door, were used to create the soft-NLOS propagation conditions. An example of soft-NLOS experiment scenario is shown in Figure 3.9 (c). The counter, made of wood, obstructs the signal's line of sight. Figure 3.12 shows the average measured distances collected in soft-NLOS propagation con-

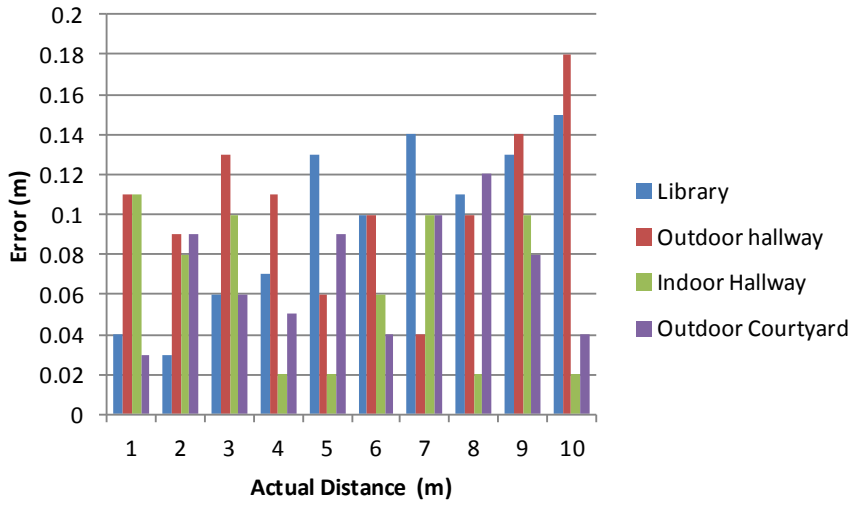

Figure 3.11: Accuracy in LOS conditions.

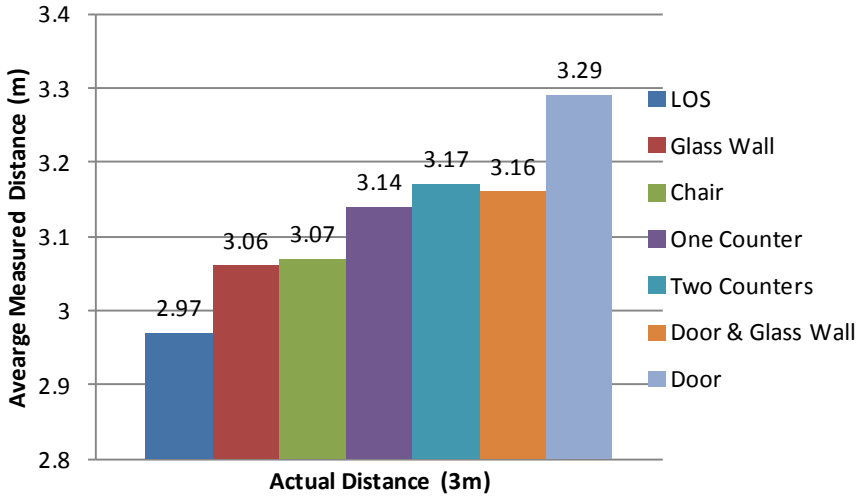

Figure 3.12: Average measured distance in Soft-NLOS conditions.

ditions. The actual distance is 3m. An average LOS ranging measurement shown here is for comparison.

In LOS condition, the ranging error is 3cm. When signal propagates through a glass wall ($length(L) \times width(W) \times height(H) : 1m \times 1cm \times 3m$), the ranging error is 6cm. A chair ($L \times W \times H : 45cm \times 5cm \times 1m$) causes 7cm error. When signal propagates through a counter ($L \times W \times H : 40cm \times 50cm \times 70cm$), the ranging error is 14cm. The use of two counters generates 17cm error. When signal propagates through a mixture of door ($L \times W \times H : 1m \times 5cm \times 3m$) and glass wall, the ranging error is 16cm. If there is no glass wall between two UWB transceivers, only the door causes 29cm ranging

error. This is due to the obstacles having different thickness and material permittivity. These materials with relatively low attenuation cause a little bigger error in ranging than the air (3cm).

3.4.2.3 Hard-NLOS Test

The hard-NLOS ranging experiments were taken in the second floor of Block B, Tyndall National Institute. A concrete wall was selected as the obstacle to create the hard-NLOS propagation. An example of hard-NLOS ranging scenario is shown in Figure 3.9 (d). To find out the worst case of hard-NLOS propagation, we moved the follower to some specific locations, from which the UWB signals are obstructed by one wall, three walls, and eleven walls, with distance increasing. Figure 3.13 shows the average measured distances in hard-NLOS propagations. When propagating through one wall, the average ranging error is 26cm. Three walls cause 56cm ranging error. Four walls and multi obstructions cause 87cm and 78cm ranging errors, respectively. Particularly, there is no ranging measurement at 38m point, from which the leader signal propagates through eleven walls. These results show that the hard-NLOS propagation adds irregular positive bias to the range estimate, and the high attenuation materials may cut off the signal transmission.

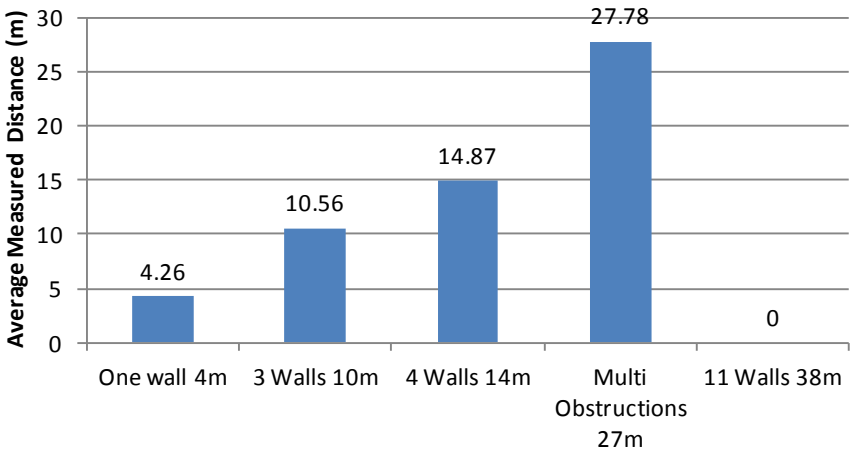

Figure 3.13: Average measured distance in Hard-NLOS conditions.

3.4.3 Precision

The instant ranging experiments were implemented in the second floor of Block B, Tyndall National Institute, as shown in Figure 3.7. The distance measurements were collected in LOS, soft-NLOS and hard-NLOS ranging. The typical measurement scenarios are shown in Figure 3.9 (b),(c),(d). Each ranging scenario includes 30 testing points, more than 200 measurements at each point. Hence, totally, 6000 measurements for each propagation condition. In this work, the precision of instant distance measurements is analyzed using the empirical cumulative distribution function (CDF). The 1m and 10cm are selected as the thresholds. Figure 3.14 shows the CDF of the precision of instant distance measured using equation (3.2). The blue line shows the precision of instant ranging in LOS conditions. The ranging error between -1m to 1m (see horizontal axis) occurs in 96% (see vertical axis) of the measurements. However, the ranging error between -0.1m to 0.1m (see horizontal axis) occurs in 52% (see vertical axis) of the measurements. The green line shows the precision of instant ranging in soft-NLOS conditions. The ranging error between -1m to 1m occurs in 100% of the measurements. The ranging error between -0.1m to 0.1m occurs in 33% (see vertical axis) of the measurements. The precision in soft-NLOS condition is worse than LOS condition. The red line shows the precision of instant ranging in hard-NLOS conditions. The ranging error between -1m to 1m occurs in 80% of the measurements. The ranging error between -0.1m to 0.1m occurs in only 15% (see vertical axis) of the measurements.

Table 3.3: Summary of instant ranging results

	LOS	Soft-NLOS	Hard-NLOS
Measurements	6000	6000	6000
Accuracy $> 1m$	96%	100%	80%
Accuracy $> 10cm$	52%	33%	15%

Table 3.3 shows the comparison of instant ranging measurements collected in the LOS, soft-NLOS and hard-NLOS propagation conditions. In LOS conditions, the instant

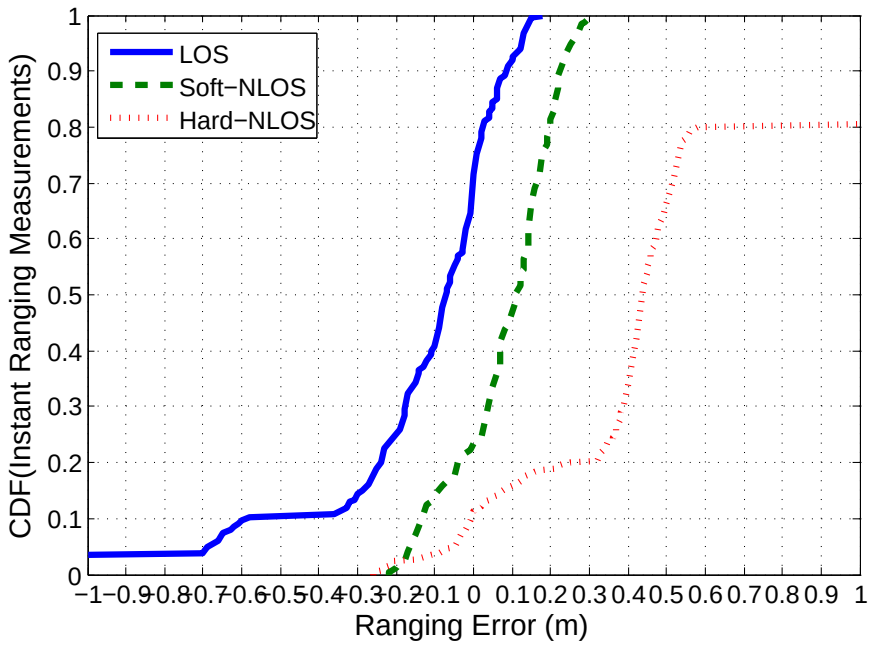

Figure 3.14: Precision of instant ranging measurements in LOS, Soft-NLOS, Hard-NLOS conditions.

ranging error was below 1m/10cm occurs in more than 96%/52% of the 6000 measurements, respectively. In soft-NLOS conditions, the instant ranging error below

Table 3.4: Summary of MMF based instant measurements

	LOS	Soft-NLOS	Hard-NLOS
Measurements	6000	6000	6000
Accuracy $> 1m$	100%	100%	80%
Accuracy $> 10cm$	48%	40%	20%

1m/10cm occurs in more than 100%/33% of the 6000 measurements, respectively. In hard-NLOS conditions, instant ranging error below 1m/10cm occurs in more than 80%/15% of the 6000 measurements, respectively. The percentage error below 10cm of soft-NLOS ranging (33%) is less than the LOS ranging (52%), but is higher than the hard-NLOS ranging (15%).

Figure 3.15 illustrates the CDF of the MMF based instant ranging by using the equation (3.12). Table 3.4 shows the comparison of the MMF based instant ranging measurements collected in the LOS, soft-NLOS and hard-NLOS propagation conditions. In LOS conditions, the ranging error of MMF based instant measurements was

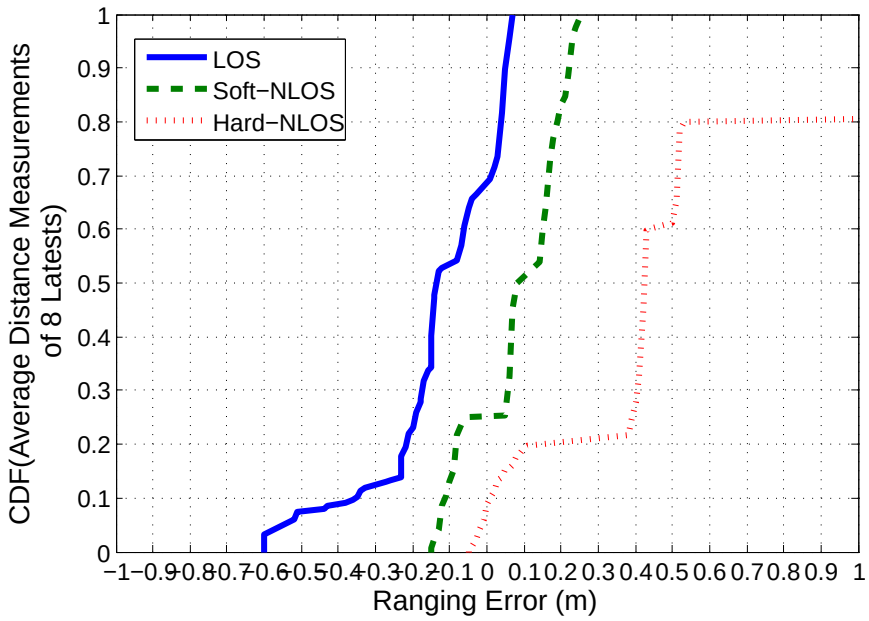

Figure 3.15: Precision of MMF instant ranging measurements in LOS, Soft-NLOS, Hard-NLOS conditions.

below 1m/10cm occurs in more than 100%/48% of the 6000 measurements, respectively. In soft-LOS conditions, the ranging error below 1m/10cm occurs in more than 100%/40% of the measurements, respectively. In hard-LOS conditions, the ranging error below 1m/10cm occurs in more than 80%/20% of the measurements, respectively. The percentage of error below 10cm of soft-NLOS ranging (40%) is less than the LOS ranging (48%), but is higher than the hard-NLOS ranging (20%).

From Figure 3.14 and Figure 3.15, the percentage of ranging measurements with positive biases in soft-NLOS and hard-NLOS propagation conditions, 80%, is higher than the one in LOS condition, 30%. This is mainly because of the direct path excess delay is incurred by propagation of the partially obstructed direct path through different materials in soft-NLOS conditions; and in hard-NLOS conditions, the direct path to certain receivers is completely obstructed, and only received signals from reflections are captured. By employing the MMF based ranging, the accuracy is improved and some outliers are filtered by comparing the results in Table 3.3 and Table 3.4. In the LOS conditions, the worst case of instant measurement is >1m, while the worst case of MMF based ranging is 0.6m.

3.5 Chapter Summary and Conclusion

In this chapter, a ranging paradigm was described based on a symmetric double sided two way TOA (SDS-TW-TOA) protocol and a threshold based leading path detection algorithm. The threshold was calculated based on the noise variance measured from the channel impulse response.

Employing this ranging paradigm, the IEEE 802.15.4-2011 UWB based ranging was examined in multipath environments. Three propagation conditions were considered including LOS, soft-NLOS, and hard-NLOS. The LOS, soft-NLOS and hard-NLOS conditions were determined according to the different path loss exponents. The soft-NLOS situation happens typically when the signal propagates through relatively low attenuation materials, such as glass, counter and door. The hard- NLOS situation often occurs when the signal propagates through high attenuation materials, such as concrete walls. The ranging experimental results were reported. The achievable accuracies were 0.2m in LOS, 0.3m in soft-NLOS, and 1m in hard-NLOS. In addition, the IEEE 802.15.4-2011 UWB ranging system had precisions of 52% within 10cm in LOS condition, 33% within 10cm in soft-NLOS condition, and 15% within 10cm in hard-NLOS condition. In particular, the ranging system turned off at a distance of 38m when the signal propagated through 11 concrete walls.

The IEEE 802.15.4-2011 UWB ranging system can get one meter and even sub-meter level accuracy. However, the precision of instant ranging measurements was low compared to an expected confidence level (e.g., 90% with 10cm). Moreover, the ranging measurements in LOS conditions were not stable, even though sometimes the system can get centimeter level accuracy. In addition, NLOS conditions caused different ranging errors when signal propagates through different obstructions. From the soft-NLOS condition to hard-NLOS conditions, the ranging accuracy decreases. Sometimes, there are no ranging results when UWB signal propagated through 11 concrete walls.

Chapter 4

Bilateral Transmitter Output Power Control Algorithm

In order to improve the performance of IEEE 802.15.4-2011 ultra wideband (UWB) ranging system through time of arrival (TOA) technique, this chapter presents a bilateral transmitter output power control algorithm which can stabilize the multipath channels between UWB transceivers. In this chapter, the features of IEEE 802.15.4-2011 UWB in multipath propagation are described. The relationship between transmit power, transmission range and the signal to noise ratio (SNR) is extracted. Based on this multiapth model, the operation of the bilateral transmitter output power control algorithm is then presented. Finally, the experimental results to evaluate this approach are reported.

4.1 Introduction

In IEEE 802.15.4-2011 UWB system, as illustrated in Figure 4.1, at the transmitter side, channel coding, modulation and pulse generation are done digitally in the baseband. Then, the digital transceiver sends data, the digital analogue converter (DAC)

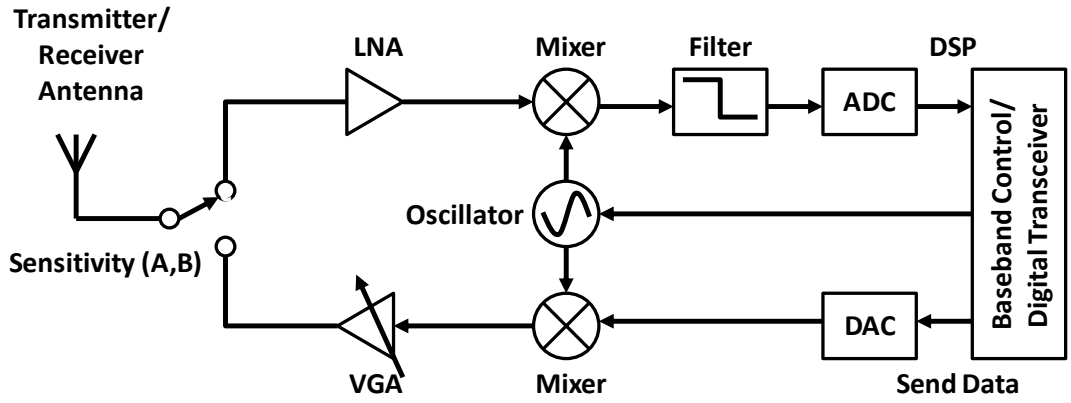

Figure 4.1: UWB transceiver.

outputs an analogue signal. The mixer is used to shift 2ns UWB pulses to a specific center frequency, such as 4GHz. After that, a variable-gain or voltage-controlled amplifier (VGA) is designed to vary the signal gain to a controlled voltage. The UWB signals are finally radiated through the antenna.

At the receiver side, at the antenna, the received signal dynamic range lies between A and B dBm. A is the largest sensitivity, and B is the weakest sensitivity. The low noise amplifier (LNA) following the antenna is to amplify the signal by a fixed gain. The amplified signal is then down-converted and filtered. The ADC module is to convert the analogue signal to a digital signal for digital signal processing.

In multipath propagation, the channel communication quality is affected by a number of noise sources from both the hardware system and the channel environments, such as the ADC noise, thermal noise and multipath components. However, there is no model that can effectively describe the relationship between the channel communication quality and the noise sources.

The SNR model can be used to describe the channel communication quality. Some SNR models are obtained for a given received signal power and the thermal noise only [52]. However, these SNR models can not exactly describe the channel communication quality in practical implementations.

Employing the IEEE 802.15.4-2011 UWB transceiver [11], two UWB signals with

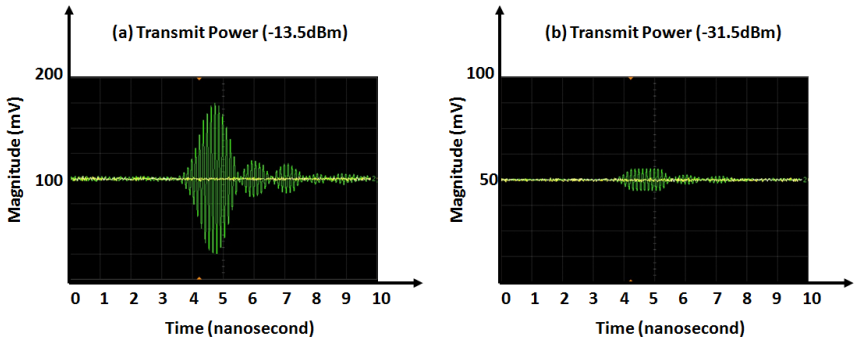

Figure 4.2: IEEE 802.15.4-2011 UWB pulses at the antenna.

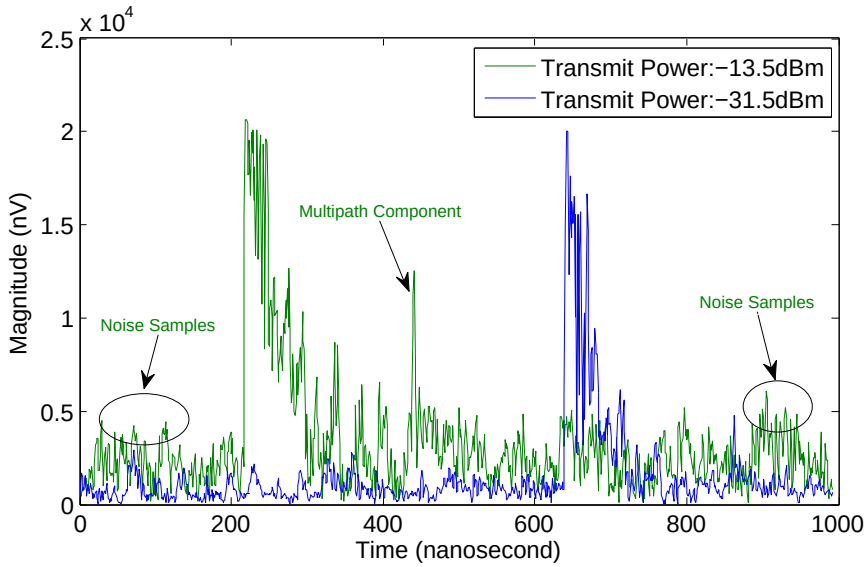

Figure 4.3: Received IEEE 802.15.4-2011 UWB channel impulse responses when using transmit powers of -13.5dBm and -31.5dBm, at a distance of 2.5m.

different transmit powers are emitted. At the antenna, the UWB pulse with transmit power of -13.5dBm is measured as shown in Figure 4.2 (a). The other UWB pulse with transmit power of -31.5dBm is measured as shown in Figure 4.2 (b). It is clear that there is no noise in these UWB pulses, if have, some thermal noise.

At the receiver, both UWB pulses are sampled as shown in Figure 4.3. The channel impulse response exhibits multipath components with different amplitudes and delays. Nevertheless, the magnitude of noise samples and multipath components obtained using the transmit power of -13.5dBm is higher than the use of the transmit power of -31.5dBm at a distance of 2.5m. Therefore, the use of higher transmit power may generate more noise, especially in a short transmission range.

In [17], the signal power at the receiver is modelled as an addition of the received signal energy part E_r and the noise energy part E_{noise} as:

$$E = E_r + E_{noise} = E_r + \sum_{i=1}^{N} E_i \tag{4.1}$$

Where, E_i is corresponding to the energy of the i^{th} noise source, E_r can be modeled by [46] as:

$$E_r = KPD^{-n} \tag{4.2}$$

Where, K is a constant that subsumes the effects of other physical layer parameters, P is a certain transmit power, D is the distance between two UWB radios, n is the path loss exponent. The SNR is then defined by [17] as:

$$SNR = (\sum_{i=1}^{N} (SNR_i)^{-1})^{-1} = (\sum_{i=1}^{N} (\frac{E_r}{E_i})^{-1})^{-1} \tag{4.3}$$

Even though this SNR model theoretically considers all the noise sources, it does not provide exact noise source models relative to the channel parameters. Therefore, a SNR model of IEEE 802.15.4-2011 UWB propagation in practical implementations is required to showcase the features of the multipath channel.

4.2 Signal to Noise Ratio Calculation

In practice, it is difficult to distinguish noise sources as they are randomly distributed in the channel impulse response. The noise variance, σ_n, measured from the noise only

region of the channel impulse response, is regarded as the noise power:

$$\sigma_n = \frac{\sum_{i=k_{ns}-L_{noise}}^{k_{ns}+L_{noise}} (P_i^{real} - P_a^{real})^2 + (P_i^{imag} - P_a^{imag})^2}{L_{noise}}; if(i<0), i = i+K; \quad (4.4)$$

The index of the first arrival path is uniformly distributed in a length of L_{signal}, starting from the index k_{clp}, as shown in Figure 4.4, whereas the remaining slots $k_{clp}+L_{signal}+1,...,K$ contain only noise. These indices, from index k_{clp} to index $k_{clp}+L_{signal}$, are in the multipath plus noise region. The total energy of these indices is an addition of the signal power and the noise power.

Therefore the signal power is:

$$P_{signal} = \sum_{j=k_{clp}}^{k_{clp}+L_{signal}} (P_j^{real} - P_a^{real})^2 + (P_j^{imag} - P_a^{imag})^2 - \sigma_n \times L_{signal}; if(j>=K), j = 1; \quad (4.5)$$

Where, P_j^{real} and P_j^{imag} are the real value and imaginary value of the j^{th} multipath sample, due to the complex-valued time-discrete input. The SNR is defined as the difference between the P_{signal} and the noise variance σ_n:

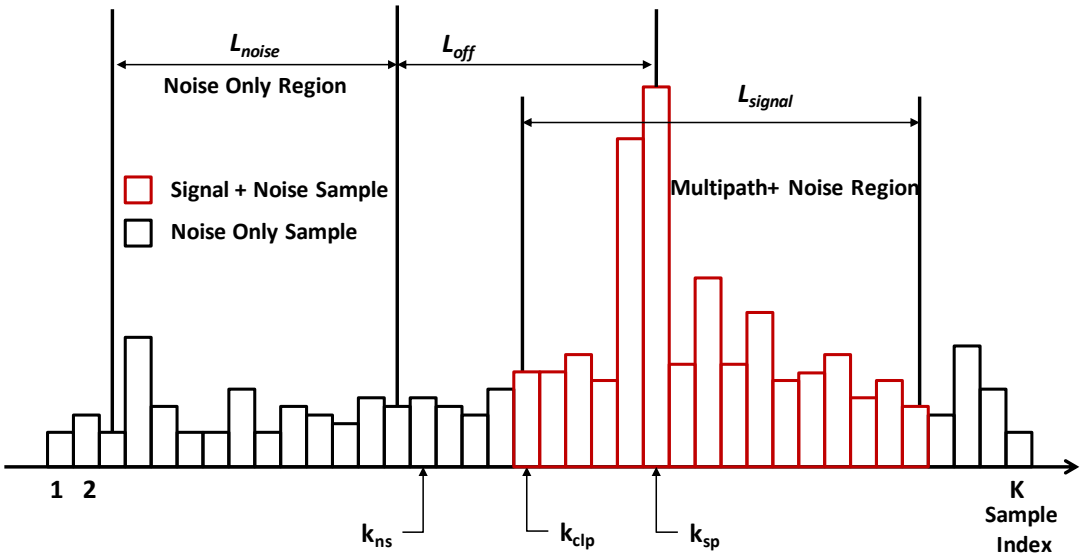

Figure 4.4: Signal to noise ratio calculation.

$$SNR = 10log(\frac{P_{signal}}{\sigma_n}) \tag{4.6}$$

This SNR describes the signal quality to a certain extent. However, various noise sources in UWB communication system have effects on the SNR of the received signal, such as system characteristics, unknown and time-varying multipath components. Consequently, the features of the IEEE 802.15.4-2011 UWB propagation in multipath environments are needed to observe the relationship between the transmit power, the transmission range and the SNR.

4.3 Multipath Propagation Observation

In this section, extensive ranging experiments are described which were performed in an anechoic chamber and indoor environments. The purpose is to observe the features of IEEE 802.15.4-2011 multipath propagation and extract the relationship between the transmit power, the transmission range and the SNR.

4.3.1 Experimental Activity

Two *Decawave* IEEE 802.15.4-2011 standard compliant UWB transceivers [11] were employed to measure and record the transmit power, the noise variance, the received signal power and the SNR. The UWB signal parameters are listed in Table 3.1. The ranging parameters are listed as in Table 3.2. A number of transmit powers were used ranging from -31.5dBm to -13.5dBm.

The maximum is limited by FCC to -13.5dBm. The minimum transmit power of the device is -31.5dBm. A ranging experiment is using one transmit power and one transmission range. Different propagation conditions were considered, such as LOS in the

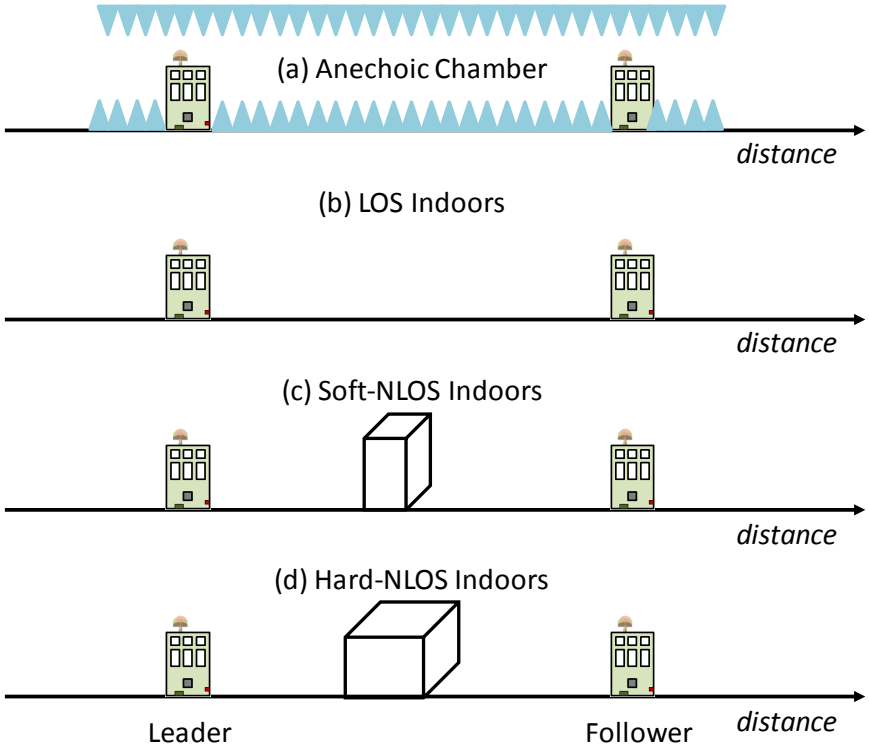

Figure 4.5: Arrangement of the ranging experiments: (a) anechoic chamber; (b) LOS indoors; (c) Soft-NLOS indoors; (d) Hard-NLOS Indoors.

anechoic chamber, LOS, soft-NLOS, hard-NLOS in indoor environment. The arrangement of the ranging experiments is depicted in Figure 4.5.

The measurement scenarios are shown in Figure 4.6, which can be categorized into three parts. The first part is to observe the effect of different transmit powers on the channel impulse response (CIR), SNR and ranging performance without or with multipath propagation. Ranging experiments were implemented in an anechoic chamber (AC) and in an indoor office (OFC) in LOS condition with a fixed distance of 0.7m, as shown in Figure 4.6 (a), (b). The transmit power varies from -31.5dBm to -13.5dBm. Each experiment collects 200 instant ranging measurements and 200 CIRs.

The second part is to observe the effect of transmit power and transmission range on the SNR and ranging performance in multipath propagation. Ranging experiments were implemented in a corridor in LOS condition at different distances, as shown in Figure 4.6 (c). During experiments, the follower is kept stationary; the leader moves to the 12 testing points ranging from 2.5m to 30m with each interval of 2.5m. The

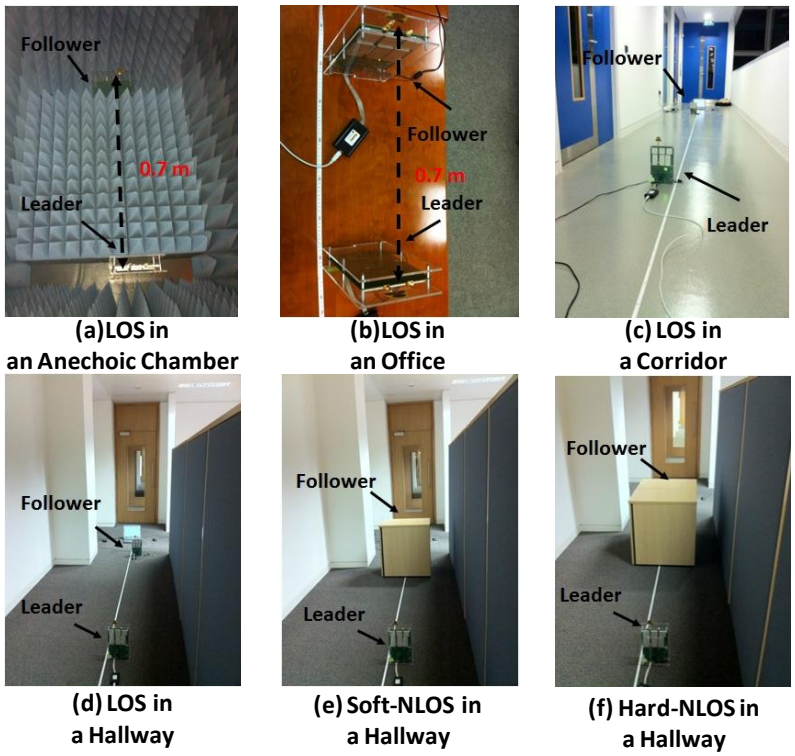

Figure 4.6: Ranging experimental setups in LOS and NLOS conditions.

transmit power varies from -31.5dBm to -13.5dBm with each interval of 1.5dBm. Each experiment collects 200 instant ranging measurements and 200 CIRs.

The third part is to observe the effect of transmit power and transmission range on the SNR and ranging performance in different propagation conditions. Ranging experiments were implemented in a hallway in LOS, soft-NLOS, hard-NLOS conditions at different distances ranging from 2.5m to 10m with each interval of 2.5m, as shown in Figure 4.6 (d), (e), (f). The transmit power varies from -31.5dBm to -13.5dBm with each interval of 1.5dBm. Each experiment collects 100 instant ranging measurements and 100 CIRs. All the obstacles around the ranging system and the follower are stationary; only the leader moves to the testing points. A locker ($L \times W \times H$: $40cm \times 50cm \times 70cm$) is used to create a soft-NLOS propagation condition. In order to observe different NLOS propagation, two lockers ($L \times W \times H$: $80cm \times 50cm \times 70cm$) are used to form the hard-NLOS condition. The lockers were placed in the middle of the leader and the follower.

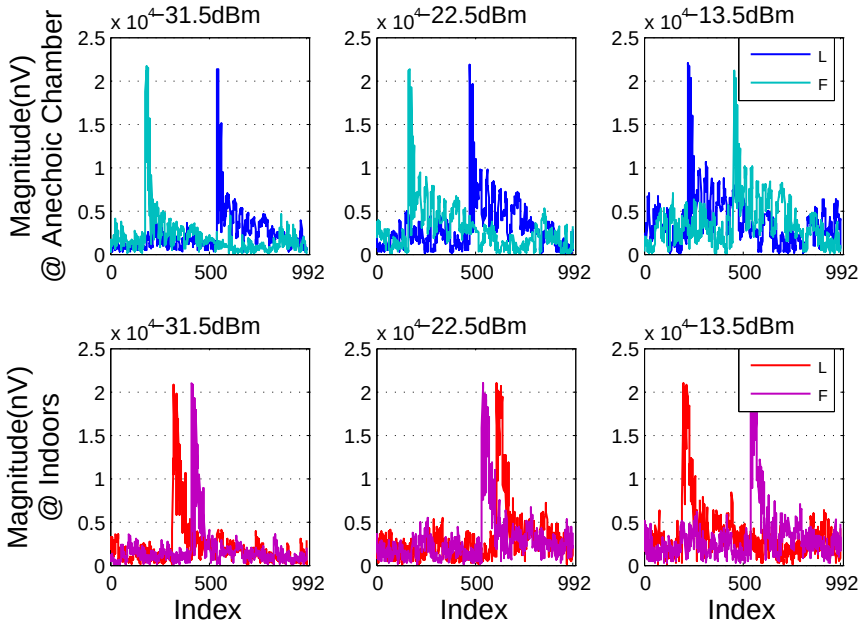

Figure 4.7: Measured channel impulse responses in anechoic chamber and indoor office. L: leader; F: follower.

4.3.2 Features

4.3.2.1 Propagation in Anechoic Chamber and Indoor Environment

The first part measurements were collected from the ranging experiments in anechoic chamber (AC) and office (OFC) as shown in Figure 4.6 (a), (b). Figure 4.7 shows the waveforms of the channel impulse responses (CIRs) captured at the leader (L) and the follower (F) using different transmit powers: -31.5dBm, -22.5dBm and -13.5dBm. In AC, the magnitude of noise samples becomes higher with transmit power increasing. This situation also occurs in the OFC.

Moreover, the waveforms of the CIRs are not the same. This is because of the parameters of multipath channels, such as reflection coefficients, are varying during the signal propagation.

Ideally, only one peak path exists in the CIRs. However, in practical implementation, some multipath components exhibit due to reflections. In OFC, some adjacent peaks can be found in the CIRs, especially using high transmit power, such as -22.5dBm and

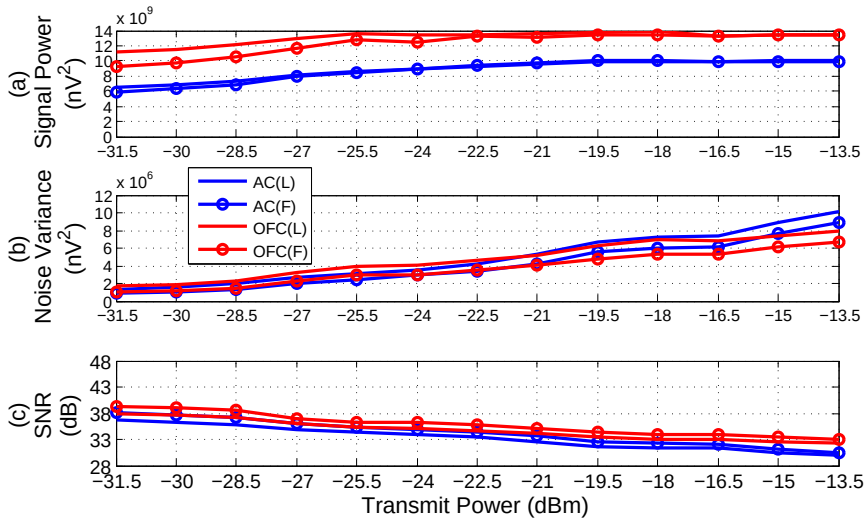

Figure 4.8: Comparison of AC and OFC channel measurements. L: leader; F: follower.

-13.5dBm. However, in AC, the number of peak paths are almost the same when using different transmit powers.

Figure 4.8 shows the relationship between received signal power, noise variance, SNR and transmit power in AC and OFC. With the transmit power increasing, the received signal power increases, as shown in Figure 4.8 (a). The received signal power in OFC is higher than AC's. This is due to a number of multipath components (such as the adjacent peaks) arrive at the signal duration in multipath propagation. The noise variance measured in AC and OFC are approximately similar, as shown in Figure 4.8 (b). However, the noise variance increases with the transmit power increasing.

In AC, there is no multipath effect. If the thermal noise and quantisation noise are constant, therefore this phenomenon is mainly due to the saturation effect. In OFC, this situation is due to the saturation effect and multpath effect. The SNR decreases with the transmit power increasing in short range of 0.7m as shown in Figure 4.8 (c). This is because the ADC goes into saturation and the saturation noise increases quickly. At the same time, the strong received signal is clipped by the ADC and its power tends to a stable value.

The ranging performance is shown in Figure 4.9. The actual distance is 0.7m. In

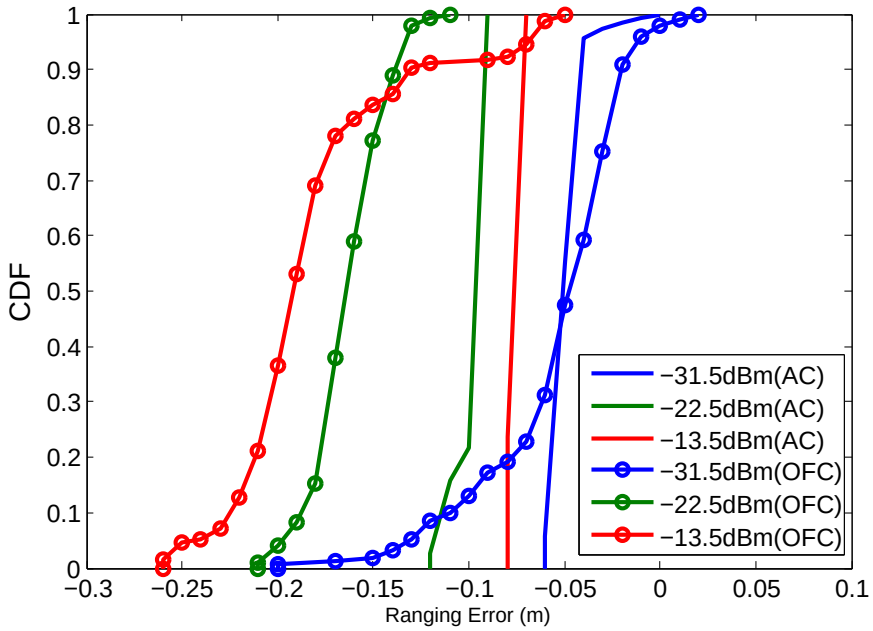

Figure 4.9: CDF of ranging error in AC and OFC. L: leader; F: follower.

AC, the ranging error below 10cm occurs in 100% of the measurements, when using transmit power of -31.5dBm. In OFC, the ranging error below 10cm occurs in 90% of the measurements, when using transmit power of -31.5dBm. In AC, the ranging error below 10cm occurs 80% and 100% of the measurements, when using transmit power of -22.5dBm and -13.5dBm, respectively. In OFC, the ranging error below 10cm occurs 0% and 8% of the measurements, when using transmit power of -22.5dBm and -13.5dBm, respectively. As a result, in short range of 0.7m, the system measurements show that the lower transmit power (down to -31.5dBm), the higher SNR and the more accurate range estimates. The use of low transmit power in a short transmission range may obtain high SNR in practical implementations.

4.3.2.2 Multipath Propagation in LOS Condition

The second part measurements were collected from the ranging experiments in a corridor in LOS conditions as shown in Figure 4.6 (c). In practice, transmission range is another important parameter that affects the received signal power and the SNR.

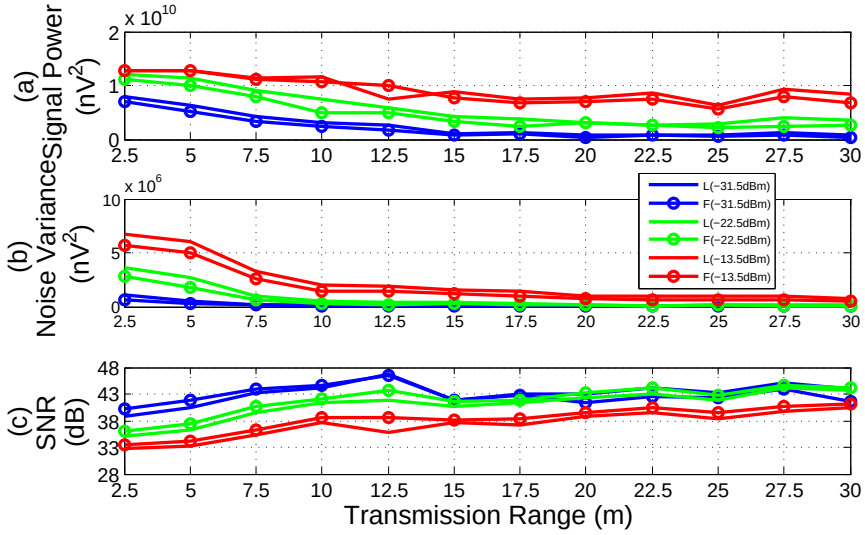

Figure 4.10: Channel measurements in a corridor. L: leader; F: follower.

Figure 4.10 shows the relationship between the transmit power, the transmission range and the SNR. The received signal power and the noise variance decrease with distance increasing, see Figure 4.10 (a) and (b). The SNR increases with the distance increasing, see Figure 4.10 (c). From 2.5m to 30m, the lower transmit power (e.g., -22.5dBm) achieves larger SNRs than the use of the higher transmit power (e.g., -13.5dBm). However, when using the lowest transmit power of -31.5dBm, the measured SNR increases firstly to reach a maximal value and then decreases with distance increasing. This is because at a short range (approximately up to 12.5m), the saturation and multipath effects contribute more noise to the system, see 4.10 (b).

In a longer transmission range (approximately after 12.5m), the received signal power decreases resulting in SNR degradation due to thermal and quantization noise and multipath effect, see Figure 4.10 (b).

Figure 4.11 shows the ranging performance. The ranging error below 10cm occurs 35%, 60%, 40% of the measurements, when using the transmit powers of -31.5dBm, -22.5dBm, -13.5dBm, respectively. The use of the medium transmit power of -22.5dBm achieves the best ranging performance. The use of the largest transmit power of -13.5dBm achieves lower ranging performance and SNR than the use of the medium

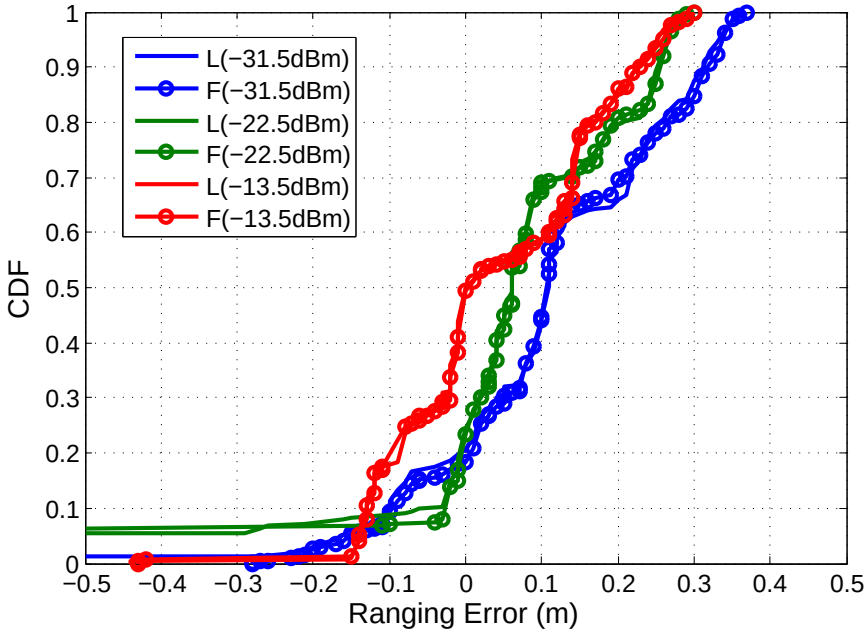

Figure 4.11: CDF of the ranging error in a corridor for the LOS condition. L: leader; F: follower.

transmit power 4.10 (c), but keeps the strongest received signal power, see Figure 4.10 (a). The system obtains the worst ranging performance by using the lowest transmit power of -31.5dBm with distance increasing from 2.5m to 30m. As a result, using a specific transmit power, the relationship between transmission range and SNR is nonlinear. In a short range, the SNR increases with distance increasing mainly due to the saturation and multipath effects. In a long range, the SNR decreases with distance increasing mainly due to the thermal and quantisation noise and multipath effect.

4.3.2.3 Multipath Propagation in Different Conditions

The third set of measurements were collected from the ranging experiments in a hallway in LOS and NLOS conditions as shown in Figure 4.6 (d), (e), (f).

The Figure 4.12 and Figure 4.13 show the waveforms of CIRs captured at a fixed distance of 10m, by using the transmit power of -13.5dBm. In LOS condition, the magnitude of noise region is higher than soft-NLOS and hard-NLOS conditions. The hard-NLOS propagation obtains the lowest noise magnitude. The magnitude of multi-

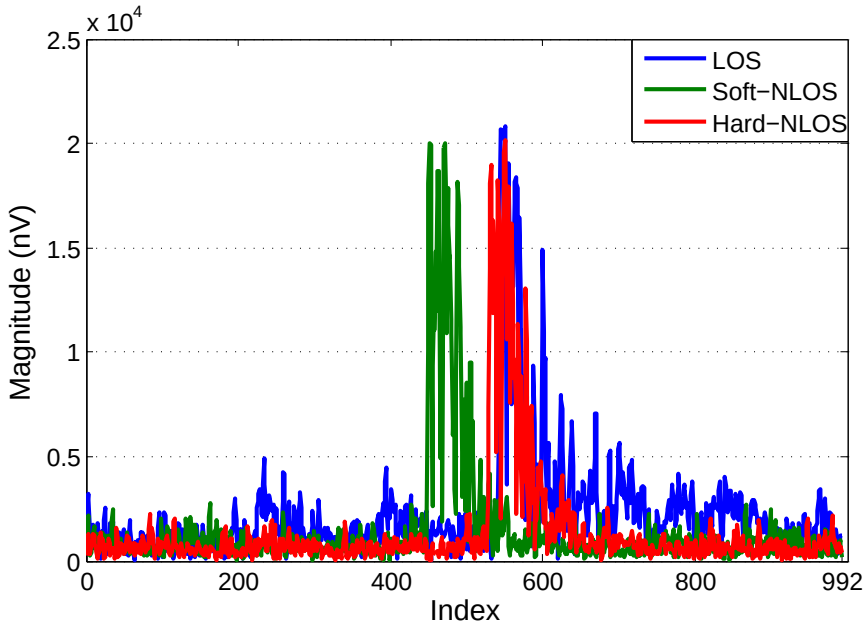

Figure 4.12: Leader channel impulse responses in a Hallway for the LOS and NLOS conditions.

path signal region in LOS condition is higher than the soft-NLOS's and hard-NLOS's.

Figure 4.14 to Figure 4.16 show the relationship between transmit power, transmission range and SNR in LOS and NLOS conditions. Figure 4.14 shows the results of LOS ranging. The received signal power decreases with distance increasing in all conditions, see Figure 4.14 (a), Figure 4.15 (a) and Figure 4.16 (a). Due to the different pass loss exponents, the received signal power in LOS is higher than soft-NLOS and hard-NLOS conditions when using the same transmit power and transmission range.

The noise power decreases with distance increasing when using higher transmit power (e.g., -13.5dBm) in all conditions, see Figure 4.14 (b), Figure 4.15 (b) and Figure 4.16 (b). However, the noise in soft-NLOS propagation tends to a constant after 5m when using transmit power of -31.5dBm, see Figure 4.15 (b). The noise in hard-NLOS propagation is already a constant at the beginning when using transmit power of -31.5dBm, see Figure 4.16 (b).

The SNR increases with distance increasing when using largest transmit power (e.g., -13.5dBm) in all conditions, and the SNRs in hard-NLOS and soft-NLOS are higher

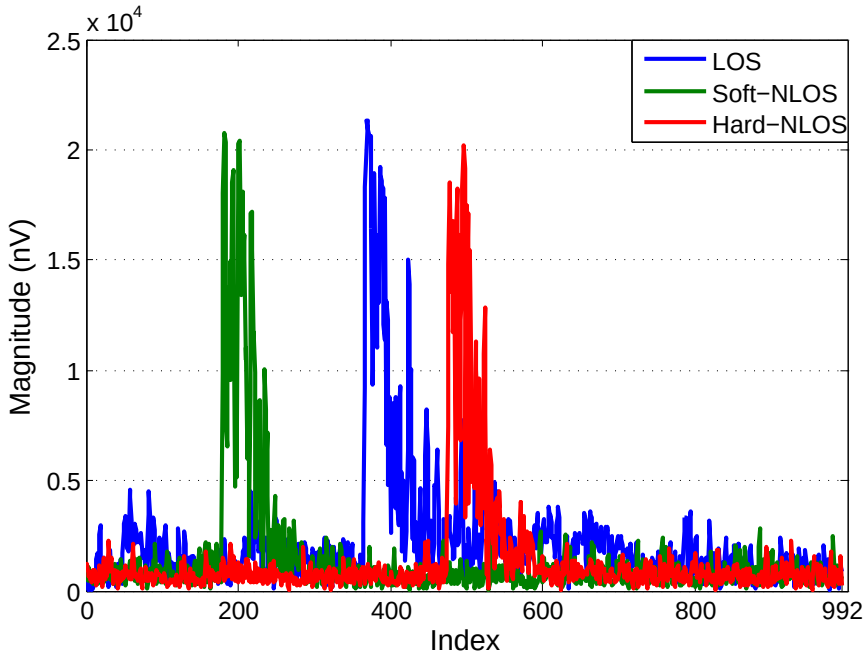

Figure 4.13: Follower channel impulse responses in a Hallway for the LOS and NLOS conditions.

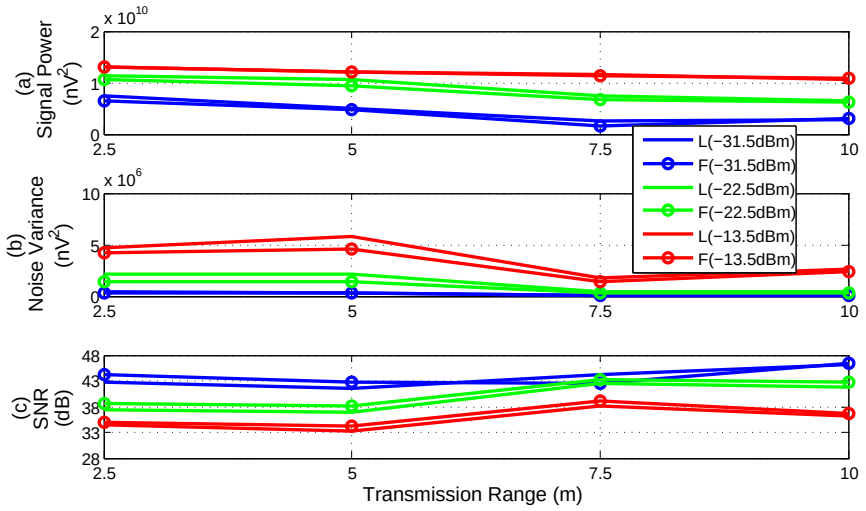

Figure 4.14: Channel measurements in a hallway for the LOS condition. L: leader; F: follower.

than the LOS's, see Figure 4.14 (c), Figure 4.15 (c) and Figure 4.16 (c).

However, when using the transmit power of -31.5dBm, the SNR in soft-NLOS propagation decreases, see Figure 4.15 (c). Similar to soft-NLOS, the SNR in hard-NLOS decreases when using the transmit power of -31.5dBm, see Figure 4.16 (c), and at 10m, there is no signal at the antenna, and the SNR is zero.

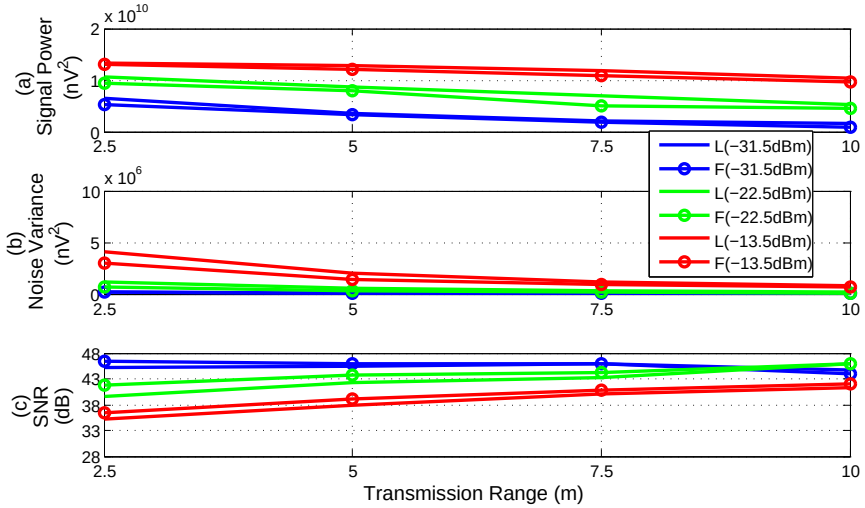

Figure 4.15: Channel measurements in a hallway for the soft-NLOS condition. L: leader; F: follower.

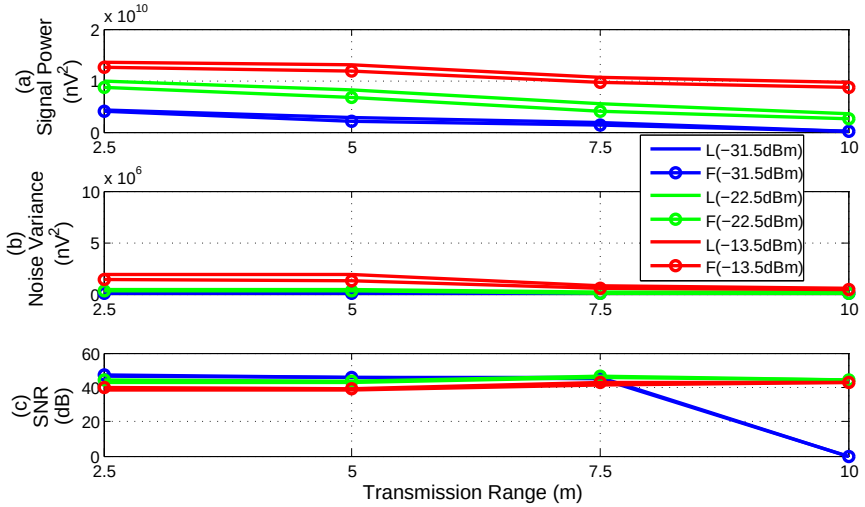

Figure 4.16: Channel measurements in a hallway for the hard-NLOS condition. L: leader; F: follower.

Figure 4.17 to Figure 4.19 show the ranging performance in LOS, soft-NLOS and hard-NLOS propagation conditions. The summary of ranging performance is listed in Table 4.1.

In LOS condition, the ranging error below 10cm occurs in 55%, 55%, 50% of the measurements, when using transmit powers of -31.5dBm, -22.5dBm, -13.5dBm, respectively. In a short range in LOS condition, using lower transmit power can get more accurate range estimates. Nevertheless, the use of largest transmit power achieves the worst ranging performance. In soft-NLOS and hard-NLOS conditions, the ranging ac-

Table 4.1: Summary of ranging performance in different propagation conditions

	LOS	Soft-NLOS	Hard-NLOS
Accuracy $> 10cm$	2.5∼10m	2.5∼10m	2.5∼10m
Tx:-31.5dBm	55%	12%	1%
Tx:-22.5dBm	55%	40%	2%
Tx:-13.5dBm	50%	30%	5%

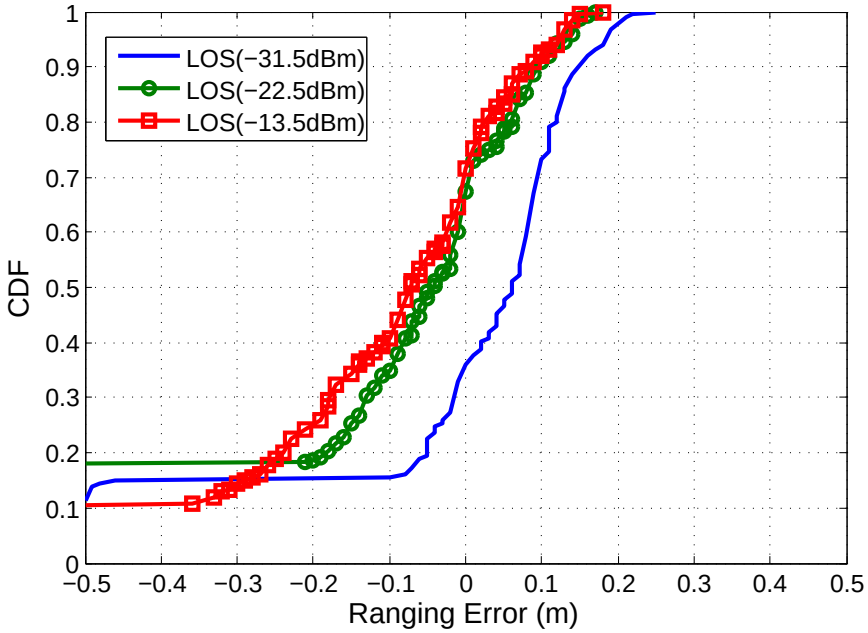

Figure 4.17: CDF of the ranging error in a hallway for the LOS condition.

curacy decreases seriously, see Table 4.1. The ranging error in NLOS conditions is mainly due to the extra propagation delay which is caused by the slower propagation speed of UWB waves in some obstacles or the selecting the reflected signal as the direct path for TOA estimation [16].

As a result, the strong signal may generate saturation noise and multipath effect and lower the system performance in a short range. The longer transmission range and the larger power loss exponent situations can attenuate the signal power. However, these situations shorten the connectivity and the SNR decreases as well due to thermal and quantisation noise. In NLOS conditions, the ranging accuracy degradation is mainly due to extra propagation delay.

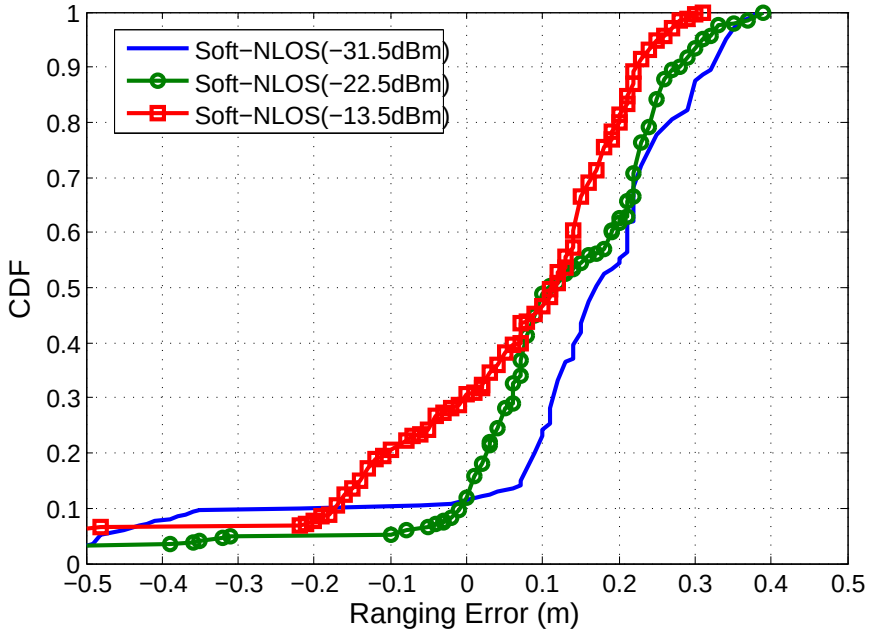

Figure 4.18: CDF of the ranging error in a hallway for the soft-NLOS condition.

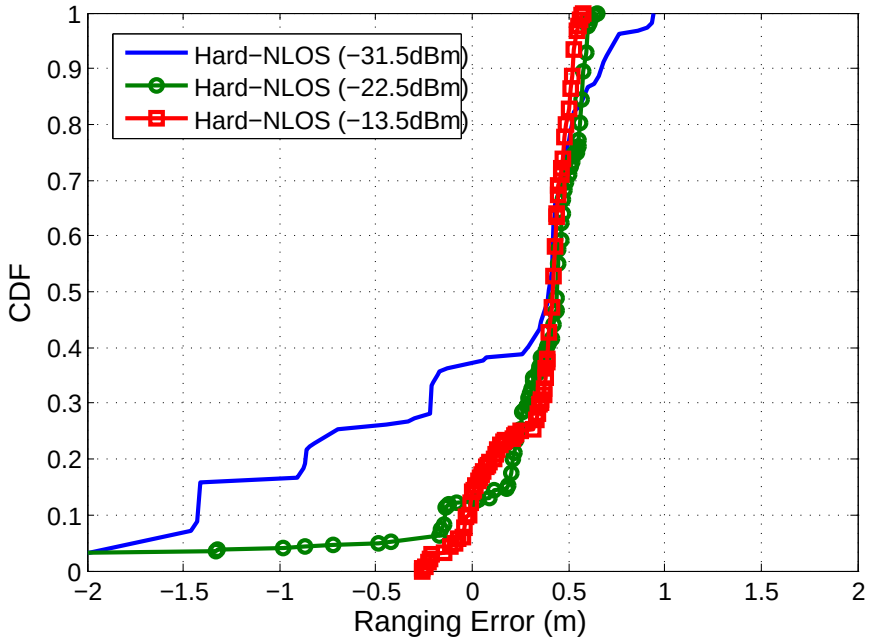

Figure 4.19: CDF of the ranging error in a hallway for the hard-NLOS condition.

4.3.2.4 Summary

From these results, major features of IEEE 802.15.4-2011 UWB multipath channel observation are as follows.

• In multipath propagation, if the UWB system is not well designed, the relationship

between the transmission range and the SNR is nonlinear, when using the highest transmit power. The SNR increases firstly to reach a maximal value and then decreases with distance increasing. The maximal SNR is an inflexion point. Before this inflexion point, the shorter transmission range makes the ADC go into saturation and results in lower SNR. After this inflexion point, the SNR decreases with distance increasing, due to the thermal and quantisation noise.

• In LOS conditions, the relationship between the transmit power, the SNR and the ranging performance is that: (1) in a short range or before the inflexion point, the lower the transmit power, the higher the SNR and more accurate ranging performance; (2) in a long range or after the inflexion point, the larger the transmit power, the higher the SNR and more accurate ranging performance.

• In NLOS conditions, the relationship between the transmit power and the SNR is the same as the one in LOS condition. However, the ranging performance is mainly affected by that the propagation of electromagnetic waves is slower in some materials compared to air. The signal arrives with excess delay, or the receiver can only observe the reflected signal.

4.4 Bilateral Transmit Power Control

As described previously, the channel parameters such as the transmit power, the transmission range would affect the SNR resulting in IEEE 802.15.4-2011 UWB TOA ranging instability and inaccuracy. Only the transmit power can be controlled as other parameters are unknown and time-varying. Based on the relationship between the transmit power, the transmission range and the SNR described above, this section presents a bilateral transmit power control to stabilize the multipath channel, and improve the ranging performance in LOS conditions.

4.4.1 Power Control Considerations

Relevant aspects of the power control in the IEEE 802.15.4-2011 UWB ranging system should be considered as follows.

• Ranging protocol. This is the basic framework for the UWB ranging system. The power control algorithm should be integrated into the ranging protocol.

• Power constraints. The transmit power is limited within the FCC limits.

• Capacity and signal payload. The signal should accommodate all data with associated quality requirements. The maximum payload of the IEEE 802.15.4-2011 signal is 127 bytes.

• Tradeoff management. The Bit Error Rate (BER) can be used to manage the tradeoff between connectivity (received signal power) and SNR [17]

$$BER = \frac{1}{2} erfc(\sqrt{\frac{1}{2} SNR}) \tag{4.7}$$

Where, the $erfc$ is the error function.

4.4.2 Power Control Algorithms

Employing the symmetric double sided two way TOA (SDS-TW-TOA) ranging protocol, a TOF is calculated through double sided wireless communications between the leader and the follower. Hence, both UWB nodes need to implement the power control algorithms. The target SNR γ^T is selected using the BER function, and a specific minimum receive power Pr_{min} and the noise floor of the device P_{nf} are set to meet the target SNR, $\gamma^T = 10log(Pr_{min}/P_{nf})$. If the received signal power is less than the Pr_{min}, the instant SNR will be less than the target SNR. Hence, the Pr_{min} is an inflexion point in the power control implementation.

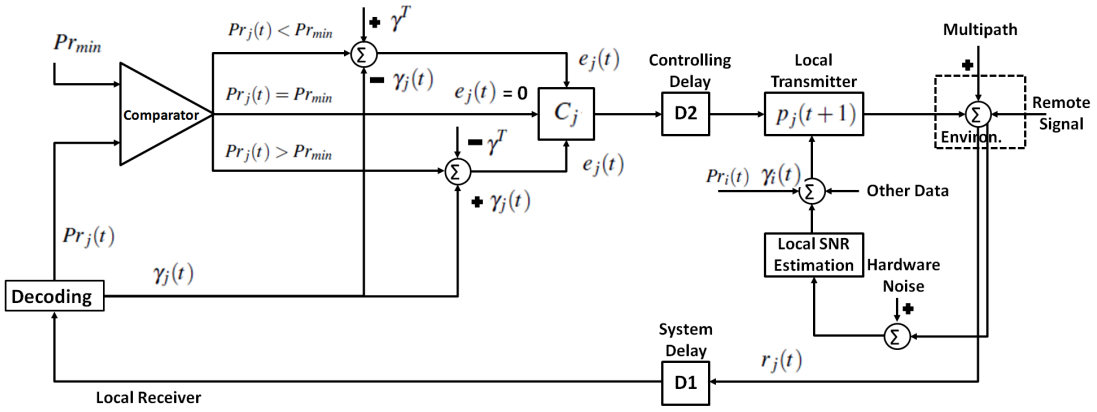

Figure 4.20: Block diagram of bilateral transmit power control loop at one UWB node.

Consider the power control scheme at one local UWB node in Figure 4.20, if the received signal power $Pr_j(t)$ decoded from the j^{th} remote signal $r_j(t)$ is greater than the Pr_{min}, the transmit power is increased or decreased depending whether the SNR ($\gamma_j(t)$) decoded from the j^{th} remote signal $r_j(t)$ is above or below the target SNR (γ^T). If the received signal power $Pr_j(t)$ is smaller than the Pr_{min}, the transmit power is decreased or increased depending whether the $\gamma_j(t)$ is above or below the γ^T. If the $Pr_j(t)$ is equal to the Pr_{min}, the transmit power does not change.

4.4.2.1 Quick Power Control

The first transmit power update algorithm in this work is denoted as adaptive power control or quick power control (QPC); and it is implemented as equations (4.8) to (4.10):

$$e_j(t) = \begin{cases} \gamma^T - \gamma_j(t) & Pr_j(t) < Pr_{min} \\ \gamma_j(t) - \gamma^T & Pr_j(t) > Pr_{min} \\ 0 & Pr_j(t) = Pr_{min} \end{cases} \tag{4.8}$$

$$p_j(t+1) = p_j(t) + \Delta e_j(t) \tag{4.9}$$

$$p_j(t+1) = min\{P_{max}, p_j(t) + \Delta e_j(t)\} \| max\{P_{min}, p_j(t) + \Delta e_j(t)\} \tag{4.10}$$

Where, the $e_j(t)$ is the power update command, and Δ is the minimum interval of the hardware power settings. P_{max} is maximum transmit power of the FCC limits and P_{min} is the minimum transmit power of the device limits. The P_{max} and P_{min} are controlled to ensure the inherent hardware saturation limitations are not exceeded. $p_j(t+1)$ is an integrating controller with $C_j\{\Delta e_j(t)\} = \Delta e_j(t)$ in one-slot cycle. At the same time, the SNR $\gamma_i(t)$ and received signal power $Pr_i(t)$ measured at local node are sent back to the remote UWB node for remote power control loop implementation.

4.4.2.2 Slow Power Control

An alternative power control algorithm is a different command decoding than above and is denoted as alternative power control or slow power control (SPC). It makes it possible to emulate slower update rates, or to turn off power control by transmitting a series of $e_j(t)$. In a n-slot cycle ($k = 1...n$), the power update command $e_j(t)$ in equation (4.8) is computed according to:

$$e_j(t) = \frac{\sum_{k=1}^{n} e_k(t)}{n} \tag{4.11}$$

Where,

$$e_k(t) = \begin{cases} \gamma^T - \gamma_k(t) & Pr_j(t) < Pr_{min} \\ \gamma_k(t) - \gamma^T & Pr_j(t) > Pr_{min} \\ 0 & Pr_j(t) = Pr_{min} \end{cases} \tag{4.12}$$

4.4.2.3 Fixed Step Size Power Control

Another approach is decision feedback where the sign of the error alone is fed back resulting in:

$$s_j(t) = sign(e_j(t)) = \begin{cases} sign(\gamma^T - \gamma_j(t)) & Pr_j(t) < Pr_{min} \\ sign(\gamma_j(t) - \gamma^T) & Pr_j(t) > Pr_{min} \\ 0 & Pr_j(t) = Pr_{min} \end{cases} \tag{4.13}$$

When utilizing decision based feedback, a simple integrating controller takes the form:

$$p_j(t+1) = p_j(t) + \beta s_j(t) \tag{4.14}$$

The controller is often referred to as a fixed step size power control (FPC) law where the power $p_j(t)$ is increased or decreased by β depending on the sign of error $s_j(t)$. Considering the $s_j(t)$ is greater or less than 0, the $s_j(t)$ can be set as $+1$ or -1, respectively. With the limitation of the inflexion point Pr_{min}, the updated transmit power can be expressed as:

$$p_j(t+1) = p_j(t) + \begin{cases} +\beta, s_j(t) < 0 & P_r < Pr_{min} \\ -\beta, s_j(t) > 0 & P_r < Pr_{min} \\ +\beta, s_j(t) > 0 & P_r > Pr_{min} \\ -\beta, s_j(t) < 0 & P_r > Pr_{min} \\ 0 & P_r = Pr_{min} \end{cases} \tag{4.15}$$

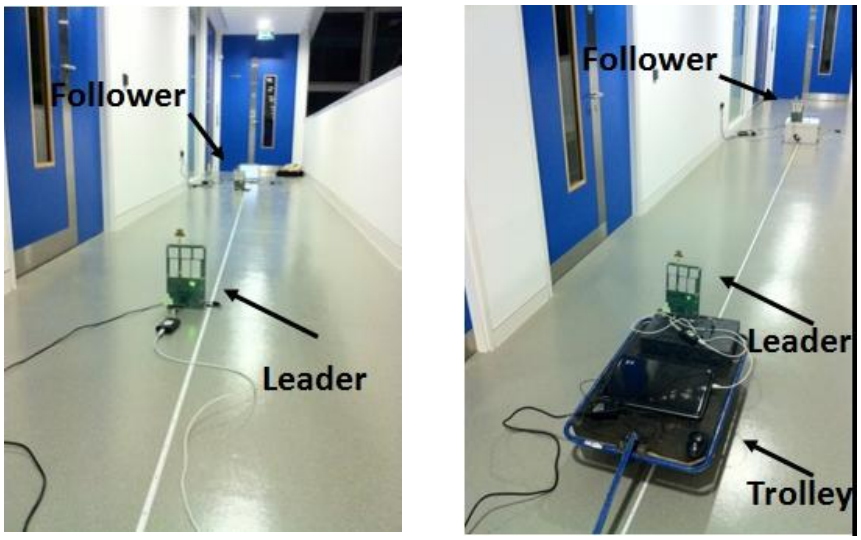

Figure 4.21: Setup of stationary and mobile ranging experiments.

4.4.2.4 None Power Control

The system without power control can be denoted as non-power control (NPC) system, in which the updating transmit power is always the same as:

$$p_j(t+1) = p_j(t) \tag{4.16}$$

The time delay ($D1$) of measuring and control signaling, see Figure 4.20, imposes a severe performance constraint on the power control loop performance of a power aware network based application.

4.4.3 Practical Implementation

The above power control algorithms are critically assessed using a multipath propagation scenario. Stationary (from 2.5m to 30m) and mobile (from 1m to 8m with a trolley) ranging experiments are set up inside an indoor environment, see Figure 4.21. A target SNR value of 43dB is selected for both UWB transceivers, guaranteeing a BER of $< 3e^{-11}$, verified using equation (4.7).

The noise floor value P_{nf} of the IEEE 802.15.4-2011 UWB prototype is measured which is $3.1e^5nV^2$ and the minimum receive power Pr_{min} is set to be $6.3e^8nV^2$ to meet the target SNR (43dB). The Δ is set to be 1.5dBm and the $e_j(t)$ is rounded to an integer. The β is set to be 1.5dBm. The maximum transmit power (-13.5dBm) of FCC limits is selected at the beginning for strongest links and also for the NPC system. A frame is a record of the receive time of the leading pulse according to the ranging algorithm. In this work, a ranging frame time is about 0.6s which is equal to 2 delays (300ms) plus 2 TOFs.

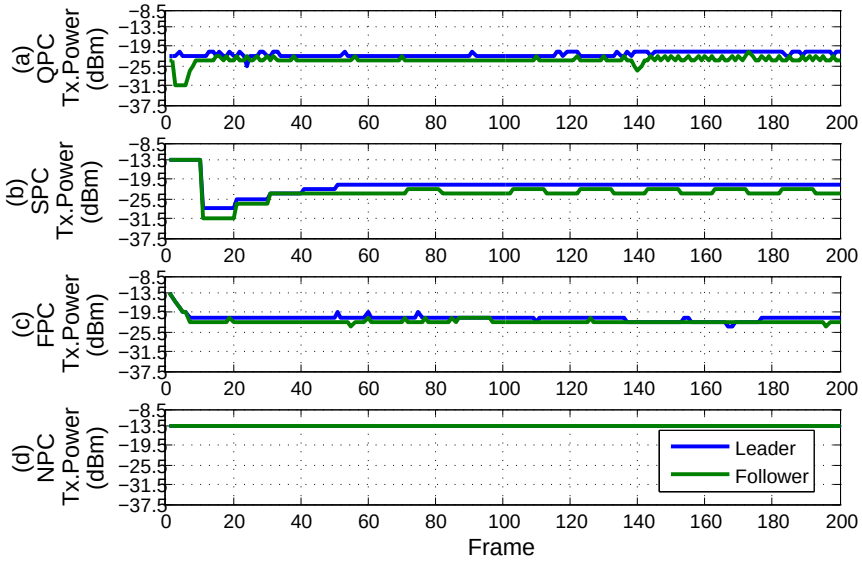

Figure 4.22: Transmit power updating at 17.5m. L: leader; F: follower.

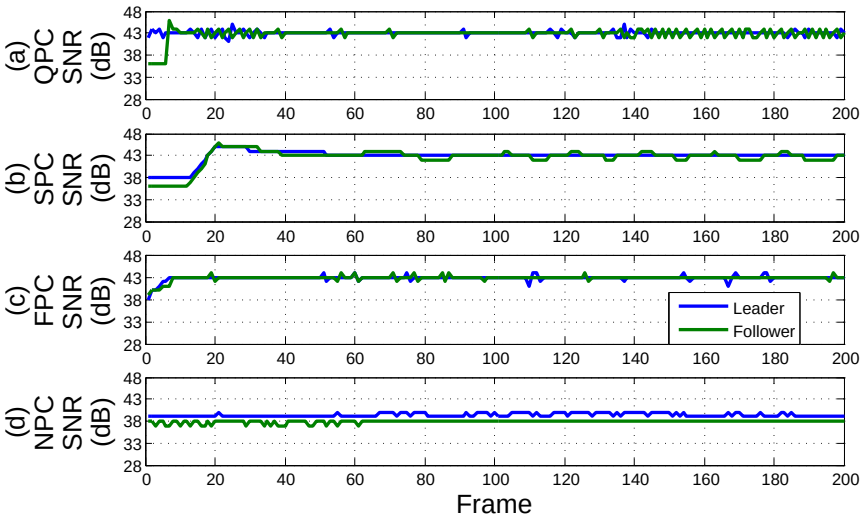

Figure 4.23: SNR updating at 17.5m. L: leader; F: follower.

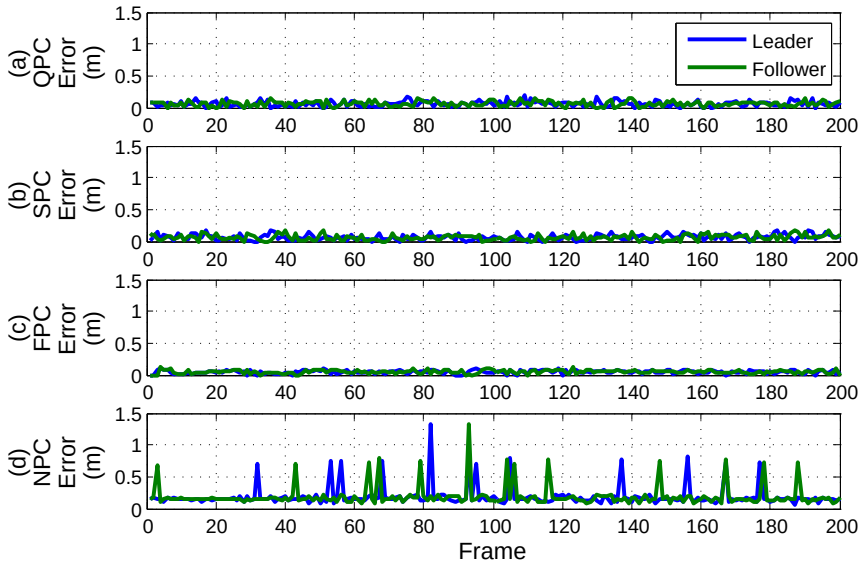

Figure 4.24: Instant ranging error at 17.5m. L: leader; F: follower

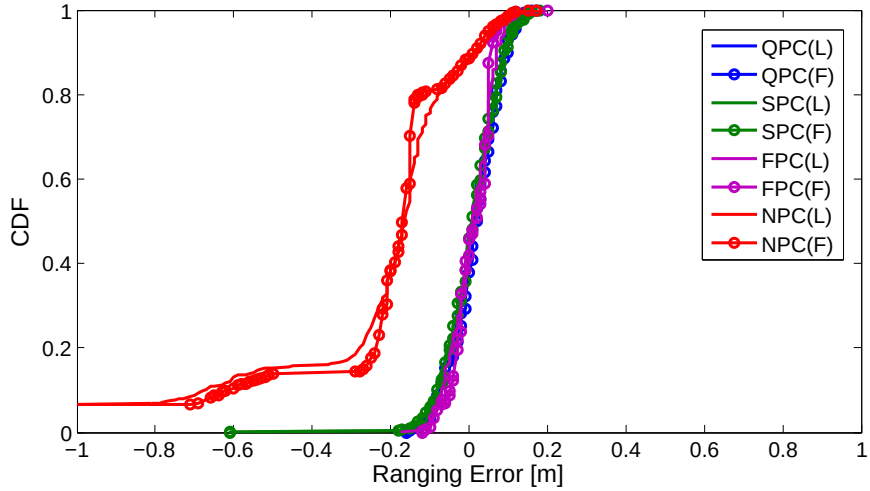

Figure 4.25: CDF of the ranging error for stationary power control tests. L: leader; F: follower

Hence, after receiving a signal, the system has about 300ms processing time for power control loop and other tasks implementation.

4.4.3.1 Stationary Power Control Test

For the purposes of clarity, the response of power control methods, QPC, SPC, FPC and NPC at distances 17.5m are presented graphically from Figure 4.22 to Figure 4.24.

The NPC uses maximum transmit power of -13.5dBm only, Figure 4.22 (d), and the

response shows that system can not reach the target SNR of 43dB at the a distance of 17.5m, see Figure 4.23 (d). The tested instant ranging accuracy is unstable and the biggest error observed is to be several meters, see Figure 4.24 (d). The QPC method, using equations (4.8) to (4.10), updates the signal outputs per frame, see the Figure4.22 (a), and the instant SNR measured reaches the target SNR quickly, see Figure 4.23 (a).

The SPC method, using equations (4.9) to (4.12), updates signal output every $n = 10$ frames. The leader maintains the target SNR after the frame-50 point and the transmit power updating turns off, see the Figure 4.22 (b) and Figure 4.23 (b). The FPC method, using equations (4.10), (4.13) to (4.15), updates with a fixed step size $\beta = 1.5dBm$. It updates the transmit power from the largest value of -13.5dBm and reaches the target SNR, see Figure4.22 (c) and Figure 4.23 (c). The transmit power updating speed is slower than the QPC but faster than the SPC. The power controlled system can stabilize the ranging channel and both UWB nodes achieve more accurate and staler ranging estimates than the NPC system, see Figure 4.24. Employing the bilateral transmit power control algorithms, the instant ranging estimates of the leader and follower are similar in behaviour.

Figure 4.25 shows the ranging precision of different power control algorithms. Table 4.2 shows the results comparison of different power control algorithms. Using the QPC method, ranging error below 10cm/5cm occurs in more than 91%/60% of the measurements, respectively. The worst case is 18cm. SPC method generates a ranging error that below 10cm/5cm occurs in more than 85%/50% of the measurements, respectively. However, the worst case is 60cm. FPC method obtains the most accurate range estimates, the error below 10cm/5cm occurs in more than 94%/80% of the measurements, respectively. The worst case is 20cm. Without power control, using the NPC method, ranging error below 10cm/5cm occurs in less than 20%/12% of the measurements, respectively. The worst case is greater than 1m.

To measure the transmit power efficiency for the respective algorithms, the transmit

Table 4.2: Stationary ranging results comparison of QPC, SPC,FPC, NPC

	QPC	SPC	FPC	NPC
Power Update Rate (cycle)	1	10	1	0
Power Update Value (dBm)	$1.5e_j(t)$	$1.5e_j(t)$	$+/-1.5$	Null
Measurements	4800	4800	4800	4800
Accuracy $> 10cm$	91%	85%	94%	<20%
Accuracy $> 5cm$	60%	50%	80%	<12%
Worst Case	18cm	60cm	20cm	1.4m

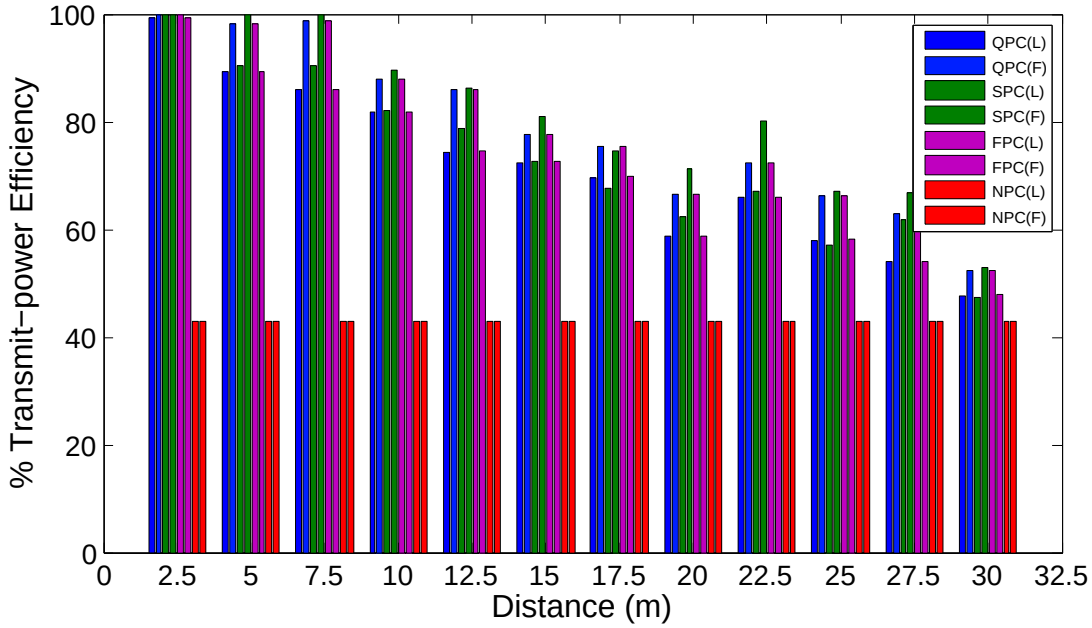

Figure 4.26: Transmit power efficiency from 2.5m to 30m. L: Leader; F: Follower

power efficiency for any one controller configuration is defined as the average transmit power consumed by two nodes operating using a particular power control algorithm for the duration of an experiment. For example 100% transmit power efficiency in this context would imply that the node is transmitting using its minimum output power setting. The transmit power efficiency here can be expressed as:

$$Efficiency = \frac{P_m - P_{ave}}{P_m - P_{min}} \times 100\% \tag{4.17}$$

Where, P_m is the maximum transmit power of the device setting, P_{ave} is the average transmit power consumed, P_{min} is the minimum transmit power of the device setting. In this system, P_m is 0dBm. P_{min} is -31.5dBm. Figure 4.26 plots the percentage trans-

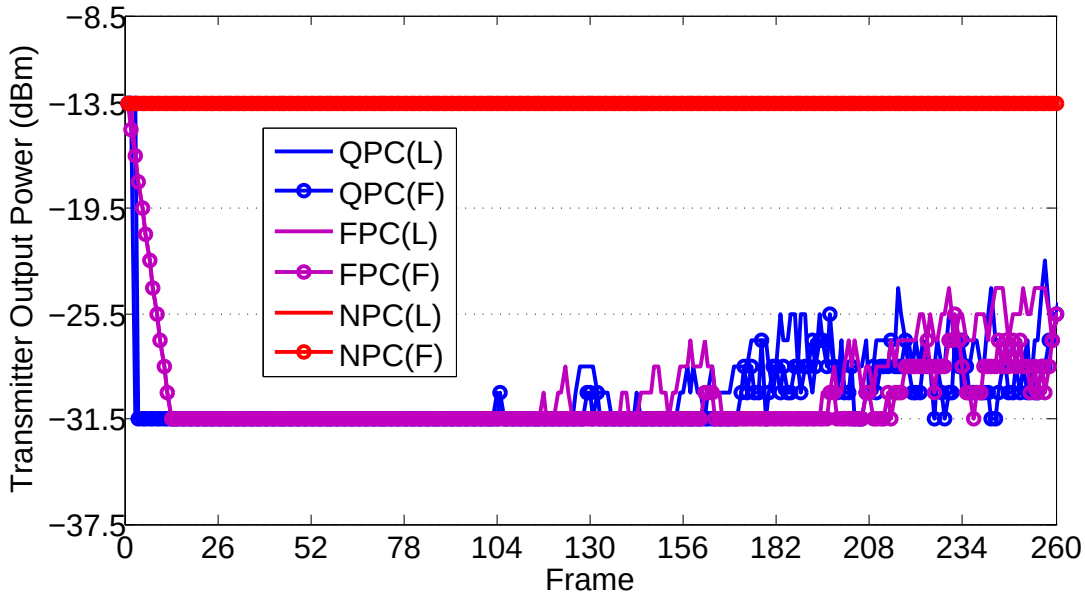

Figure 4.27: Transmit power updating in mobile condition. L: leader; F: follower

mit power efficiency for each of the mote control configuration. The utilization of power control methods can get more transmit power efficiency (up to 99%) than the NPC method (43%). With the distance increasing from 2.5m to 30m, the transmit power efficiency of the power control methods decreases from 99% to 50%, because the controller increases the output power to maintain target SNR and connectivity.

4.4.3.2 Mobile Power Control Test

The mobile ranging is tested to observe the performance of the power control methods in the real-world environment with uncertain factors such as the motion of the IEEE 802.15.4-2011 UWB nodes and a time-varying wireless multipath channel. The SPC method with a lower transmit power update rate, which is good for energy-saving of the system in stationary ranging case. Thus, this section considers the NPC, FPC and QPC for mobile test. The follower (F) is stationary during experiment. The leader (L) moves from 1m (from the follower) in a straight line to a distance of 8m with an approximate constant velocity of (35 frame/m), see the Figure 4.21. The distance estimates on the moving path are analyzed using a liner equation function in Matlab.

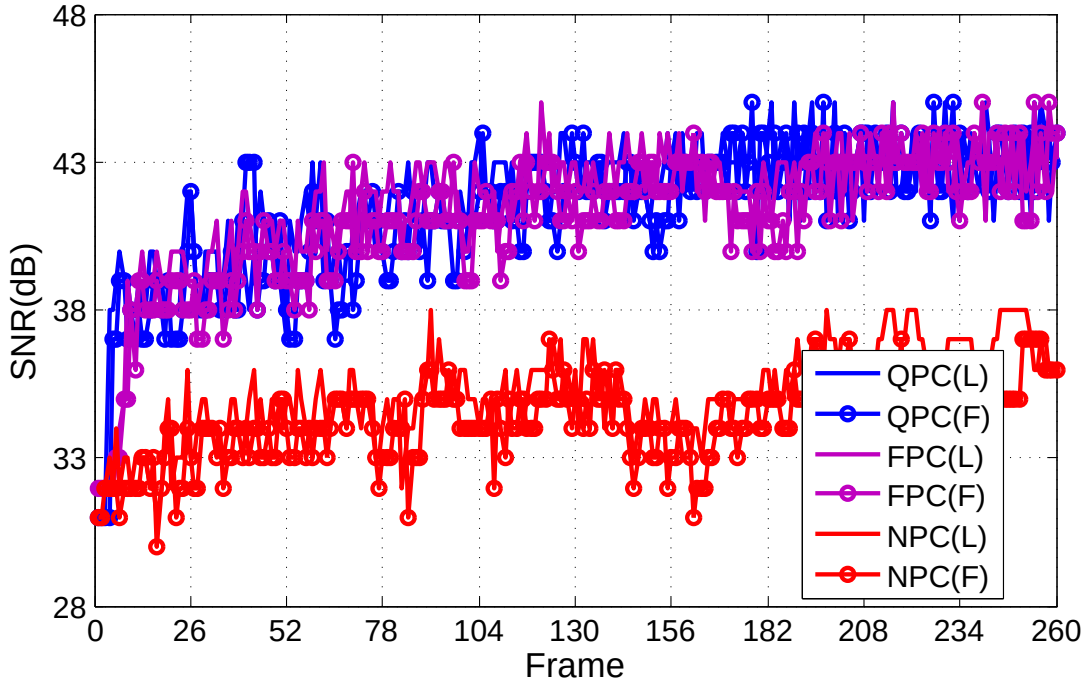

Figure 4.28: SNR updating in mobile condition. L: leader; F: follower

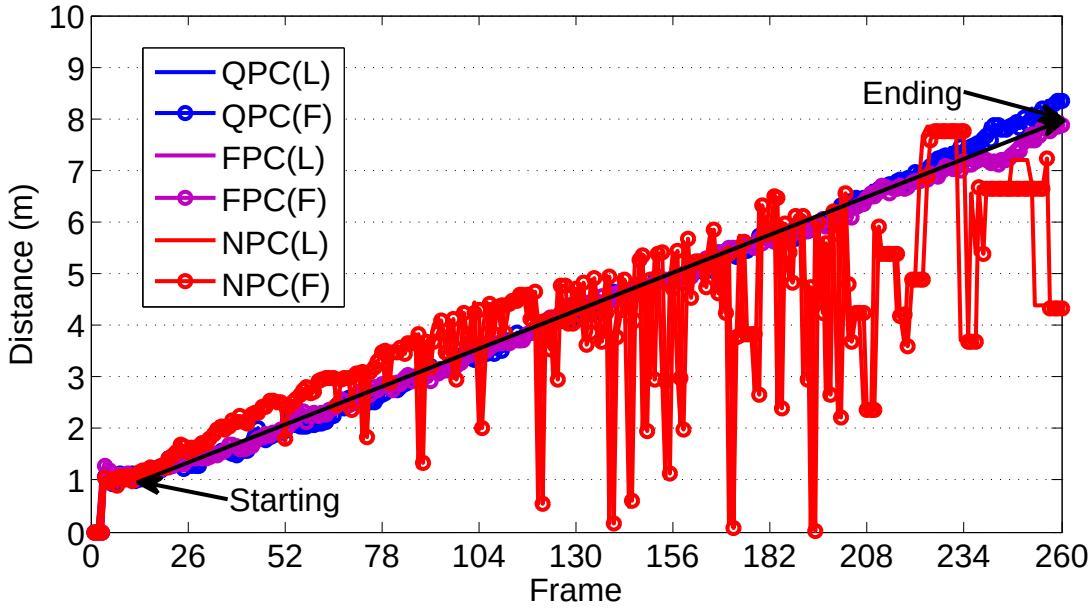

Figure 4.29: Distance measurements from 1m to 8m. L: leader; F: follower

Figure 4.27 shows the transmit power updating situations with the utilization of QPC, FPC and NPC. Both leader and follower run the power control loop and adjust the transmit power with related power control commands according to whether the SNR is greater or less than the target SNR (43dB). The NPC method keeps the maximum transmit-power (-13.5dBm).

The SNRs measured using NPC from 1m to 8m are always less than 43dB, see Figure 4.28. The QPC and FPC update the transmit power and reach the minimum transmit power of the device (-31.5dBm) before the 100^{th}-frame point, see Figure 4.27. It means that, at a short range, there exists many multipath effects and system needs low transmit power to mitigate them. Due to the inherent hardware saturation limitation, QPC and NPC can not get the expected SNR before the 100^{th}-frame point, see Figure 4.28. However, the SNRs increases with the distance increasing from the starting point. The transmit power using QPC and FPC, increases after the 100^{th}-frame point, see Figure 4.27. That means the system reaches the target SNR (43dB) and goes to maintain it, see the Figure 4.28. Even though the SNRs obtained by the NPC are always less than 43dB, the SNR increases with distance increasing from the starting point (32dB).

Figure 4.29 plots the ranging estimates when the leader moves from 1m (starting at about 13 frames point) to the end (8m test-point). The duration is about 247 frames. Hence, the velocity is approximately 35frames/m. The reference moving path can be represented as a linear equation $d_{ref} = 0.0283f + 1$. d is the instant tested distance, and f is the relative ranging frame.

The comparison of QPC,FPC,NPC in mobile ranging test is summarized in Table 4.3.

Table 4.3: Mobile ranging results comparison of QPC,FPC,NPC

	Frames	Linear Equation	MAE	Power Efficiency
Reference	247	d_{ref}=0.0283f+1	0	Null
QPC	247	d_{qpc}=0.029f+0.83	1.038m	95%
FPC	247	d_{fpc}=0.028f+0.96	0.0772m	97%
NPC	247	d_{npc}=0.019f+1.7	1.8532m	43%

Employing the QPC and FPC methods, the moving path linear equations are measured as $d_{qpc} = 0.029f + 0.83$ and $d_{fpc} = 0.028f + 0.96$, respectively. The d_{fpc} obtained by the FPC method is approximately equal to the equation of reference moving path. The tested moving path linear equation using NPC method is $d_{npc} = 0.019f + 1.7$. The

accuracy can be quantified by means of mean absolute error (MAE) as follows.

$$MAE = \frac{\sum_{f=1}^{247} |d_{ref} - d_x|}{247} \tag{4.18}$$

Where, d_x is the linear equation of one of the power control algorithms. Hence, the MAE of QPC is $\frac{\sum_1^{247} |0.007f+0.17|}{247} = 1.038m$. The MAE of FPC is $\frac{\sum_1^{247} |0.0003f+0.04|}{247} = 0.0772m$. The MAE of NPC is $\frac{\sum_1^{247} |0.0093f+0.7|}{247} = 1.8532m$.

The utilization of power control methods can get better transmit power efficiency (up to 97%) than the NPC method (43%). With power control methods, both UWB nodes can mitigate the uncertain multipath effects during the double sided wireless transmission and get almost the same and accurate range estimates which meet the reference moving path. The power controlled system can stabilize the ranging channel, but the NPC system obtains highly variable ranging estimates ($0 \sim 4$m difference) during the moving period.

4.5 Chapter Summary and Conclusion

In this chapter, the features of the IEEE 802.15.4-2011 UWB propagation in multipath environments were analyzed based on the results recorded from extensive ranging experiments. The relationship between transmit power, transmission range, SNR and ranging performance in line of sight (LOS) and non line of sight (NLOS) conditions was extracted through the ranging measurements. A novel bilateral transmitter output power control algorithm was proposed to maintain the target SNR and improve the ranging performance in LOS condition. In NLOS conditions, the ranging performance is mainly affected by that the propagation of electromagnetic waves is slower in some materials compared to air. The validation of the algorithm was performed in both the stationary and mobile cases in realistic ranging scenarios.

The features of the IEEE 802.15.4-2011 UWB propagation were observed as follows. (1) In LOS conditions, the SNR has an effect on the instantaneous accuracy. High SNR indicates a stable multipath channel. (2) The SNR, as a function of distance, is not log-linear in multipath propagation if the UWB transceiver is not well designed. The SNR increases firstly to reach a maximal value and then decreases with distance increasing. The maximal SNR is an inflexion point. Before this inflexion point, the shorter transmission range makes the ADC go into saturation and results in a lower SNR. After this inflexion point, the SNR decreases with increasing distance, due to the thermal and quantisation noise. The use of different transmit powers has various inflexion points. (3) High SNR can smoothen the channel impulse response in NLOS propagation, but can not achieve good ranging performance. The ranging performance in NLOS propagation is mainly affected by the extra propagation delay.

The bilateral transmitter output power control algorithm was presented which is capable of dynamically controlling the outputs of the IEEE 802.15.4-2011 UWB nodes to stabilize the multipath channel. The experimental results revealed that this novel algorithm can: (1) cooperate seamlessly with a symmetric double sided two way TOA based ranging paradigm; (2) compensate for uncertain multipath effects and maintain connectivity and (3) improve the ranging performance.

Chapter 5

Fully-Coupled Hybrid IEEE 802.15.4-2011 Ultra Wideband and Inertial Measurement Unit Localization System

This chapter presents a fully-coupled architecture for the hybrid UWB and IMU localization system. Three fusion algorithms for relative position estimation of an object are proposed, including the pure inertial navigation system (INS), INS plus UWB ranging correction, and orientation plus ranging algorithm. A proof-of-concept fully-coupled positioning scheme is implemented and tested in three practical cases related to indoor localization. Experimental results are finally reported.

5.1 Introduction

The limitations of existing architectures of the hybrid UWB and IMU systems are that they do not exchange data with other network nodes since the UWB channel is dedicat-

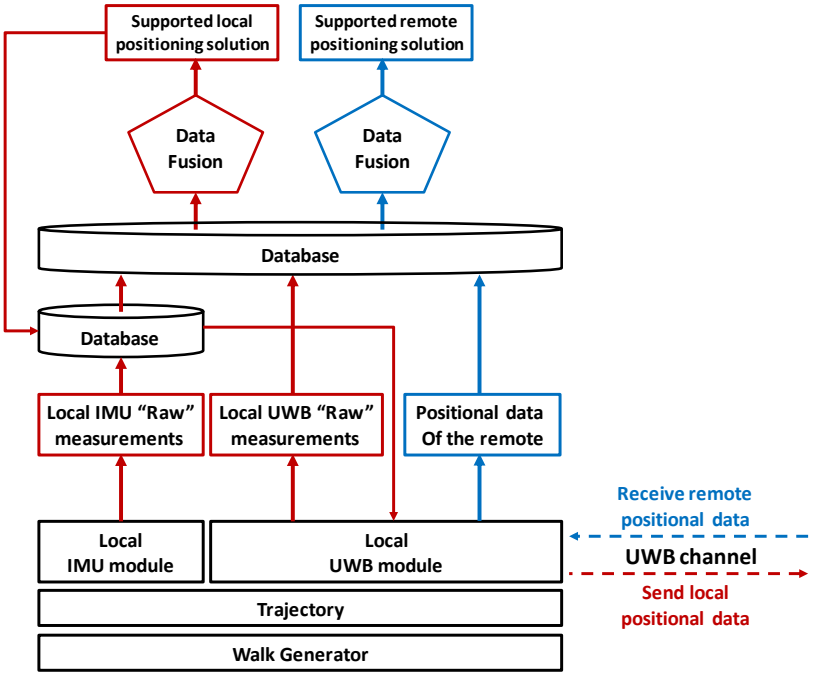

Figure 5.1: Fully-coupled architecture at a single node.

ed to ranging alone. The UWB communication is therefore poor power performance. The hybrid UWB and IMU systems can not perform simultaneous local-positioning and remote-tracking of the objects. The solution in many cases is to supplement the system with an additional wireless technology, which, in turn, increases the cost and size of the infrastructure and further complicates data synchronization.

5.2 Fully Coupled Architecture

In this work, to address the limitations of existing architectures of hybrid UWB and IMU systems and improve the overall performance of indoor localization, a fully coupled architecture is proposed, which is illustrated in the Figure 5.1.

The trajectory is generated by the walk generator. At the receiving time, the 'raw' measurements of local IMU and UWB modules and the remote positional data received through an UWB channel are stored in a database. The database is populated by location data from each node communicating in the network. Then, the specifi-

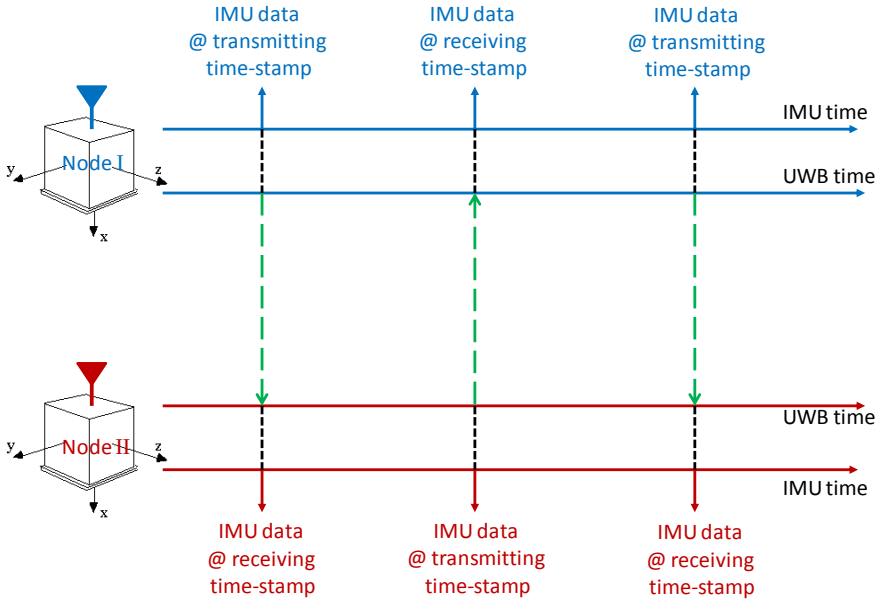

Figure 5.2: Positional data exchange scheme in fully-coupled architecture.

cally synchronized positional data in the database are fused for local-positioning and remote-positioning. At transmit time, the specific updated positional data and other useful information of the local node is sent to the remote nodes.

In order to implement an efficient mutual positioning, a 'local' and 'remote' synchronization mechanism must be realized. For example, as shown in Figure 5.2, node II receives the IMU data and UWB signal from node I; the UWB measurements are synchronized with the local IMU data for position estimation. Likewise, node I receives the IMU data and UWB signal from node II; the UWB measurements are synchronized with the local IMU data for position estimation.

The advantages of the fully-coupled architecture for indoor positioning are concluded as follows. (1) It can perform data exchange with other network nodes using the UWB channel, and thus makes simultaneous local-positioning and remote-tracking possible, and improve the power performance of UWB communication. (2) This reciprocal data distribution allows several nodes to track one another and for each node to consider its mobile neighbors as anchors. This approach therefore has the potential to reduce the overall number of anchors needed for positioning, and thus the total cost of the

system. (3) Positioning accuracy can be improved by combining the complementary advantages of UWB and inertial sensors. Inertial data can be employed to compute the traveled trajectory when UWB measurements are absent due to range limitations or adverse NLOS conditions. UWB localization can supplement inertial data to discriminate between accurate measurements and data corrupted by noise and drift.

5.3 Practical Data Exchange

In practice, in order to efficiently implement mutual positioning, a bidirectional positional data exchange methodology must be realized.

Considering the IMU components of two independent hybrid modules, it is not possible to assume a synchronous or constant sampling rate, due to elements such as clock drift and asynchronous event triggering. The UWB ranging sampling rate generates data with an irregular cadence also. This is due to the dependence, in the ranging estimation, on the TOF measurements and processing delays, which, in turn, are strongly correlated with hardware limitations and the varying distance associated with the ambulatory environment.

In order to utilize the latest positional data for the remote tracking, a positional data exchange scheme is proposed in this work as shown in Figure 5.3. It assumes the architecture schematic for a 2 node scenario (an anchor and an object, respectively). The anchor IMU module estimates its 3D orientation and stores it chronologically in a local database, which is periodically updated. Simultaneously, when the onboard UWB radio is transmitting a wireless signal to perform ranging, the latest inertial data accumulated in the database and specific positional information are integrated into the transmitted UWB packet. The maximum temporal difference between the UWB signal and the inertial orientation is the IMU 3D orientation algorithm sampling time, for instance, 1 ms in case of a 1KHz sampling rate. Subsequently, the UWB radio

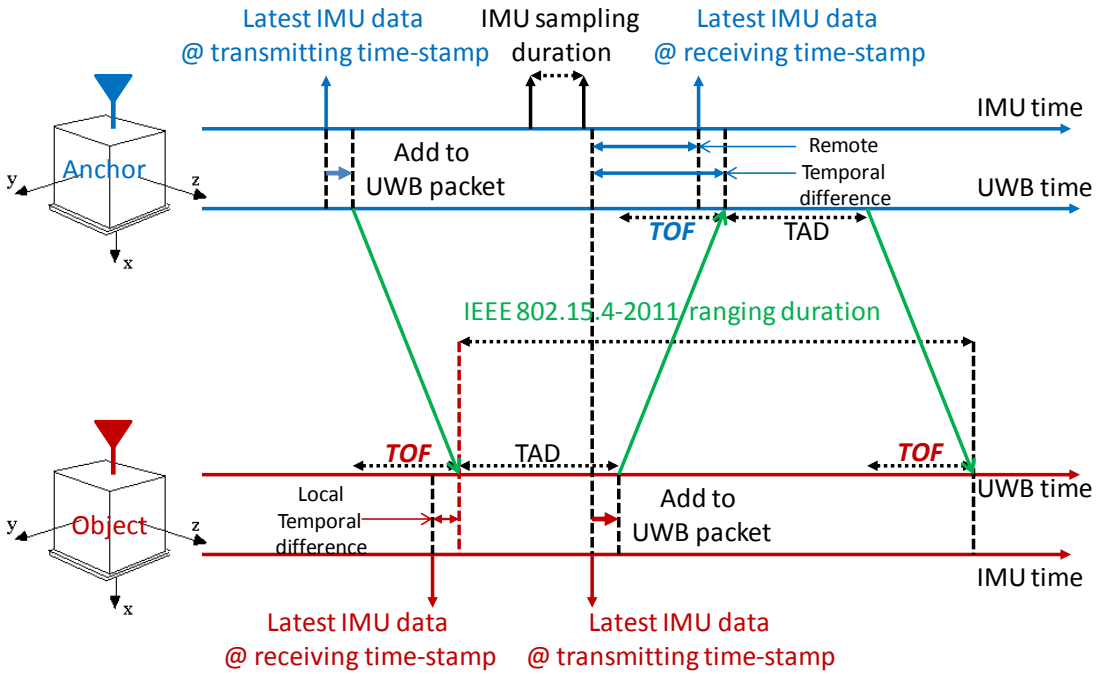

Figure 5.3: Practical positional data exchange scheme.

in the object receives the packet and, in accordance with the SDS-TW-TOA ranging protocol, retransmits a signal to the anchor, contained in which is the latest inertial data, stored in object's local inertial database, along with the distance estimated from the received ranging information.

Upon receiving this transmission, the anchor is subsequently able to complete the SDS-TW-TOA ranging calculation 'locally' and to associate this distance value with the latest locally generated inertial sample. In addition, it receives the latest object's inertial measurements. The maximum temporal difference between the anchor's TOF data and the latest object's inertial data is equal to the IMU sampling duration plus a TOF. The maximum temporal difference between the anchor's IMU data and the latest object's IMU data is equal to the sum of the TOF and IMU sampling duration. In case of indoor short-range areas (up to 100 m or 333.33ns) and with high IMU orientation sampling rate (> 1 KHz, or 1ms), the TOF contribution can be neglected. Hence, these contributions have the same weight.

All latest positional measurements recorded at a single node are stored in the database

including the latest local distance and orientation, latest remote orientation and other specific positional information. Then, these positional measurements are fused for local- and remote-positioning. For local-positioning, the object completes a TOF estimation at the receiving timestamp and associates TOF data with the latest IMU data generated locally. For "remote" positioning, the object adds the latest generated IMU data to the UWB packet which is going to be transmitted to the anchor at the transmit timestamp. After the wireless communication, when this packet is arrived, the anchor encodes the object's inertial data and associates them with the latest TOF and IMU measurements which are estimated locally at the receive timestamp.

5.4 Data Fusion Algorithms

The fully-coupled sensor fusion introduced in the previous section requires a positioning model to merge measurements from the UWB and IMU modules. In this work, two nodes are employed to set up a proof-of-concept system. Each node consists of two modules, an IMU and an IEEE 802.15.4-2011 UWB transceiver, as shown in Figure 5.4.

The IMU consists of an array of 3D accelerometer, 3D gyroscope, and 3D magnetometer coupled with a high resolution analog-to-digital converter (ADC). This IMU module is based on the modular Tyndall 25mm mote platform [21]. Orientation is estimated by the IMU in real-time 10 times per second employing the well established low computational methodology described in [59]. The IEEE 802.15.4-2011 UWB transceiver is provided by the *Decawave* Company [11], which calculates the distance every 0.6 seconds, as described in section 3.2, chapter three.

The measurements in the database include orientation estimated from IMU module, distance measured from UWB module and remote positional data. Based on this point-to-point setup, three fusion algorithms for relative position estimation of the mobile

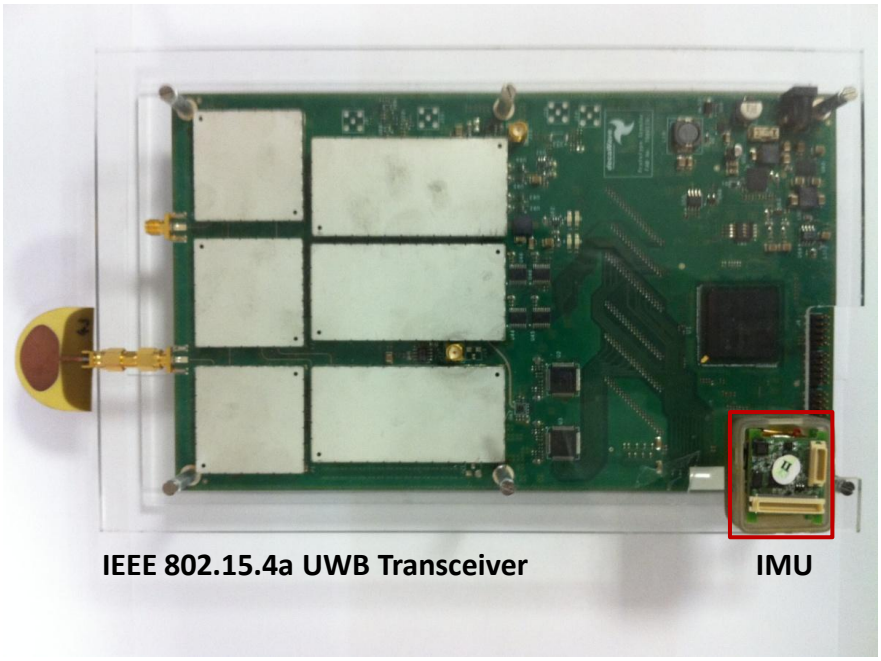

Figure 5.4: The sensor node integrating an IEEE 802.15.4-2011 UWB and an IMU.

object are considered in this work, namely pure inertial navigation system (INS), INS with UWB correction and orientation plus ranging. The anchor's position represents the origin of a Cartesian coordinate system whose orientation is employed to establish a reference frame.

5.4.1 Inertial Navigation System

In this work, a pure inertial navigation system is firstly considered. Only yaw measurement of the IMU is used for navigation in a 2D plane. Therefore, the position of the object calculated using inertial navigation algorithm can be expressed as

$$\begin{cases} X_{n+1} = X_n \pm v_{x,n+1} \bullet dt \\ Y_{n+1} = Y_n \pm v_{y,n+1} \bullet dt \end{cases} \tag{5.1}$$

where,

$$\begin{cases} v_{x,n+1} = \bar{v} \times cos(\Phi_{n+1}) \\ v_{y,n+1} = \bar{v} \times sin(\Phi_{n+1}) \end{cases} \tag{5.2}$$

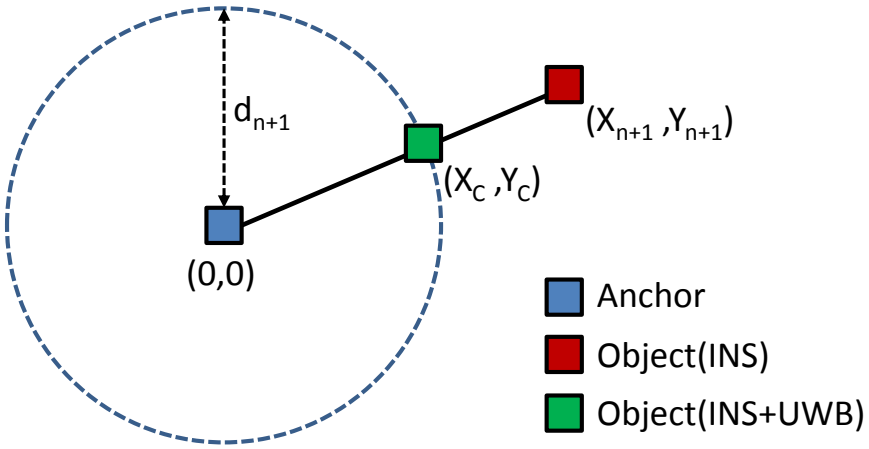

Figure 5.5: INS with UWB correction.

Where, (X_{n+1}, Y_{n+1}) indicates the next position of the object node, (X_n, Y_n) is the current position, dt is the sampling time, $\bar{v}$ is the magnitude of traveling speed, and Φ_{n+1} is the difference between the yaws estimated by the object and anchor nodes. It is worth pointing out that, in the previous formula, the sign '+' is necessary in case the object node moves forward, the opposite when it moves backward.

Although the discrimination between the two movements is trivial due to the presence of a gyroscope in the IMU module, for simplicity, it is assumed that the object node moves forward only. The initial position of the object is known. The positions of the object are relative to the starting point. Furthermore, even though the speed magnitude could be estimated by means of a double integration of the acceleration (after the transformation from the body to the global reference and a gravity subtraction), in this work, it is assumed to be constant for the present experiment.

5.4.2 INS with UWB Ranging Correction

Inertial measurements are typically affected by errors, such as drift and bias, which influence the accuracy of the previous approach [59].

To mitigate such effects of drift and bias, an INS with UWB ranging correction is considered. A description of the method is shown in Figure 5.5.

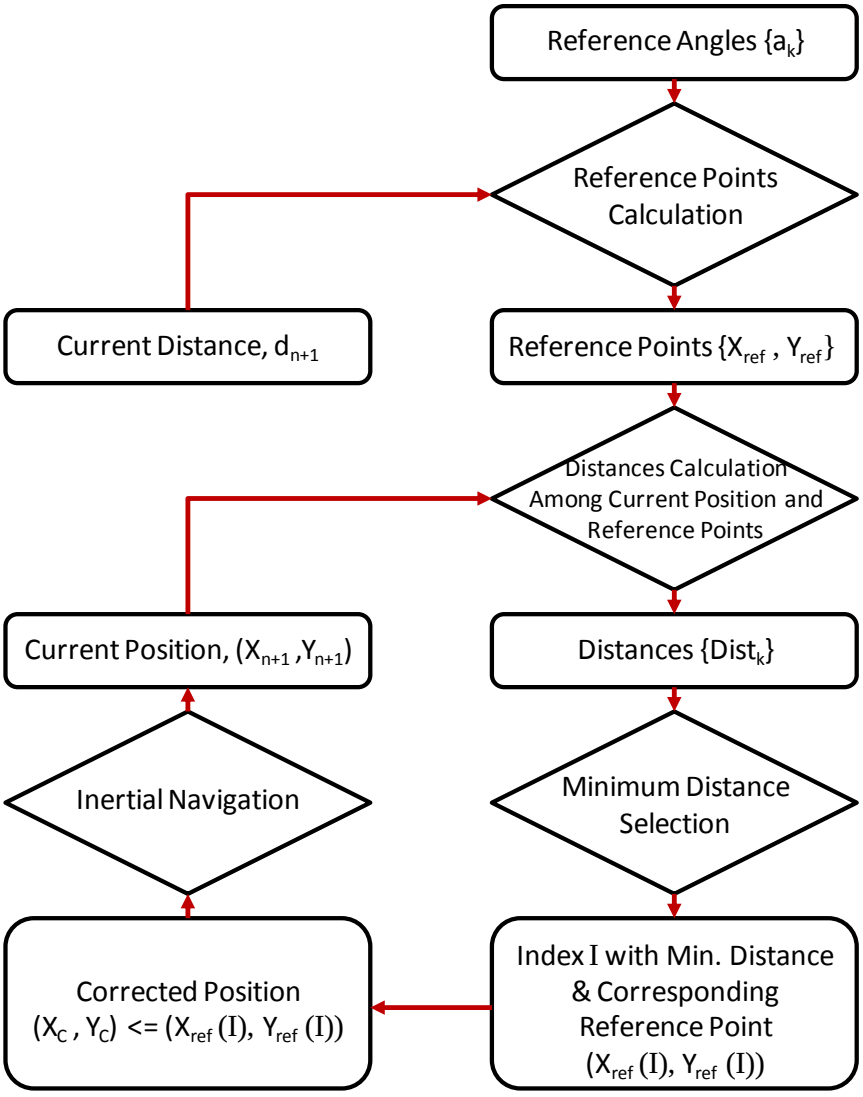

Figure 5.6: Flowchart of INS with UWB correction approach.

It consists of estimating the point with the shortest distance among the position currently estimated with the pure INS approach (X_{n+1}, Y_{n+1}) and the points in a circle having the anchor position as center and radius equal to the current UWB ranging measurement d_{n+1} as per the TOF-based ranging algorithm. The corrected position of the object is taken as (X_c, Y_c) and represents the new estimated position of the object node and represents (X_n, Y_n) in the subsequent iteration of the INS algorithm (equations (5.1), (5.2)).

The flowchart of INS with UWB correction approach is illustrated in Figure 5.6. The reference angles are firstly selected depending on the number of the distance measure-

ments as

$$\{a_k\} = \{0 : \frac{360^o}{n+1} : 360^o\}; k = n+1; n = 0,1,2,...,N \tag{5.3}$$

Then, the currently measured distance d_{n+1} and the reference angles $\{a_k\}$ are used to calculate the reference points in the circle with anchor position (origin) as circle center as

$$\begin{cases} X_{ref}(k) = d_{n+1} \times cos(a_k) \\ Y_{ref}(k) = d_{n+1} \times sin(a_k) \end{cases} \tag{5.4}$$

The distances among current position (X_{n+1}, Y_{n+1}) measured by pure INS approach and the reference points are then calculated as

$$\{Dist_k\} = (X_{ref}(k) - X_{n+1})^2 - (Y_{ref}(k) - Y_{n+1})^2 \tag{5.5}$$

The minimum distance is:

$$D_{min} = min\{\{Dist_k\}\}, k = n+1; n = 0,1,2,...,N \tag{5.6}$$

The reference point corresponding to minimum distance D_{min} in $\{Dist_k\}$ is regarded as the correct position of the object which is taken as

$$\begin{cases} X_c = X_{ref}(I) \\ Y_c = Y_{ref}(I) \end{cases} \tag{5.7}$$

Where, the I is the index with minimal distance of $\{Dist_k\}$. The corrected position (X_c, Y_c) then represents the new estimated position of the object and represents (X_n, Y_n) in the subsequent iteration of the INS algorithm. Such corrections can be performed

as often as the needed in order to meet the desired level of accuracy.

5.4.3 Orientation Plus Ranging

Another position estimation approach is using orientation and ranging measurements. The orientation includes roll, pitch, and yaw components. To estimate the object's movement in a 2D plane, the roll and pitch angles are theoretically constant values. It is therefore only distance and yaw angle are considered for the position estimation in 2D plane. The stationary coordinate is defined arbitrarily with the vertical axis and origin pointing up. The anchor is selected as the origin, the directions measured from the IMU body coordinate are regarded as the X-axis (North direction 0^o) and Y-axis (West direction), see Figure 5.7.

5.4.3.1 Problem Statement

The object moves forward in this work, that implies that the moving direction and yaw angle are the same. There are four situations of the instant yaw and distance.

• Situation (1): Both distance and yaw are not changed when the object is stationary.

• Situation (2): Distance value is unvarying, but the yaw varies when the object rotates locally or moving regularly on a circle.

• Situation (3): Yaw is unvarying, but the distance varies when the object moves on a straight path only.

• Situation (4): Both are varying when the object rotates to move to other paths such as moving on a cross-type road.

According to the classic trigonometric function, using the distance d_{n+1} between two nodes for position estimation requires a corresponding angle α, see Figure 5.7, the α is the angle enclosed by the lines from point object to point anchor and point anchor

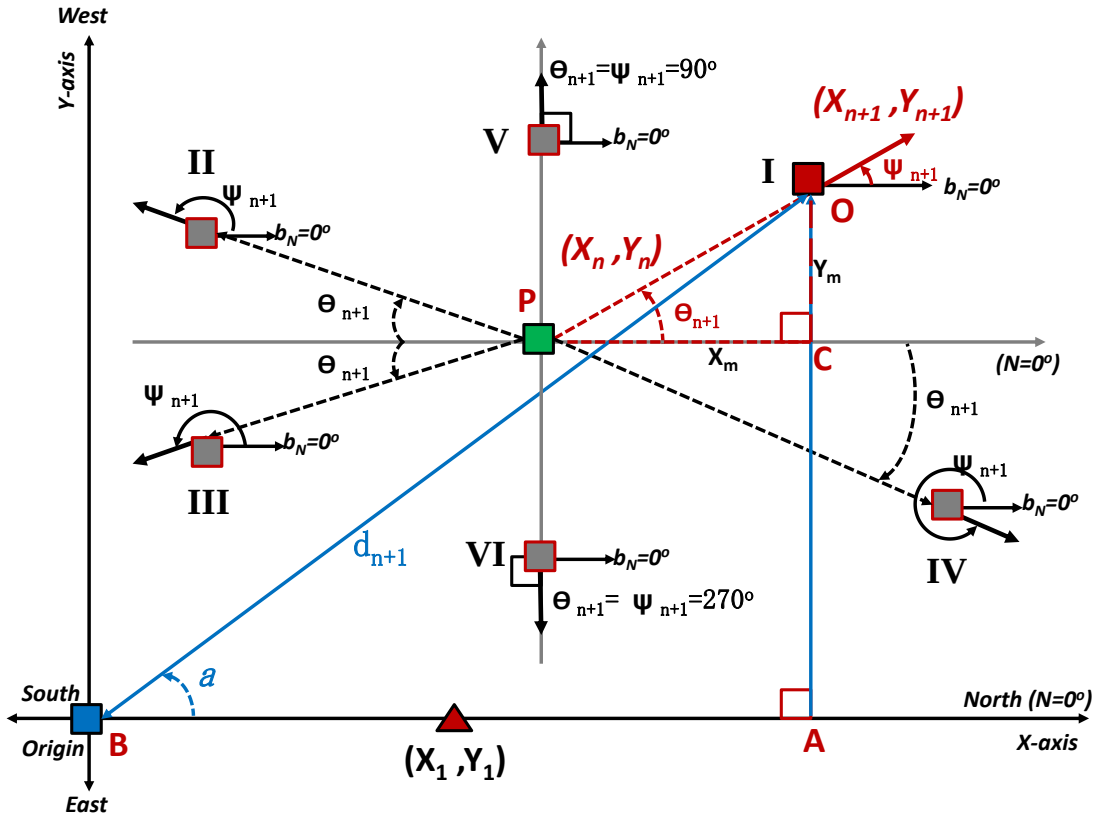

Figure 5.7: Resources available for position estimation of the object when it travels from the current position (X_n, Y_n) (green square block) to a new position (X_{n+1}, Y_{n+1}) (red square block). A start-point (X_1, Y_1) (red triangle), one anchor is used in this hybrid position system and it is chosen as the origin (blue square block).

to the north direction. In situations (1) and (3), which are well controlled, the yaw angle can be directly used as the α. However, in situations (2) and (4), there are not enough variables to measure this α with only one distance and one yaw angle. There is no absolute correlation between the yaw and α. That because of the yaw angle is related to the direction of IMU body coordinate b (b_N in Figure 5.7 represents the north direction of the IMU body coordinate), but α is related to direction of one distance based position coordinate, and both coordinates are isolated.

5.4.3.2 Position Estimation

Some resources available are considered for position estimation including the initial position (X_1, Y_1) and the latest position (X_n, Y_n) previous to the next new position

(X_{n+1}, Y_{n+1}).

These variables make up two right angled triangles with IMU body-coordinate and position coordinate. For instance, see Figure 5.7, when the object moves from position P to a new position O, Triangles AOB and COP can be found. Therefore, according to the trigonometric function, two mathematical functions can be obtained with respect to data d_{n+1}, (X_{n+1}, Y_{n+1}), ψ_{n+1}, (X_n, Y_n), X_m, Y_m. $X_m = |X_{n+1} - X_n|$ is the distance between X_{n+1} and X_n, $Y_m = |Y_{n+1} - Y_n|$ is the distance between Y_{n+1} and Y_n. $\tan(\theta_{n+1}) = \frac{Y_m}{X_m}$. Here, the θ_{n+1} is the angle enclosed by the lines from point object to point O and point P to the X-axis. Mathematically, θ_{n+1} belongs $[0^o, 90^o]$ in the four regions of the position coordinate based on a virtual origin (X_n, Y_n). Due to the assumption of moving forward of the object, the θ_{n+1} can be obtained from the ψ_{n+1} of the IMU body-coordinate. For instance, the situation I in region I, $\theta_{n+1} = \psi_{n+1}$; situation II, $\theta_{n+1} = 180^o - \psi_{n+1}$; situation III, $\theta_{n+1} = \psi_{n+1} - 180^o$; situation IV, $\theta_{n+1} = 360^o - \psi_{n+1}$; situation V, $\theta_{n+1} = \psi_{n+1} = 90^o$; situation VI, $\theta_{n+1} = 360^o - \psi_{n+1} = 90^o$.

Depending on the situations of θ_{n+1}, the real-time position (X_{n+1}, Y_{n+1}) can be calculated as follows:

$$\begin{cases} X_{n+1}^2 + Y_{n+1}^2 = d_{n+1}^2 \\ \tan(\theta_{n+1}) = \tan(\psi_{n+1}) = \dfrac{|Y_{n+1} - Y_n|}{|X_{n+1} - X_n|}, \psi_{n+1} \subset [0^o, 90^o) \\ X_{n+1} = X_n, \psi_{n+1} = 90^o \\ \tan(\theta_{n+1}) = \tan(180^o - \psi_{n+1}) = \dfrac{|Y_{n+1} - Y_n|}{|X_{n+1} - X_n|}, \psi_{n+1} \subset (90^o, 180^o] \\ \tan(\theta_{n+1}) = \tan(\psi_{n+1} - 180^o) = \dfrac{|Y_{n+1} - Y_n|}{|X_{n+1} - X_n|}, \psi_{n+1} \subset (180^o, 270^o) \\ X_{n+1} = X_n, \psi_{n+1} = 270^o \\ \tan(\theta_{n+1}) = \tan(360^o - \psi_{n+1}) = \dfrac{|Y_{n+1} - Y_n|}{|X_{n+1} - X_n|}, \psi_{n+1} \subset (270^o, 360^o] \end{cases} \tag{5.8}$$

Where, the n is integer and $n \subseteq [1, +\infty]$. To estimate the first position of the object, the

initial position (X_1, Y_1) is required. This is another assumption of this fusion algorithm.

Mathematically, equation (5.8) generates two X_{n+1} values and corresponding Y_{n+1} values. And these X-/Y-values are distributed in four different regions of the predefined position coordinate based on the origin. Hence, the problem becomes that which X-/Y-values can be used and which region of the position coordinate is specified to show the position estimates.

In this work, the object moves in the first region of the coordinate of the anchor. That implies that the X-values are positive values to be used to estimate the corresponding Y-values. Another issue is mathematical issue that $\tan(90^o)/\tan(270^o) = +\infty/-\infty$, when the $\theta_{n+1} = 90^o/270^o$, respectively. Thus, the X_{n+1} and Y_{n+1} can be calculated as follows:

$$\begin{cases} X_{n+1} = \dfrac{-2T\tan(\theta_{n+1}) + \Delta}{2(\tan(\theta_{n+1})^2 + 1))}, \theta_{n+1} \neq 90^o/270^o \\ Y_{n+1} = Y_n + (X_{n+1} - X_n)\tan(\theta_{n+1}), \theta_{n+1} \neq 90^o/270^o \\ X_{n+1} = X_n, \theta_{n+1} = 90^o/270^o \\ Y_{n+1} = |\sqrt{d_{n+1}^2 - X_{n+1}^2}|, \theta_{n+1} = 90^o/270^o \end{cases} \tag{5.9}$$

Where,

$$T = Y_n - X_n\tan(\theta_{n+1}) \tag{5.10}$$

$$\Delta = \sqrt{(2T\tan(\theta_{n+1}))^2 - 4(\tan(\theta_{n+1})^2 + 1)(T^2 - d_{n+1}^2)} \tag{5.11}$$

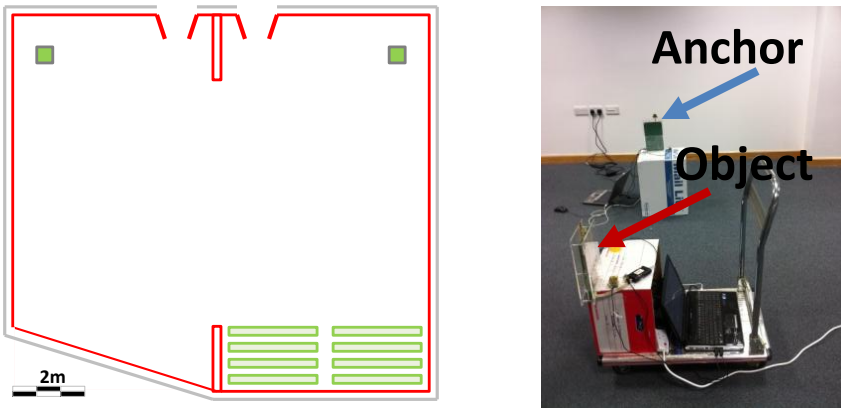

Figure 5.8: Experimental setup.

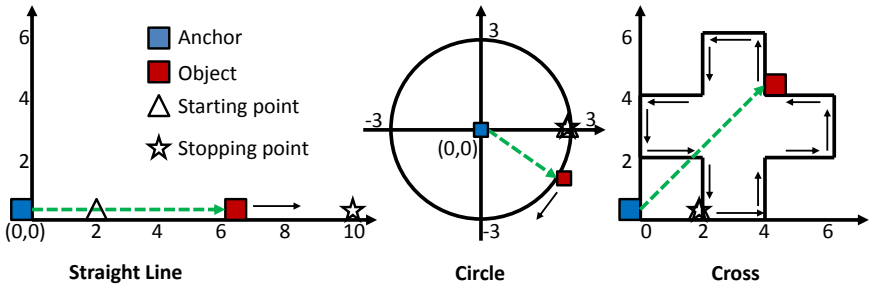

Figure 5.9: Experimental scenarios.

5.5 Practical Implementation

In this work, a practical proof of concept system for the fully-coupled approach is set up as a peer-to-peer system. The experiment entails the use of two nodes (for the purposes of the experiment known as the anchor and object, respectively), each node consists of two modules, as shown in Figure 5.4. The fully-coupled hybrid system is used to track an object moving in a relatively large conference room (approximately $12 \times 10 \times 2.5$ m), as shown in Figure 5.8.

Three experimental scenarios (Figure 5.9) have been considered. In the first one, the object moves in a straight line from the starting point (2,0) to the stopping point (10,0). In the second one, the object moves in a circle with a radius of 3m, starting and stopping at the point (3,0). In the third one, the object moves counter-clockwise in a 2D plane according to a path representing a Greek cross with equal arm width and length.

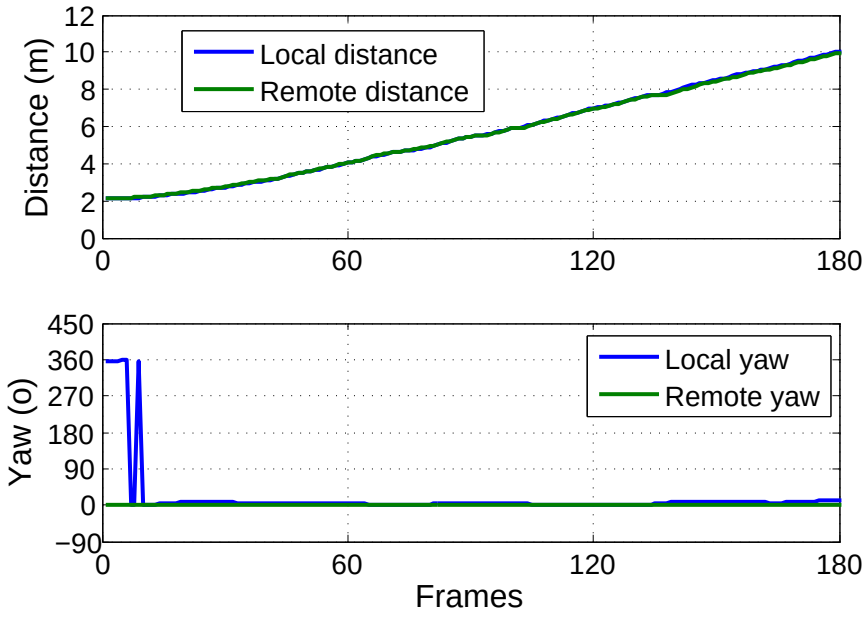

Figure 5.10: Yaw and distance measurements at the object (straight line).

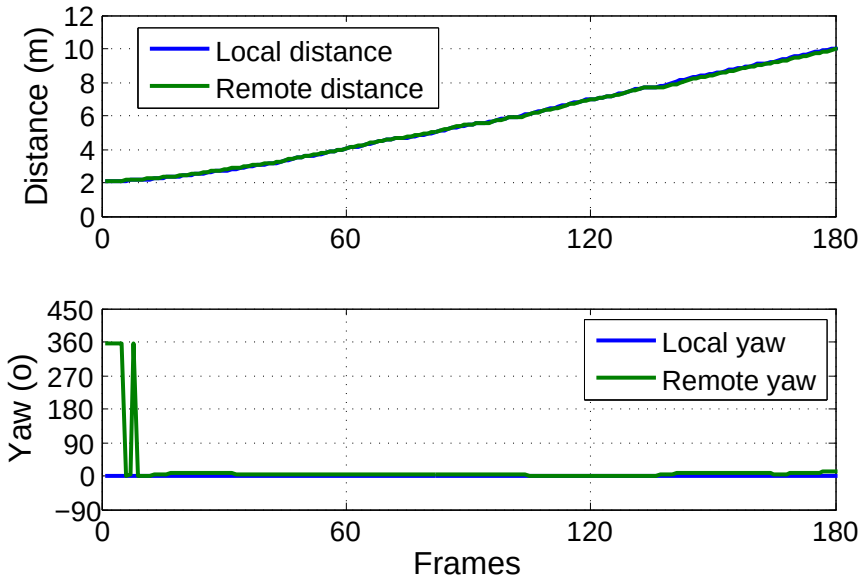

Figure 5.11: Yaw and distance measurements at the anchor (straight line).

The length of each segment of the cross is 2m and the route topology has been chosen in order to have a set of several orientation changes (13 in total) in correspondence with varying range. The start point of the mobile path coincides with the end point and is located at (2,0). The anchor is fixed at a specific point which is chosen as the origin (0,0). The real-time position estimates are shown on a 2D plane. In this work, only the yaw component of orientation is considered for position estimation.

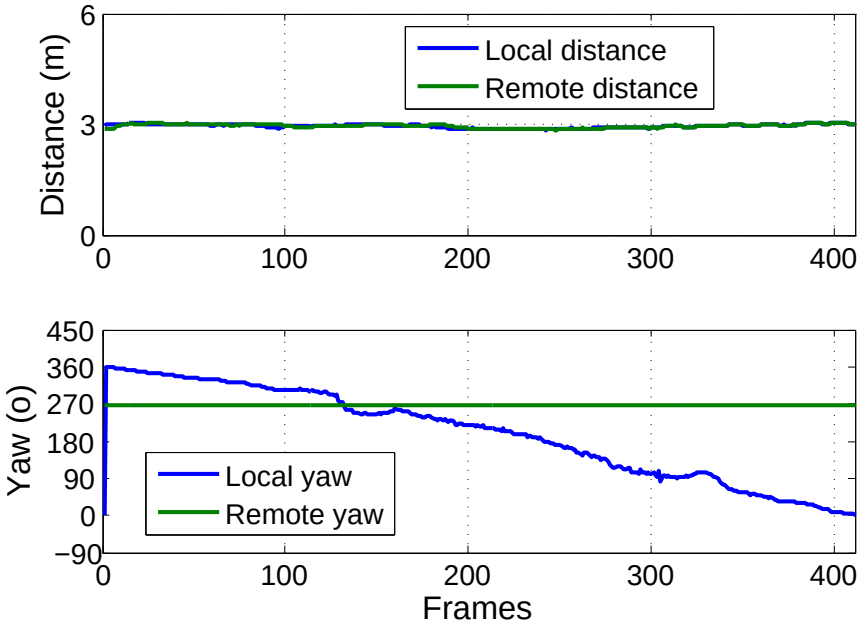

Figure 5.12: Yaw and distance measurements at the object (circle line).

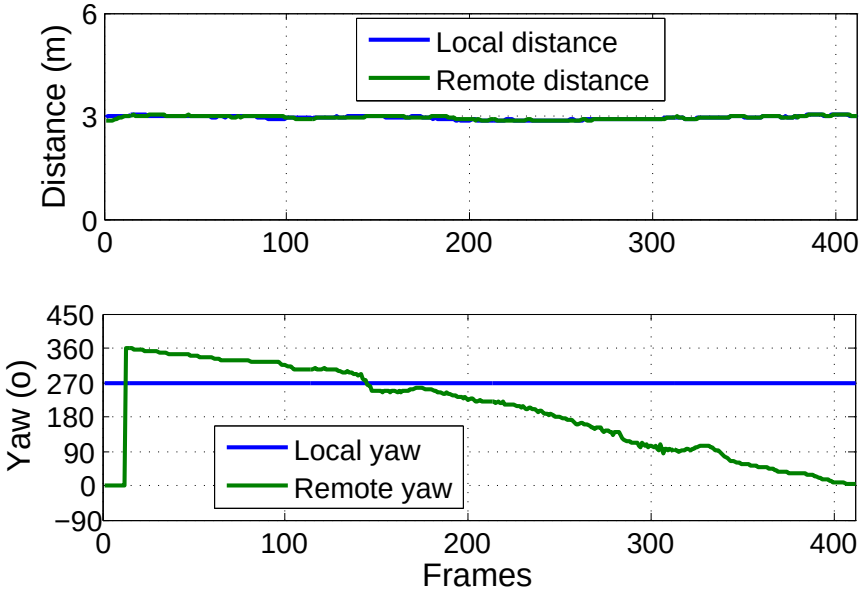

Figure 5.13: Yaw and distance measurements at the anchor (circle line).

5.5.1 Data Exchange Results

Yaw and distance measurements for the three practical scenarios are presented in Figure 5.10 to Figure 5.15.

Figure 5.10 shows positional measurements collected by the object when moving along a straight line. The object moves on a straight line path from the starting point (2,0)

to the stopping point (10,0), hence the distance changes from 2m to 10m. The yaw angle does not change, which is zero degree. Even though the yaw angles of the object changes from 0^o to 360^o, the mathematical results are the same. At the same time, the object receives the yaw and distance measurements from the anchor. Figure 5.11 shows the yaw and distance measurements collected by the anchor when the object moves on a straight line path. As the anchor is stationary, hence its yaw angle is always zero degree. However, it measures the distance to the object, which changes from 2m to 10m. Moreover, the anchor receives the object's yaw and distance measurements. These figures show that both the object and the anchor not only can get measurements from local IMU and UWB sensors, but also obtain the information from the remote node through the IEEE 802.15.4-2011 UWB channel.

Figure 5.12 describes positional measurements collected by the object when moving along a circle. The object moves on a circle path from the starting point (3,0) to points (0,-3), (-3,0), and arrives at the stopping point (3,0). Therefore, the distance does not change which is always 3m. The yaw angle changes from 360^o to 270^o, 180^o, 90^o, and finally is 0^o. Even though the yaw angles of the object changes from 0^o to 360^o at the beginning, the mathematical results of the position estimation are the same. At the same time, the object receives the yaw and distance measurements from the anchor, whose yaw angle is 270^o and distance is 3m. Figure 5.11 shows the yaw and distance measurements collected by the anchor when the object moves on a circle path. As the anchor is stationary, hence its yaw angle is always 270^o . It also updates the distance to the object. Moreover, the anchor receives the object's yaw and distance measurements. At the first 10 frames, the yaw angles of the object are 0^o, and then back to 360^o. The yaw angle curves of Figure 5.12 and Figure 5.11 are different at the beginning, but the mathematical results of the position estimation are the same. These figures also show that both the object and the anchor not only can get measurements from local IMU and UWB sensors, but also obtain the information from the remote node through the IEEE 802.15.4-2011 UWB channel.

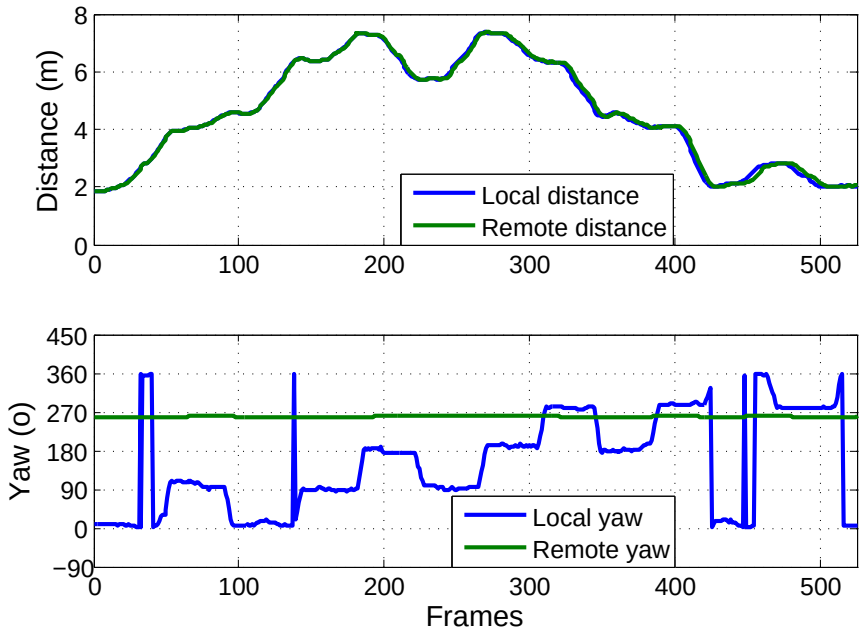

Figure 5.14: Yaw and distance measurements at the object (cross).

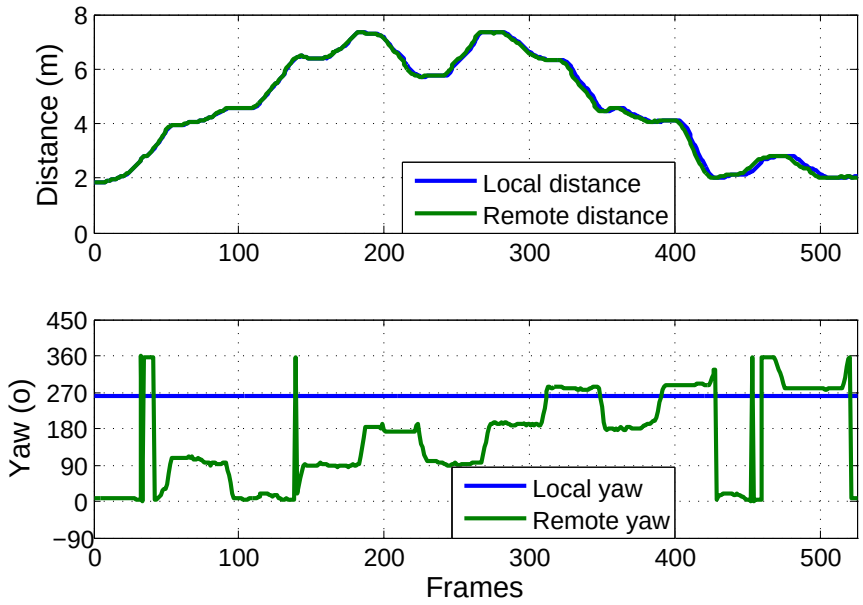

Figure 5.15: Yaw and distance measurements at the anchor (cross).

Figure 5.14 illustrates positional measurements collected by the object when moving along a Greek cross. The object moves on a cross path from the starting point (2,0) to points (4,0), (4,2), and arrives at the point (2,0). Therefore, both yaw and distance measurements change. The yaw angle changes from 0^o to 90^o, 0^o, 90^o, and finally is 0^o. The distance also changes from 2m to 4m, and finally to be 2m. At the same time,

the object receives the yaw and distance measurements from the anchor, whose yaw angle is 270^o. During the experiments, sometimes, the yaw angle measurements jump from 0^o to 360^o. However, there are mathematically the same for position estimation. Figure 5.11 shows the yaw and distance measurements collected by the anchor when the object moves on a cross path. As the anchor is stationary, hence its yaw angle is always 270^o . It also updates the distance to the object. Moreover, the anchor receives the object's yaw and distance measurements. These figures also show that both the object and the anchor not only can get measurements from local IMU and UWB sensors, but also obtain the information from the remote node through the IEEE 802.15.4-2011 UWB channel.

These results show that (1) the measurements at the object are closely the same as the data collected by the anchor; (2) the fully coupled architecture can use the IEEE 802.15.4-2011 UWB channel to perform data exchange between nodes and implement UWB ranging estimation.

5.5.2 Position Estimation Results

According to the fully coupled architecture, the system is able to implement local-positioning and remote-tracking at the object and at the anchor, respectively. The position estimation approaches using the INS, INS with UWB correction are implemented. The object node uses the yaw and distance measurements to estimate its locations as shown in Figure 5.16, Figure 5.18 and Figure 5.20. The anchor uses the received positional data and its distance and yaw measurements to track the object node as shown in Figure 5.17, Figure 5.19 and Figure 5.21.

It is evident that the positioning performance of INS-only is significantly reduced when compared to the performance achieved with the INS approach with UWB corrections. The overall error is generated due to the non-constant velocity, sensor drift, noise and ranging time lag. These error sources may cause a deviation of the X/Y positioning

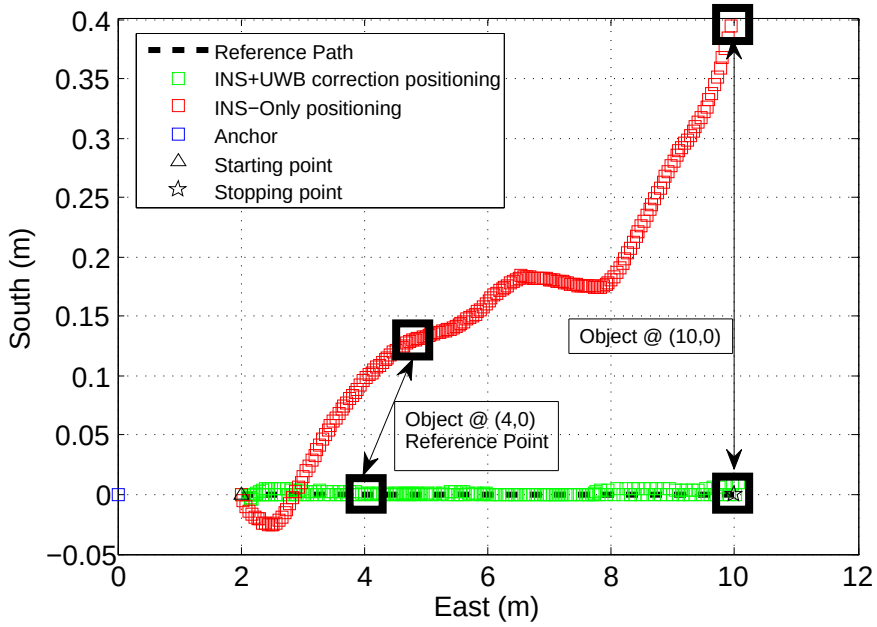

Figure 5.16: Positions of the object measured at object on a straight line.

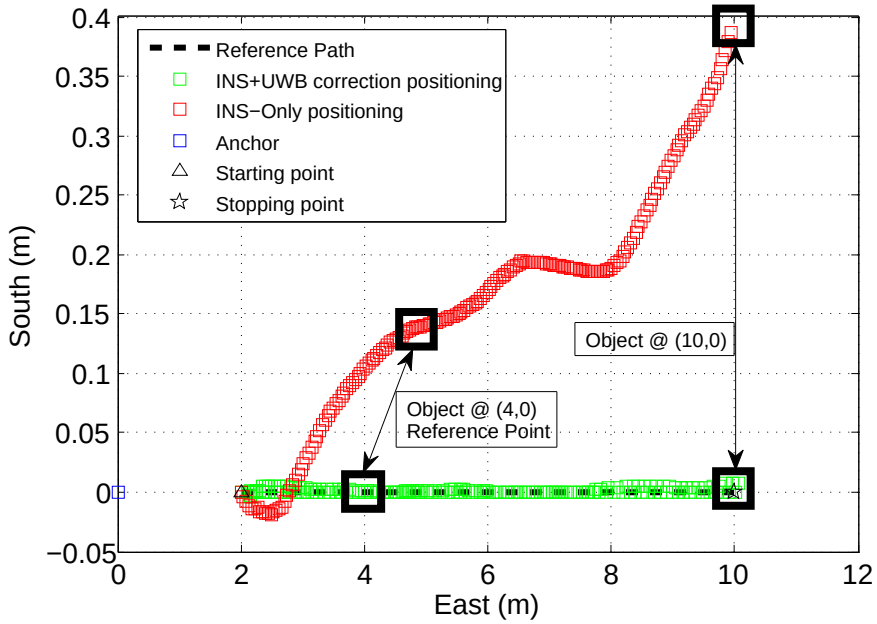

Figure 5.17: Positions of the object measured at anchor on a straight line.

values from the traveled reference points.

For instance, in Figure 5.16 and Figure 5.17, in correspondence of the reference points (4,0) and (10,0), the positions estimated by INS-only are (4.6,0.12) and (9.93,0.39), respectively. However, the positions estimated by INS with UWB correction approach at the same instants are more accurate and are equal to (4,0) and (10.05,0), respectively.

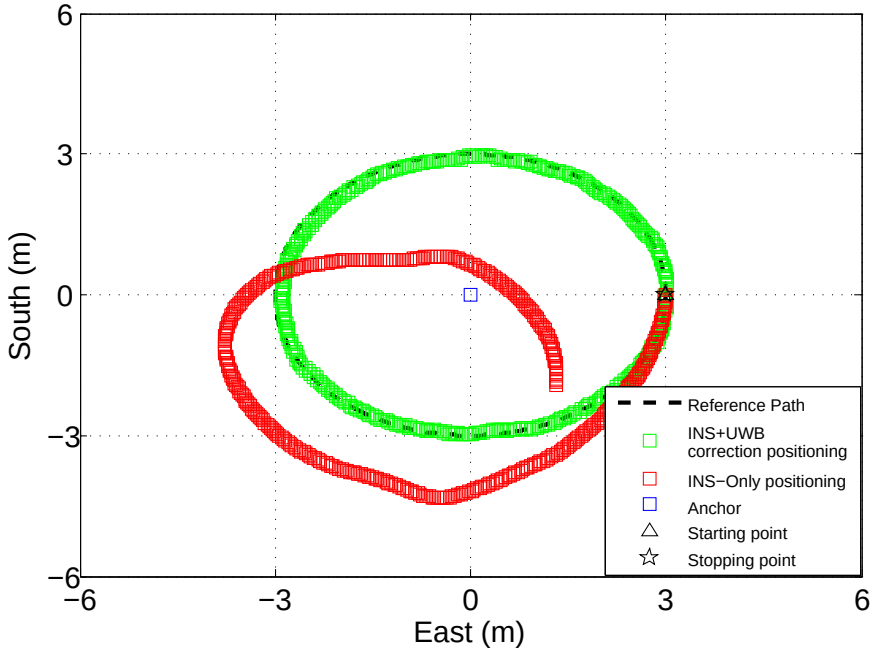

Figure 5.18: Positions of the object measured at object on a circle.

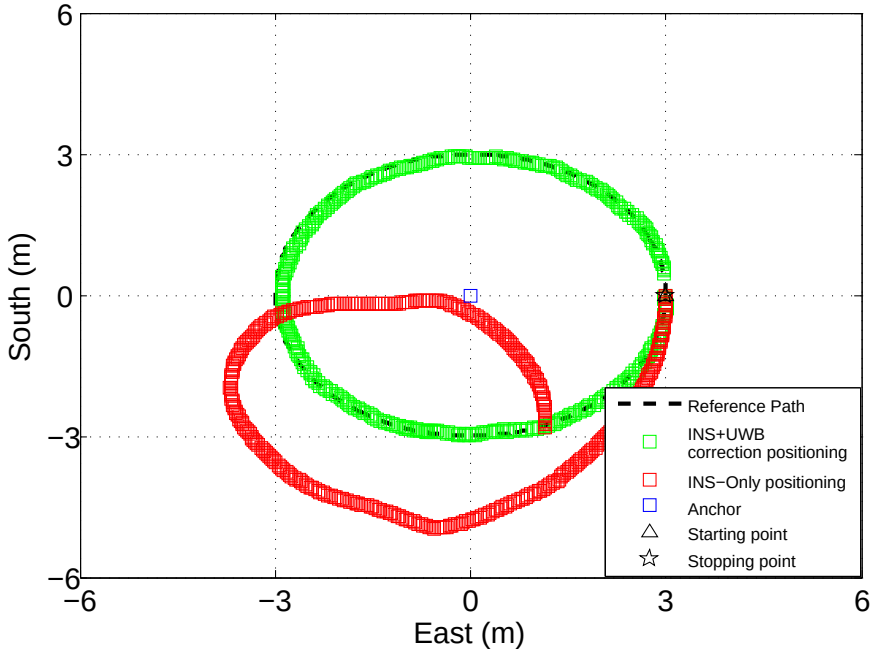

Figure 5.19: Positions of the object measured at anchor on a circle.

The positioning error is measured using a root square deviation function as:

$$\varepsilon = \sqrt{(X_m - X_{ref}^m)^2 + (Y_m - Y_{ref}^m)^2} \tag{5.12}$$

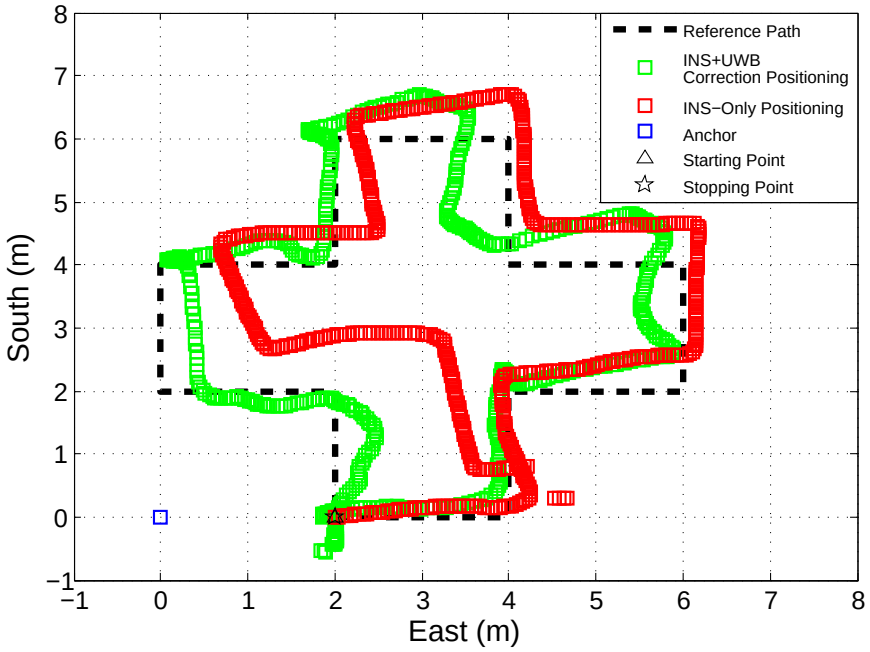

Figure 5.20: Positions of the object measured at object on a cross.

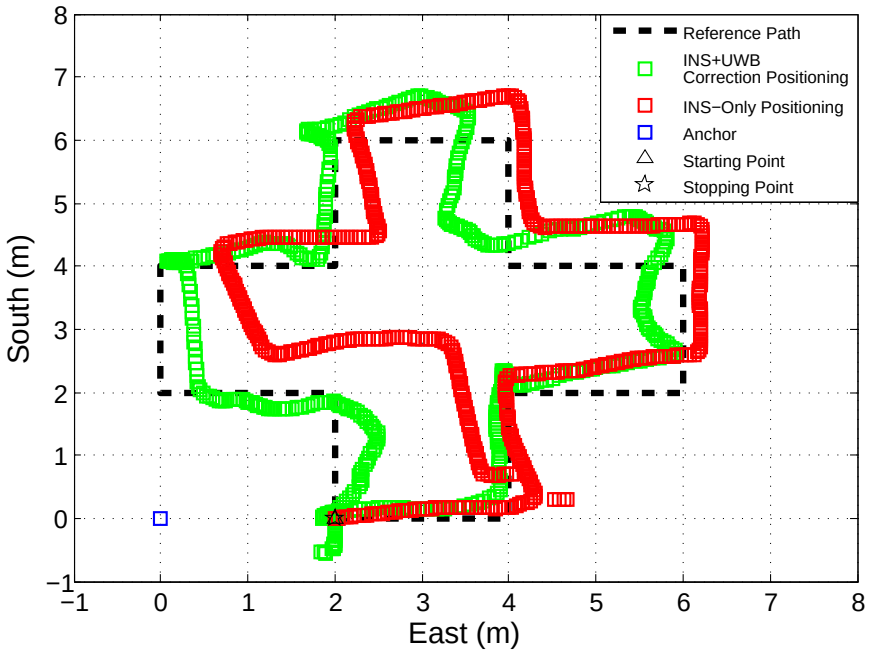

Figure 5.21: Positions of the object measured at anchor on a cross.

Where, (X_m, Y_m) is the current position estimate and (X^m_{ref}, Y^m_{ref}) denotes the related reference position. An error comparison between INS-only and INS with UWB ranging correction is illustrated in Figure 5.22 to Figure 5.24.

The experimental error as represented in Figure 5.22 is calculated in correspondence

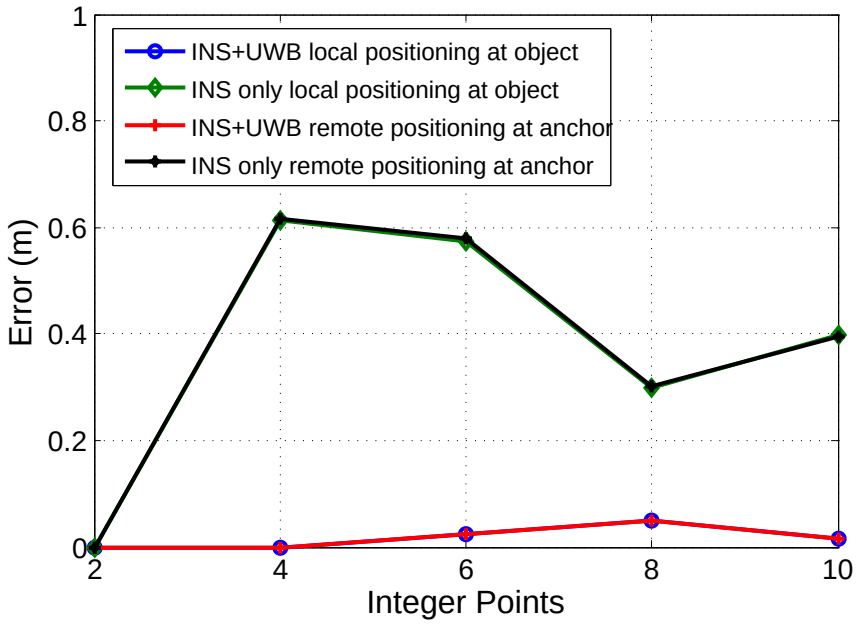

Figure 5.22: Positioning error measured on a straight line.

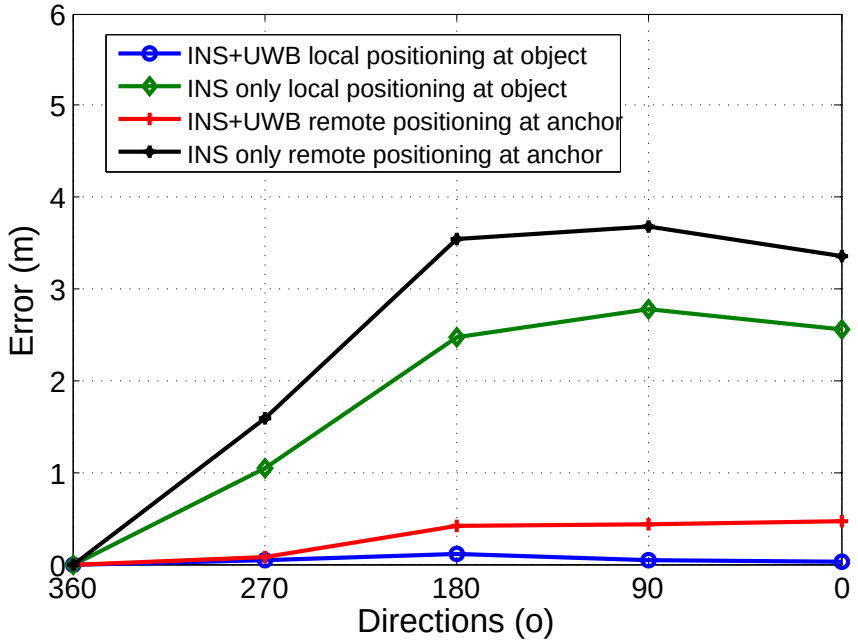

Figure 5.23: Positioning error measured on a circle.

with each integer point (e.g., point (2,0), point (4,0)) while traversing the predefined straight line reference path. The error range of INS-only approach is from 0 to 0.6m. However, the INS with UWB correction approach improves the accuracy of INS-only, and obtains less than 0.05m accuracy.

The positioning error in Figure 5.23 is calculated in correspondence with each direction

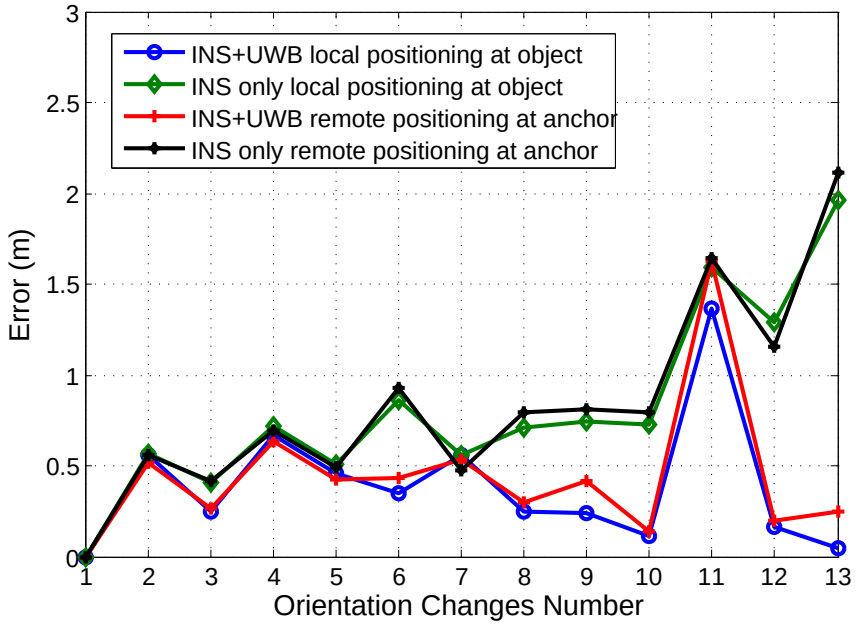

Figure 5.24: Positioning error measured on a cross.

to which the object faces (e.g., North (0^o), East (90^o)) while traversing the predefined circle reference path. The error range of INS-only approach is $0 \sim 3.7m$. The INS with UWB correction approach obtains less than 0.5m accuracy.

The experimental error as represented in Figure 5.24 is calculated in correspondence with each turn while traversing the predefined Greek cross reference path. The error range of INS-only approach is $0 \sim 2.2m$. The INS with UWB correction approach obtains obtains (less than 1.6m) higher accuracy than the INS-only approach.

In the INS case, the error is initially small however it continually increases throughout the experiment and looks toward becoming unbounded. The UWB-based correction on the other hand maintains the error almost uniformly during the experimental procedure. While the resulting error is not insubstantial it does however indicate the potential for the proposed architecture in the ambulatory context.

Table 5.1 shows the average accuracy result comparison of INS-only and INS with UWB correction approaches. When using INS only, the average position errors are 0.3778m, 2.1012m and 0.8194m in the straight line, circle and cross cases, respec-

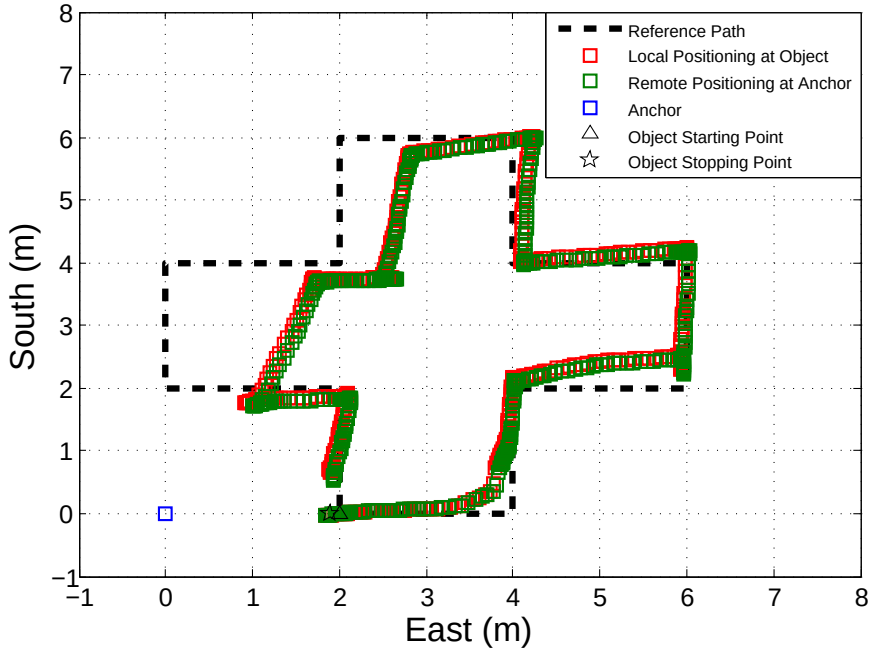

Figure 5.25: Local-positioning and remote-tracking using orientation and ranging only when object moves on a cross.

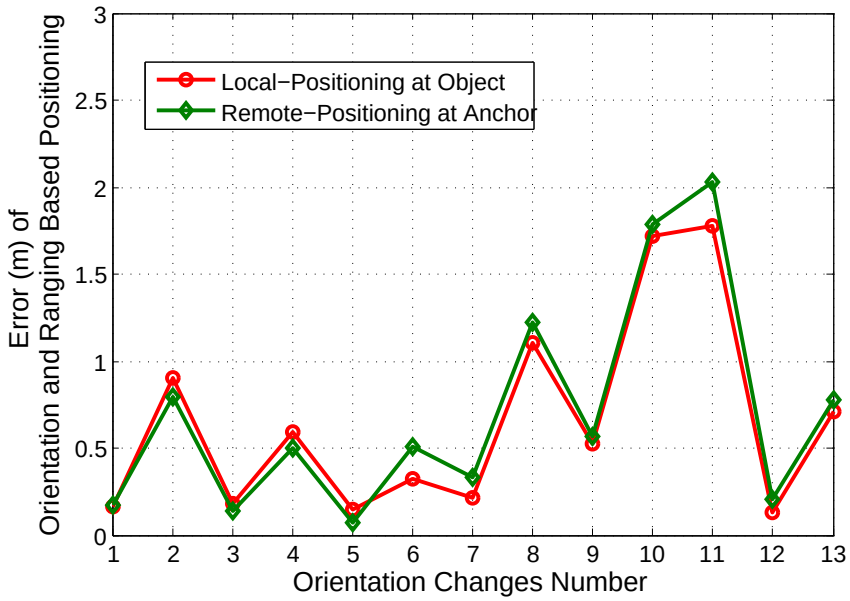

Figure 5.26: Positioning error measured on a cross.

tively. The average position errors of INS with UWB correction approach are 0.018m, 0.1601m and 0.3867m in the straight line, circle and cross cases, respectively. The INS with UWB correction approach can obtain a total average position error of 0.1883m of three practical cases, and gets 83% improvement on the pure INS (1.0994m). More-

over, this fusion algorithm gets 62% improvements on the accuracy of the existing extended Kalman filter tracking algorithm fusing UWB and INS data (0.5m) reported in [69].

Table 5.1: Performance comparison of INS-only and INS with UWB correction

	INS Only	INS with UWB correction
Average Position Error @ Straight Line	0.3778m	0.018m
Average Position Error @ Circle	2.1012m	0.1601m
Average Position Error @ Cross	0.8194m	0.3867m
Total Average Position Error	1.0994m	0.1883m

The position estimation using the orientation plus ranging only is also implemented. The object node uses its yaw and ranging measurements only to self-locate as shown in Figure 5.25. The anchor uses the received object orientation and its ranging measurements only to track the object node. The trajectory of the object measured both at the object and the anchor are approximately the same. This because of the positional data (yaw and ranging, see Figure 5.14 and see Figure 5.15) collected at the object and anchor are synchronous. There is a bit difference between local-positioning and remote-tracking. This is mainly because of the yaw and TOF estimates measured at the receiving times of both object and anchor are different due to the motion of the object.

Again from Figure 5.25, we can see that the error is initially small however it continually increases throughout the experiment. The experimental error as represented in Figure 5.26 is calculated in correspondence with each turn while traversing the predefined Greek cross reference path. According to the orientation plus ranging approach, the variables such as yaw, distance and previous position are used to estimate the new position. Therefore, the error of each previous position estimates will be accumulated for the new position estimation. Therefore, even though the position estimates at the beginning meets the moving path, however, they becomes not very accuracy and far away from the reference path, especially after the 7th turn.

5.6 Chapter Summary and Conclusion

In this chapter, a novel fully-coupled architecture was proposed for the hybrid UWB and IMU localization system. The fully-coupled architecture was designed to perform data exchange among network nodes over the UWB channel. Three fusion algorithms for relative position estimation of a mobile object were described, including inertial navigation system (INS), INS with UWB ranging correction, and orientation plus ranging. A proof-of-concept system was fully implemented and tested for locating a single object.

Compared to the loosely-coupled and tightly-coupled architectures, the fully-coupled architecture have more advantages such as 1) employing the UWB channel for both ranging and positional data exchanging with other network nodes; 2) fusing remote IMU data with local UWB ranging, and enabling simultaneous local-positioning and remote-tracking requirement of the object.

In addition, the fully-coupled architecture may have some potential capabilities. For example, the reciprocal data distribution can allow several nodes to track one another and for each node to consider its mobile neighbors as anchors at intelligently arrived at spatiotemporal points. This approach therefore has the potential to reduce the overall number of anchors needed for positioning, and thus the total cost of the system.

The INS with UWB ranging correction algorithm obtained a total average position error of 0.1883m of three practical cases, and gets 83% and 62% improvements on the accuracy of the pure INS (1.0994m) and the proposed extended Kalman filter tracking algorithm fusing UWB and INS data (0.5m), respectively.

Chapter 6

Summary, Conclusion and Future Work

6.1 Summary

This work considered using the emerging IEEE 802.15.4-2011 and inertial sensors for indoor localization. The problems mentioned in this work include: 1) the uncertain multipath components from IEEE 802.15.4-2011 UWB multipath channels affect the instant time of arrival (TOA) ranging performance; 2) the accuracy of the pure inertial navigation are affected by the bias and noise terms of inertial measurements; and 3) the existing architectures of hybrid UWB and IMU systems are limited in mutual sharing data.

This work started with an examination of ranging capabilities of the IEEE 802.15.4-2011 UWB technology. A time-based ranging paradigm was employed that is based on a symmetric double sided two way time of arrival (SDS-TW-TOA) protocol and a threshold-based leading path detection algorithm. The IEEE 802.15.4-2011 compliant UWB transceivers used for ranging estimation were supplied by *Decawave* company. The effects of multipath propagation on the accuracy and precision of ranging measure-

ments were analyzed. Three multipath propagation conditions in indoor environments were considered including line of sight (LOS), soft non line of sight (soft-NLOS) and hard non line of sight (hard-NLOS). Experimental results showed that the achievable accuracies were 0.2m in LOS over a range of 10m (e.g., signal propagates through air), 0.3m in soft-NLOS over a range of 3m (e.g., signal propagates through doors) and 1m in hard-NLOS over a range of 27m (e.g., signal propagates through concrete walls). The error of instant ranging measurements below 10cm occurred in 52% of the measurements in LOS, 33% of the measurements in soft-NLOS, and 15% of the measurements in hard-NLOS.

In order to achieve higher ranging accuracy, this work focused on the development of algorithm to stabilize the multipath channel of IEEE 802.15.4-2011 UWB. A transmit power control approach was considered in order to mitigate the noise coming from both hardware and channel environments. In order to effectively adjust the transmit power to obtain the expected SNR, extensive indoor ranging measurements were implemented. The features of IEEE 802.15.4-2011 UWB multipath propagation were observed. The relationship between transmit power, transmission range and SNR was extracted from the measurements. Based on this multipath model, a bilateral transmitter output power control algorithm was developed to cooperate with the SDS-TW-TOA protocol and bidirectionally stabilize the multipath channels between UWB systems.

In order to address the limitation of existing architectures of hybrid UWB and IMU systems, this work considered a fully coupled architecture to realize data sharing between network nodes using the UWB channel. Such a fully couple architecture is therefore able to realize synchronous local-positioning and remote-tracking of the object. Three fusion algorithms were considered to compute the object's location, including inertial navigation system (INS), INS with UWB ranging correction, and orientation plus ranging.

6.2 Conclusion

• Due to its large signal bandwidth, the IEEE 802.15.4-2011 UWB can provide high precision ranging through TOA techniques for indoor localization.

• The proposed bilateral transmitter output power control algorithm can:

(1) cooperate seamlessly with a symmetric double sided two way ranging protocol;

(2) stabilize the multipath channels;

(3) maintain the connectivity between IEEE 802.15.4-2011 UWB systems;

(4) and improve the instant ranging accuracy and stability without automatic gain control module.

• The proposed fully-coupled architecture for hybrid UWB and IMU system can

(1) perform positional data exchange with other network nodes via the UWB channel;

(2) realizing both local-positioning and remote-tracking of the object;

(3) address the limitation of mutual sharing the data with other network nodes of the loosely-coupled and tightly-coupled architectures.

• The inertial navigation system (INS) can compute the position of an object using onboard inertial measurements, capable of rejecting multipath and non line of sight conditions.

• The INS with UWB ranging correction can improve the accuracy of the pure INS.

6.3 Contributions

The main contributions to the state of the art are summarized as follows.

• The first reported performance characterization of the IEEE 802.15.4-2011 UWB for

indoor localization, and the results demonstrate the accuracy and precision of using TOA measurements for ranging applications.

• The first reported observation of the features of IEEE 802.15.4-2011 UWB propagation in indoor environments, and relationship between transmit power, transmission range and signal to noise ratio (SNR).

• A bilateral transmitter output power control algorithm is developed to stabilize the multipath channel, achieves 80% within 5cm instant ranging accuracy, and get 68% improvement on the precision of the existing non-power control methodology in LOS conditions.

• A fully-coupled architecture is developed for hybrid IEEE 802.15.4-2011 UWB and IMU localization system, which can perform data exchange with other network nodes using the UWB channel and realize simultaneous local-positioning and remote-tracking of an object.

• A fusion algorithm, called internal navigation system (INS) with UWB correction, is developed, which obtains a total average position error of 0.1883m of three practical cases, and gets 83% and 62% improvements on the accuracy of the pure INS (1.0994m) and the existing extended Kalman filter tracking algorithm fusing UWB and IMU data (0.5m), respectively.

6.4 Future Work

6.4.1 NLOS Identification and Mitigation

Even though the bilateral transmitter output power control algorithm can stabilize the multipath channel and improve the ranging accuracy in LOS conditions, the ranging error due to NLOS propagation remains.

In NLOS conditions, since the propagation of electromagnetic wave is slower in some materials compared to air the signal arrives with a delay, this introduces a positive bias in the range estimate. When the direct path to a node is completely obstructed the node's receiver can only observe NLOS components, resulting in estimated distances larger than the true distance [9].

One research direction for NLOS ranging improvement is developing a NLOS identification and mitigation algorithm. Some NLOS identification algorithms have been proposed in [53], [27]. These algorithms distinguish LOS and NLOS, by using various system parameters, such as running the variance on subsequent range estimates, the channel impulse response, root mean square delay spread, change of SNR, and their relatively presumed threshold values. NLOS mitigation goes beyond identification and attempts to counter the positive bias introduced in NLOS signals. Approaches for NLOS identification and relative mitigation can be found in [8], [44], [50], [70].

Another research direction for NLOS localization improvement is that using IMU's (human body's) orientation to detect the NLOS condition [49]. In [72], experimental results show that the signals transmitted by the UWB mobile was shown that they are not able to pass through the human body. Therefore, the orientation measurements can be conducted to assess whether the human body represents an obstacle for UWB electromagnetic waves propagation or not.

For example, in Figure 6.1, the IMU, attached to the object, is suspended together around the neck and carried on the thorax. In this configuration, UWB signals received by the anchor located in the back of the object can only result from reflected multipath. In the developed algorithm, the latest position of the object (X_n, Y_n) and the coordinates of the anchor (X_m, Y_m) are combined with the orientation Ψ_n to determinate whether a measurement is recorded in front of the pedestrian or not. For each time step, the azimuth ζ_n binding the object position (X_n, Y_n) with the anchor (X_m, Y_m) is defined. The difference $\Delta_n = \Psi_n - \zeta_n$ between the azimuth and the orientation is

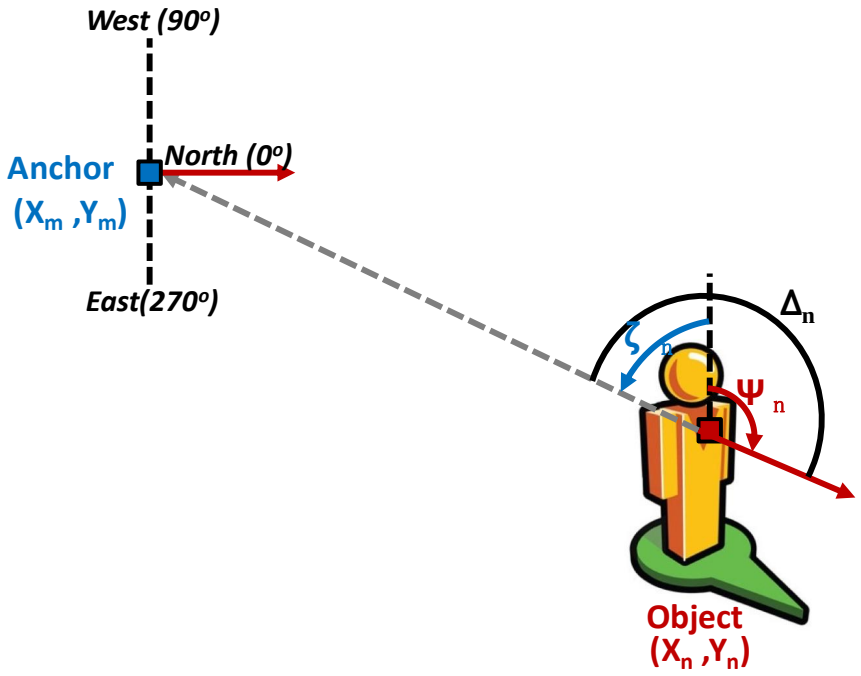

Figure 6.1: NLOS identification based on IMU orientation measurement.

then computed. When Δ_n, in absolute value, is greater than $\pi/2$, the location of the corresponding anchor is considered as being in back of the object, as shown in Figure 6.1. When the NLOS condition is detected, the next step is to design an algorithm to improve the localization accuracy. Moreover, it is worth noting that different wearable configurations should have their corresponding algorithms for NLOS mitigation.

6.4.2 Fully Coupled Localization Algorithm

The fully-coupled hybrid UWB and IMU positioning system can realize simultaneous local- and remote-tracking of the mobile objects and have potential to reduce the cost of the whole localization system. However, in order to perform absolute localization, a geometric approach such as triangulation should be considered. The triangulation algorithm requires three distance measurements. To get better accuracy, a robust fusion algorithm combining a group of UWB and inertial measurements should be considered for position estimation of the mobile objects.

Moreover, to get at least three ranging measurements, the system should allow the

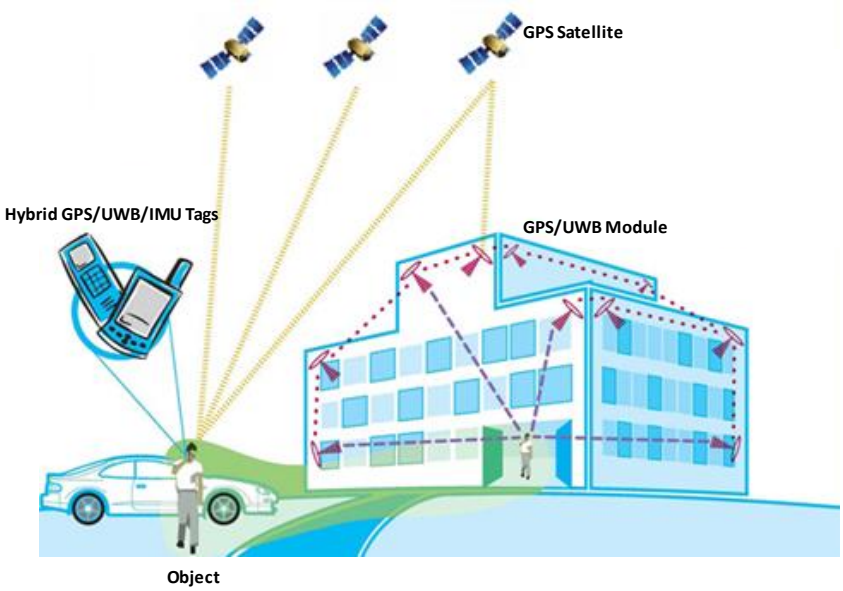

Figure 6.2: Seamless localization system using hybrid GPS/UWB/IMU system.

users to efficiently share the media spectrum range. Some issues which need more delving into are optimal location aware routing protocol for a UWB network as well as the security policy to be implemented at the (medium access control) MAC level, given that it can be used in conjunction with sensors because of its localization, low power and high security properties.

6.4.3 Low Cost and Seamless Localization

Cost and robustness are the eternal topics in the positioning system development [25]. The cost arises from capital costs such as the price per device unit and the system infrastructure. Apart from single device design using low power and low cost inertial sensors, UWB chip and a microcontroller, a system deployment algorithm is required to realize a minimum amount of infrastructure. This algorithm can be developed considering the UWB transmission range in LOS and NLOS conditions and the data exchange capability of fully-coupled architecture.

The seamless localization will be the most powerful positioning scheme in the future. The seamless positioning system covers both outdoor and indoor environments. The

integration of GPS and UWB would be a achievable solution as shown in Figure 6.2. The hybrid GPS receiver and UWB transceiver modules can be deployed in outdoor environments. The UWB access points are deployed in an indoor environment, some of which can link to the outdoor UWB transceivers. Based on the positions of these outdoor and indoor anchors, the objects wearing hybrid GPS/UWB/IMU tags can be seamlessly tracked.

References

[1] First report and order fcc 02-48. *Federal Communications Commission*, Feb 2002.

[2] Ieee std 802.15.4a. *IEEE Standard for Information Technology - Telecommunications and Information Exchange Between Systems - Local and Metropolitan Area Networks - Specific Requirement Part 15.4: Wireless Medium Access Control (MAC) and Physical Layer (PHY) Specifications for Low-Rate Wireless Personal Area Networks (WPANs)*, pages 1–203, 2007.

[3] Ieee standard for local and metropolitan area networks–part 15.4: Low-rate wireless personal area networks (lr-wpans). *IEEE Std 802.15.4-2011 (Revision of IEEE Std 802.15.4-2006)*, pages 1–314, Sept 2011.

[4] M.J. Ammann, A. Dumoulin, M. John, and P. McEvoy. Time-domain performance of printed uwb antennas. In *3rd European Conference on Antennas and Propagation*, pages 3766–3769, Mar 2009.

[5] Source: Strategy Analytics. http://www.strategyanalytics.com.

[6] Giovanni Bellusci, Daniel Roetenberg, Fred Dijkstra, Henk Luinge, and Per Slycke. Xsens mvn motiongrid: Drift-free human motion tracking using tightly coupled ultra-wideband and miniature inertial sensors. 2010.

[7] R. Bharadwaj, A. Alomainy, and C. Parini. Experimental investigation of efficient ultra wideband localisation techniques in the indoor environment. In *Antennas*

and Propagation Conference (LAPC), 2013 Loughborough, pages 486–489, Nov 2013.

[8] Roberto Casas, A Marco, JJ Guerrero, and J Falco. Robust estimator for non-line-of-sight error mitigation in indoor localization. *EURASIP Journal on Applied Signal Processing*, 2006:156–156, 2006.

[9] D. Cassioli, M.Z. Win, and A.F. Molisch. The ultra-wide bandwidth indoor channel: from statistical model to simulations. *IEEE Journal on Selected Areas in Communications*, 20(6):1247–1257, Aug 2002.

[10] Feng Chen, Reinhard German, and Falko Dressler. Towards ieee 802.15. 4e: A study of performance aspects. In *8th IEEE International Conference on Pervasive Computing and Communications Workshops*, pages 68–73, 2010.

[11] Decawave Company. http://www.decawave.com.

[12] Ciaran Connell. Scensor: An ieee802.15.4a uwb compliant chip ripe for energy harvesting, June 2009.

[13] R. Dalce, A. van den Bossche, and T. Val. An experimental performance study of an original ranging protocol based on an ieee 802.15.4a uwb testbed. In *IEEE International Conference on Ultra-WideBand (ICUWB)*, pages 7–12, Sept 2014.

[14] D. Dardari, Chia-Chin Chong, and M.Z. Win. Analysis of threshold-based toa estimators in uwb channels. In *Proceedings of 14th European Signal Processing Conference (EUSIPCO 06)*, 2006.

[15] D. Dardari, Chia-Chin Chong, and M.Z. Win. Threshold-based time-of-arrival estimators in uwb dense multipath channels. *IEEE Transactions on Communications*, 56(8):1366–1378, Aug. 2008.

[16] D. Dardari, A. Conti, U. Ferner, A. Giorgetti, and M.Z. Win. Ranging with

ultrawide bandwidth signals in multipath environments. *Proceedings of the IEEE*, 97(2):404–426, Feb 2009.

[17] Maria-Gabriella Di Benedetto and Guerino Giancola. *Understanding ultra wide band radio fundamentals*. Pearson Education, 2004.

[18] V. Dizdarevic and K. Witrisal. Statistical uwb range error model for the threshold leading edge detector. In *6th International Conference on Information, Communications Signal Processing*, pages 1–5, Dec 2007.

[19] ETHZ. Indoor uwb channel measurements from 2ghz to 8ghz. *IEEE 802.15-04-0447-00-004a*, Sept 2004.

[20] Xaviern Fernando, Srithar Krishnan, Hongbo Sun, and Kamyar Kazemi-Moud. Adaptive denoising at infrared wireless receivers. In *AeroSense*, pages 199–207. International Society for Optics and Photonics, 2003.

[21] M. Gaffney, Michael Walsh, S. O'Connell, Binyu Wang, B. O'Flynn, and C.O. Mathuna. A smart wireless inertial measurement unit system: Simplifying amp; encouraging usage of wimu technology. In *International Conference on Pervasive Computing Technologies for Healthcare (PervasiveHealth)*, pages 198–199, May 2011.

[22] S. Gezici, Zhi Tian, G.B. Giannakis, Hisashi Kobayashi, A.F. Molisch, H.V. Poor, and Z. Sahinoglu. Localization via ultra-wideband radios: a look at positioning aspects for future sensor networks. *IEEE Signal Processing Magazine*, 22(4):70–84, July 2005.

[23] J.R. Gonzalez Hernandez and C.J. Bleakley. High-precision robust broadband ultrasonic location and orientation estimation. *IEEE Journal of Selected Topics in Signal Processing*, 3(5):832–844, Oct 2009.

[24] G.A. Gray and G.W. Zeoli. Quantization and saturation noise due to analog-

to-digital conversion. *IEEE Transactions on Aerospace and Electronic Systems*, 7(1):222–223, Jan 1971.

[25] Yanying Gu, A. Lo, and I. Niemegeers. A survey of indoor positioning systems for wireless personal networks. *IEEE Communications Surveys Tutorials*, 11(1):13–32, Jan. 2009.

[26] Ashima Gupta and Prasant Mohapatra. A survey on ultra wide band medium access control schemes. *Computer Networks*, 51(11):2976–2993, 2007.

[27] I Guvenc, Chia-Chin Chong, and F. Watanabe. Nlos identification and mitigation for uwb localization systems. In *IEEE Wireless Communications and Networking Conference*, pages 1571–1576, Mar 2007.

[28] I. Guvenc and Z. Sahinoglu. Threshold-based toa estimation for impulse radio uwb systems. In *IEEE International Conference on Ultra-Wideband*, pages 420–425, Sep. 2005.

[29] Ismail Guvenc, Zafer Sahinoglu, Andreas F Molisch, and Philip Orlik. Non-coherent toa estimation in ir-uwb systems with different signal waveforms. In *Proc. IEEE Int. Workshop on Ultrawideband Networks*, pages 245–251, 2005.

[30] Rainer Hach. Symmetric double sided two-way ranging. In *IEEE P802.15 Working Group for Wireless Personal Area Networks*, June 2005.

[31] K. Haneda, K.-i. Takizawa, J.-i. Takada, M. Dashti, and P. Vainikainen. Performance evaluation of threshold-based uwb ranging methods - leading edge vs. search back -. In *European Conference on Antennas and Propagation*, pages 3673–3677, Mar 2009.

[32] R. Harle. A survey of indoor inertial positioning systems for pedestrians. *IEEEC ommunications Surveys Tutorials*, 15(3):1281–1293, Mar. 2013.

[33] G. Hein, J. Rodriguez, T. Wallner, and B. Eissfeller. Envisioning a future gnss system of systems (part 2). *Inside GNSS*, pages 64–72, Mar.-Apr. 2007.

[34] Jeffrey Hightower and Gaetano Borriello. Location sensing techniques. Technical report, IEEE Computer, 2001.

[35] Bernhard Hofmann-Wellenhof, Herbert Lichtenegger, and James Collins. *Global positioning system: theory and practice*. Springer Science & Business Media, 2012.

[36] J.D. Hol, F. Dijkstra, H. Luinge, and T.B. Schon. Tightly coupled uwb/imu pose estimation. In *IEEE International Conference on Ultra-Wideband.*, pages 688–692, Sept 2009.

[37] S.J. Ingram, D. Harmer, and M. Quinlan. Ultrawideband indoor positioning systems and their use in emergencies. In *Position Location and Navigation Symposium*, pages 706–715, April 2004.

[38] Bing Jing, Yuankun Xue, Ye Fan, Ning Li, and Junyan Ren. Automatic gain control algorithm with high-speed and double closed-loop in uwb system. In *IEEE 10th International Conference on ASIC*, pages 1–4, Oct 2013.

[39] Matthias John and Max Ammann. Antenna optimization with a computationally efficient multiobjective evolutionary algorithm. *Articles*, page 24, 2009.

[40] Thomas Kailath, Ali H Sayed, and Babak Hassibi. *Linear estimation*, volume 1. Prentice Hall Upper Saddle River, NJ, 2000.

[41] E. Karapistoli, F-N Pavlidou, I. Gragopoulos, and I. Tsetsinas. An overview of the ieee 802.15.4a standard. *IEEE Communications Magazine*, 48(1):47–53, Jan. 2010.

[42] Chunhan Lee, Yushin Chang, Gunhong Park, Jaeheon Ryu, Seung-Gweon Jeong, Seokhyun Park, Jae Whe Park, Hee Chang Lee, Keum-Shik Hong, and

Man Hyung Lee. Indoor positioning system based on incident angles of infrared emitters. In *30th IEEE Annual Conference*, volume 3, pages 2218–2222, Nov 2004.

[43] Hui Liu, H. Darabi, P. Banerjee, and Jing Liu. Survey of wireless indoor positioning techniques and systems. *IEEE Transactions on Systems, Man, and Cybernetics, Part C: Applications and Reviews*, 37(6):1067–1080, Nov 2007.

[44] S. Marano, W.M. Gifford, H. Wymeersch, and M.Z. Win. Nlos identification and mitigation for localization based on uwb experimental data. *IEEE Journal on Selected Areas in Communications*, 28(7):1026–1035, Sept. 2010.

[45] R. Mautz and S. Tilch. Survey of optical indoor positioning systems. In *International Conference on Indoor Positioning and Indoor Navigation*, pages 1–7, Sept 2011.

[46] Andreas F Molisch, Kannan Balakrishnan, Chia-Chin Chong, Shahriar Emami, Andrew Fort, Johan Karedal, Juergen Kunisch, Hans Schantz, Ulrich Schuster, and Kai Siwiak. Ieee 802.15. 4a channel model-final report. *IEEE P802*, 15(04):0662, 2004.

[47] Andreas F Molisch, Philip Orlik, Zafer Sahinoglu, and Jin Zhang. Uwb-based sensor networks and the ieee 802.15. 4a standard-a tutorial. In *First IEEE International Conference on Communications and Networking*, pages 1–6, 2006.

[48] S. Olonbayar, G. Fischer, D. Kreiser, and R. Kraemer. Automatic gain controlling in ir-uwb communications designed for wireless sensors. In *IEEE International Conference on Ultra-Wideband (ICUWB)*, volume 1, pages 1–4, Sept 2010.

[49] Sylvain Pittet, Valerie Renaudin, Bertrand Merminod, and Michel Kasser. Uwb and mems based indoor navigation. *The Journal of Navigation*, 61:369–384, 7 2008.

[50] Yihong Qi, Hisashi Kobayashi, and H. Suda. Analysis of wireless geolocation in a

non-line-of-sight environment. *IEEE Transactions on Wireless Communications*, 5(3):672–681, Mar 2006.

[51] D. Roetenberg, H. Luinge, and P. Slycke. Xsens mvn: full 6dof human motion tracking using miniature inertial sensors. *Xsens Technologies B.V. White Paper*, Apr 2009.

[52] Zafer Sahinoglu, Sinan Gezici, and Ismail Guvenc. Ultra-wideband positioning systems: Theoretical limits, ranging algorithms, and protocols. 2008.

[53] J. Schroeder, S. Galler, K. Kyamakya, and K. Jobmann. Nlos detection algorithms for ultra-wideband localization. In *4th Workshop on Positioning, Navigation and Communication*, pages 159–166, Mar 2007.

[54] S. Sczyslo, J. Schroeder, S. Galler, and T. Kaiser. Hybrid localization using uwb and inertial sensors. In *IEEE International Conference on Ultra-Wideband*, volume 3, pages 89–92, Sept. 2008.

[55] M. Sharma, C.G. Parini, and A. Alomainy. Investigation of toa-based ranging accuracy of a miniature ultra-wideband antenna for human motion capture applications. In *11th International Conference on Wearable and Implantable Body Sensor Networks*, pages 11–15, June 2014.

[56] B. Silva, Zhibo Pang, J. Akerberg, J. Neander, and G. Hancke. Experimental study of uwb-based high precision localization for industrial applications. In *IEEE International Conference on Ultra-WideBand*, pages 280–285, Sept 2014.

[57] L. Stoica, A. Rabbachin, and I. Oppermann. A low-complexity noncoherent ir-uwb transceiver architecture with toa estimation. *IEEE Transactions on Microwave Theory and Techniques*, 54(4):1637–1646, June 2006.

[58] Lucian Stoica, Sakari Tiuraniemi, Heikki Repo, Alberto Rabbachin, and Ian Oppermann. Low complexity uwb circuit transceiver architecture for low cost sen-

sor tag systems. In *15th IEEE International Symposium on Personal, Indoor and Mobile Radio Communications*, volume 1, pages 196–200, 2004.

[59] Ya Tian, Hongxing Wei, and Jindong Tan. An adaptive-gain complementary filter for real-time human motion tracking with marg sensors in free-living environments. *IEEE Transactions on Neural Systems and Rehabilitation Engineering*, 21(2):254–264, Mar 2013.

[60] Y. Vanderperren, W. Dehaene, and G. Leus. A flexible low power subsampling uwb receiver based on line spectrum estimation methods. In *IEEE International Conference on Communications*, volume 10, pages 4694–4699, June 2006.

[61] Y. Vanderperren, G. Leus, and W. Dehaene. An approach for specifying the adc and agc requirements for uwb digital receivers. In *The Institution of Engineering and Technology Seminar on Ultra Wideband Systems, Technologies and Applications*, pages 196–200, April 2006.

[62] Roberto Verdone, Davide Dardari, Gianluca Mazzini, and Andrea Conti. *Wireless sensor and actuator networks: technologies, analysis and design*. Academic Press, 2010.

[63] M. Vossiek, L. Wiebking, P. Gulden, J. Wieghardt, C. Hoffmann, and P. Heide. Wireless local positioning. *IEEE Microwave Magazine*, 4(4):77–86, Dec 2003.

[64] Kai Wang, Yun-Hui Liu, and Luyang Li. A simple and parallel algorithm for real-time robot localization by fusing monocular vision and odometry/ahrs sensors. *Mechatronics, IEEE/ASME Transactions on*, 19(4):1447–1457, Aug 2014.

[65] Andy Ward, A. Jones, and A. Hopper. A new location technique for the active office. *IEEE Personal Communications*, 4(5):42–47, Oct 1997.

[66] M.Z. Win and R.A. Scholtz. Characterization of ultra-wide bandwidth wireless indoor channels: a communication-theoretic view. *IEEE Journal on Selected Areas in Communications*, 20(9):1613–1627, Dec 2002.

[67] Veikko Hovinen (Wisair). A proposal for a selection of indoor uwb path loss model. *IEEE 802.15-02-280*, June 2002.

[68] Oliver J Woodman. An introduction to inertial navigation. Aug 2007.

[69] J. Youssef, B. Denis, C. Godin, and S. Lesecq. Loosely-coupled ir-uwb handset and ankle-mounted inertial unit for indoor navigation. In *IEEE International Conference on Ultra-Wideband (ICUWB)*, pages 160–164, Sept 2011.

[70] Kegen Yu and E. Dutkiewicz. Nlos identification and mitigation for mobile tracking. *IEEE Transactions on Aerospace and Electronic Systems*, 49(3):1438–1452, July 2013.

[71] J. Zhang, R.A. Kennedy, and T.D. Abhayapala. Cramer-rao lower bounds for the time delay estimation of uwb signals. In *IEEE International Conference on Communications*, volume 6, pages 3424–3428 Vol.6, June 2004.

[72] YP Zhang, Li Bin, and Cao Qi. Characterization of on-human-body uwb radio propagation channel. *Microwave and Optical Technology Letters*, 49(6):1365–1371, 2007.

[73] L. Zwirello, C. Ascher, G.F. Trommer, and T. Zwick. Study on uwb/ins integration techniques. In *8th Workshop on Positioning Navigation and Communication*, pages 13–17, April 2011.

[74] L. Zwirello, Xuyang Li, T. Zwick, C. Ascher, S. Werling, and G.F. Trommer. Sensor data fusion in uwb-supported inertial navigation systems for indoor navigation. In *IEEE International Conference on Robotics and Automation*, pages 3154–3159, May 2013.